

Angelika Kühnle

**Molecular self-assembly
and chiral recognition:
Biologically relevant molecules
on metal surfaces**

PhD Thesis October 2002
Center for Atomic-scale Materials Physics,
Interdisciplinary Nanoscience Center and
Department of Physics and Astronomy,
University of Aarhus, Denmark





This thesis is submitted to the Faculty of Science at the University of Aarhus, Denmark, in order to fulfill the requirements for obtaining the PhD degree in physics. This work has been performed under the supervision of F. BESENBACHER in the Scanning Tunnelling Microscopy group at the Department of Physics and Astronomy from October 1999 to October 2002, including an abroad research project in the group of N. V. RICHARDSON at the University of St. Andrews in September 2001.

Angelika Kühnle
October 2002

The image gallery at the top of this page shows how the surface structures of cysteine on Au(110)-(1 × 2) varies at different surface temperatures and coverages. To the left, cysteine nanoclusters obtained at low temperatures are displayed, followed by the as-deposited structure at room temperature (third image). At slightly elevated temperatures, chiral molecular dimers coexist with molecular double rows (images 4 to 6). At high cysteine coverages, dense chiral layers are formed. Upon annealing at high temperatures, the molecules decompose, leaving behind a $c(4 \times 2)$ sulphur structure, as evident from the image on the right.

Contents

1	Introduction	1
2	Methods	11
2.1	Scanning tunnelling microscopy	11
2.1.1	STM Theory	11
2.1.2	The Aarhus STM	14
2.2	Reflection absorption infrared spectroscopy	15
2.3	Low-energy electron diffraction	16
2.4	X-ray photoelectron spectroscopy	17
2.5	Temperature-programmed desorption	17
2.6	Calculations	18
2.6.1	Density-functional theory	18
2.6.2	Effective-medium theory	19
3	Literature survey	21
3.1	Chirality	21
3.2	Self-assembly	24
3.3	Molecular adsorption studies	24
3.3.1	Molecular self-assembly	24
3.3.2	Sulphur-containing molecules	26
3.3.3	Adsorption of amino acids	29
3.3.4	Inducing surface chirality by molecular adsorption	30
4	Cysteine on Au(110)	33
4.1	Introduction	33
4.1.1	Au(110)	33
4.1.2	Cysteine	34
4.1.3	Overview of the cysteine adsorption on Au(110)	35
4.2	Room-temperature structures	38
4.2.1	STM results	38
4.2.2	RAIRS experiments	38
4.3	Molecular chiral recognition	42
4.3.1	STM results	42
4.3.2	DFT calculations	46
4.3.3	Cysteine pairs at kink sites	52
4.4	Self-assembly of molecular chains	56
4.4.1	STM results	56
4.4.2	DFT calculations	58
4.5	Cysteine adsorption at higher coverages	65

4.5.1	Extended surface restructuring	65
4.5.2	EMT calculations	65
4.5.3	Dense cysteine domains	69
4.5.4	Full monolayer coverage	71
4.6	Chiral symmetry breaking	75
4.6.1	STM results	75
4.6.2	Possible origin of the symmetry breaking	76
4.7	Self-assembly of chiral nanoclusters	81
4.7.1	STM results and discussion	81
4.7.2	Cluster manipulation and diffusion	85
4.7.3	Possible nanocluster structure	86
4.8	Summary and conclusions	89
5	Sulphur on Au(110)	91
5.1	H ₂ S on Au(110)	91
5.2	Conclusion	95
6	Cysteine on Au(111)	97
6.1	Au(111)	97
6.2	Previous studies	97
6.3	Submonolayer coverage	99
6.4	Increasing coverage	101
6.5	Discussion	104
7	Dodecanethiol on Cu(110)	107
7.1	Introduction	107
7.2	TPD results	109
7.3	STM results	111
7.3.1	Low-temperature deposition	111
7.3.2	Room-temperature deposition	111
7.4	XPS results	115
7.5	LEED results	118
7.6	Discussion	120
7.7	Conclusion	125
8	German summary	127
9	Publications	131
9.1	List of publications related to this thesis	131
9.2	Other studies	132

10 List of abbreviations

133

11 Acknowledgements

135

1 Introduction

Nature provides a rich variety of structures and macromolecular “machines” with highly specialised designs, whose binding and functioning capabilities have emerged from millions of years of evolutionary optimisation [1–3]. These specialised nanomachines are basically constructed from a very limited number of building blocks, including the set of 20 natural amino acids and the four nucleotide bases. Learning from nature by understanding the optimisation of structural properties enables us to employ this knowledge for the design of new structures that can be used in other contexts ranging from technical applications [4, 5] to bioartificial organs [6]. The impact of this promising approach is reflected in the growing research area referred to as biomimetics [6–8].

Proteins, in particular, adopt a wide range of specialised functions [9], which explains the high expectations for current efforts to relate protein structure and function (proteomics) [10]. Elastin, for instance, a rubber-like protein that is found where high elasticity is needed, has achieved a high degree of perfection. It extends under pressure and releases up to 90% of the energy stored upon relaxation. Other examples include resilin, a protein found in insect wings, and various proteins from the insect cuticle demonstrating high waterproof and wet strength [11, 12]. One of the most advanced protein studies is research on spider silk [13, 14]. This protein-based biopolymer exhibits interesting properties as it is as strong as high-tensile steel but at the same time as elastic as rubber. Due to this technically important combination, spider silk has attracted much attention for the potential use in biomimetic medical devices such as ligaments and sutures and for the fabrication of lightweight and soft body armor [9].

Another widely studied research area in the field of biomimetics is the class of so-called hybrid materials. Much of the importance of these biological compounds is based on the clever combination of minerals and organic materials at the nanometre scale. Biominerals are, for example, found in shells, teeth and bones [15, 16]. Compared to pure aragonite (calcium carbonate), just 3%

by weight of organic polymers built into highly oriented aragonite improve the strength of molluscan shells and pearls by a factor of 3000 [17, 18].

Apart from specialised properties, also remarkable chemical control is demonstrated in biology, for example in the recognition of an antigen by its antibody. Understanding molecular recognition is a key issue in developing biosensors [19–23].

Researchers in the field of nanotechnology [24] have just started to employ nature’s strategies for the assembly of functionalised structures in the nanometre-size range. Visions of nanotechnology include producing new materials with highly specialised properties and functioning, but also the development of new manufacturing processes that minimise the generation of unwanted by-products. One of the key driving forces for nanotechnology has always been the continuous miniaturisation of electronic circuits [25, 26]. Conventionally, photolithography is employed for the parallel writing of these structures. This technique is, however, limited in resolution by the wavelength of the light used, and with current ultraviolet light-based techniques, the lower limit is about 130 nm. This limit can be pushed further by serial writing with a well-focussed beam of electrons or atoms [27], but with current technologies this method is slow and costly. The limitation of these classical “top-down” strategies to a minimal size of some nanometres points to the need for new concepts in the electronic device production [28–31].

One possibility is the direct construction of functional nanostructures from elementary atomic or molecular building blocks, the so-called “bottom-up” approach, which has proven possible with advanced methods of atomic and molecular manipulation by tunnelling [32] and force microscopy [33], methods that are, however, unlikely to develop into tools for an economic production of functionalised nanomaterials. The strength of the “bottom-up” approach can much better be developed in combination with another important concept, namely molecular self-assembly [34–39]. This concept is as simple as it is efficient: Put your effort in choosing the right system, provide proper starting conditions and then let nature do the rest. More precisely, molecular self-assembly describes the reversible association of molecules into well-defined aggregates that involve non-covalent interactions such as electrostatic interactions, VAN-DER-WAALS forces and hydrogen bonds [34].

Examples of molecular self-assembly are abundant in nature, many of which are astonishingly sophisticated, such as the complex folding of peptide strands into highly specialised functioning proteins [40, 41] or the transfer of genetic information from DNA to RNA.¹ Currently, scientists are trying to mimic such self-assembly processes and transfer them into other contexts [1, 9]. Surface

¹DNA stands for *desoxyribonucleic acid* and RNA for *ribonucleic acid*.

functionalisation by self-assembled monolayers is exploited [42], for instance, to improve biocompatibility in implants [43] or molecular recognition in biosensors [23], and quite promising results have been achieved in the fabrication of such biosensors that detect specific molecules [44, 45]. To design functional nanostructures that can be fabricated by molecular self-assembly at surfaces, the understanding of molecule-substrate and molecule-molecule interactions is a key prerequisite.

The work to be presented in this thesis is motivated by the research efforts mentioned here and contributes to the understanding of molecular self-assembly and recognition at a very fundamental level. By studying the structures formed by organic molecules on metal surfaces, one obtains information on molecular interactions that are of relevance for the usually far more complex processes outlined above. The adsorption studies performed in this work can therefore be understood as a very simple and basic model system that illustrates important aspects of molecular interaction at the molecular level.

In this thesis, I study the adsorption of two sulphur-containing molecules on three different metal surfaces with a *scanning tunnelling microscope* (STM) in an ultrahigh-vacuum environment, gaining insight into the temperature-dependent interplay between molecule-substrate and molecule-molecule interactions. One of the molecules investigated belongs to the class of alkanethiols, molecules consisting of a hydrocarbon chain with a mercapto headgroup ($-\text{SH}$). These molecules form so-called *self-assembled monolayers* (SAMs) on gold surfaces [46, 47], which have been studied extensively because of their promising properties for technical applications such as lubrication, corrosion protection or biocompatible surface-functionalisation [48, 49], but also as a model system for studying molecular self-assembly. By far the most data have been collected on the close-packed (111) surface of gold. In this thesis, the adsorption of dodecanethiol ($\text{HS}-(\text{CH}_2)_{11}-\text{CH}_3$) is studied on another surface that exhibits an even stronger binding affinity towards sulphur, namely the (110) facet of copper, allowing the consequences of changing the molecule-surface interaction compared to gold to be studied. The other molecule investigated in this work is the naturally occurring amino acid cysteine ($\text{HS}-\text{CH}_2-\text{CH}(\text{NH}_2)-\text{COOH}$). As amino acids are the basic building blocks of proteins, they constitute simple model systems for studying how peptides and proteins interact with surfaces [8]. Cysteine has been chosen since it is the only thiol among the naturally occurring amino acids, making the comparison between cysteine and alkanethiol structures interesting. Compared to dodecanethiol, cysteine is rather small, and VAN-DER-WAALS interactions are consequently less important in the overlayer formation. On the other hand, cysteine consists of three functional groups that

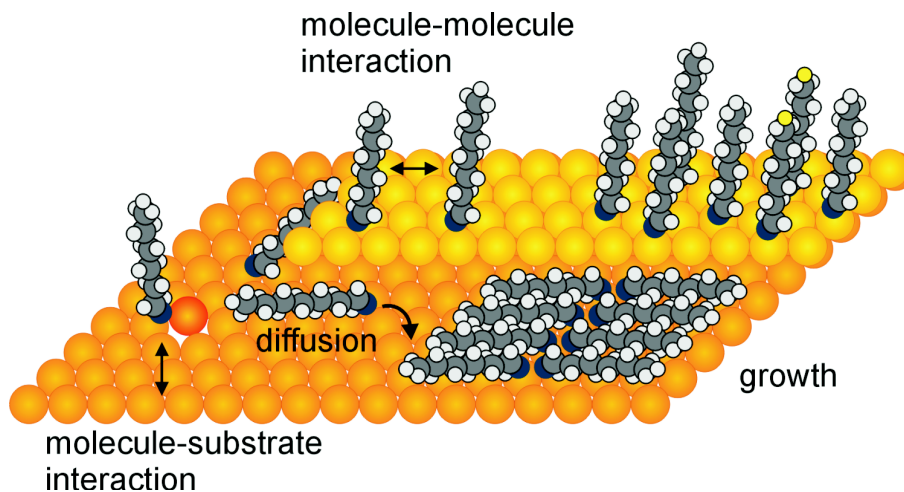


Figure 1: Processes influencing the molecular-structure formation on a substrate surface.

influence the overlayer formation and allow a rich variety of surface structures to be observed. Cysteine adsorption is studied on two rather different gold surfaces to investigate the influence of the surface geometry and reactivity on the structure formation. The main part of this thesis concerns the cysteine adsorption onto the reactive (110) facet of gold, which is reconstructed in its clean state and exhibits a large surface corrugation and low-coordinated surface atoms [50,51]. The results on the Au(110) surface have been supplemented with adsorption experiments on another surface, namely the Au(111) surface, which is close-packed and inert,² thereby increasing the relative influence of molecule-molecule interactions on the molecular-structure formation.

Besides being an amino acid and a thiol, cysteine is notable for being a chiral molecule (see Fig. 2). This adds important aspects to the observed cysteine structures that can be related to fundamental mechanisms underlying molecular biology.

Chirality is a geometrical property of an object, being non-superimposable with its mirror image like a left and a right hand (Fig. 3). The different spatial configurations of a chiral molecule, which cannot be superimposed by any rotation

²Compared to (111) facets of most other metals, Au(111) actually possesses some modulation since it is reconstructed into the so-called herringbone reconstruction [52].

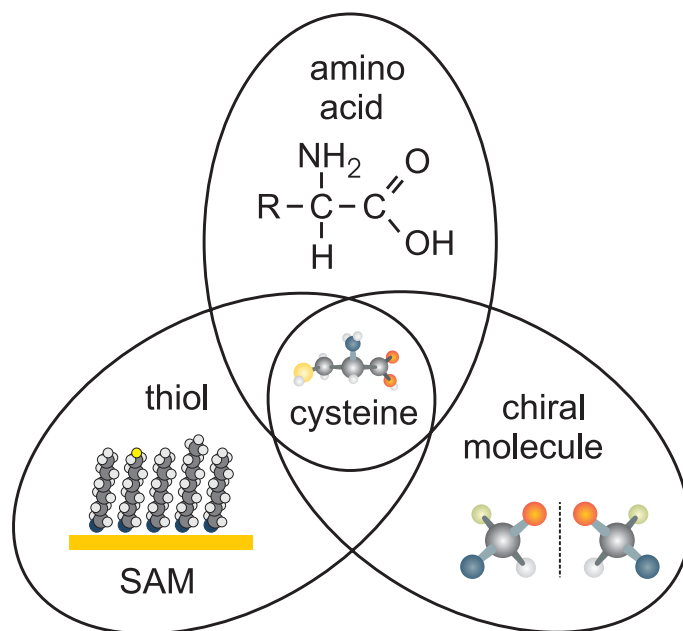


Figure 2: Cysteine as a biomolecule, a thiol and a chiral molecule.

Cysteine belongs to both the important classes of natural amino acids and thiols. Moreover, it is a chiral molecule.

or translation, are referred to as *enantiomers*.

Molecular chirality, the “handedness” of molecules, is abundant in everyday life, since fundamental processes within chemistry and molecular biology are governed by chiral molecules. Biological macromolecules are very often constructed by chiral building blocks, and their functioning crucially depends on their chirality. Proteins are exclusively built from L amino acids, while the backbone of DNA consists only of D sugar molecules. The origin of this homochirality is still a puzzle, but breaking the homochirality by incorporating molecules of the other enantiomer would destroy the macromolecule’s functioning.

Enzymatic reactions and other ligand-receptor interactions are governed by the spatial morphology, and thus by the chirality of the interacting molecules, as these reactions are based on a lock-and-key principle [53]. Therefore, different

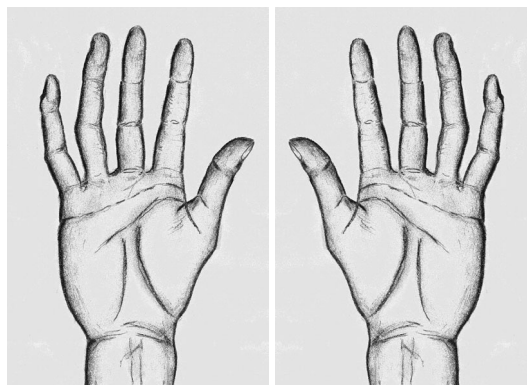


Figure 3: Hands are chiral objects.

The left and the right hand are mirror images and cannot be superimposed by any rotation or translation. The term “chiral” stems from the Greek word “cheir” meaning “hand”.

enantiomers of a chiral molecule may have distinctly different biological activity. The smell of caraway and spearmint, for example, originates from the same molecule, carvone, but in its two enantiomeric forms, which the nasal receptors can tell apart. Likewise, the activity of drugs may strongly depend on their spatial conformation. Since a drug molecule must match a specific receptor site, often only one enantiomer is of interest. The other enantiomers are often useless, but may be harmful as in the case of Thalidomide given to pregnant women, where one enantiomer reduced morning sickness, but the other harmed the fetus [54].

A central result from the present cysteine adsorption studies is the molecular-level identification of a simple chiral recognition process, occurring between individual cysteine molecules. Cysteine forms molecular dimers on a Au(110) surface, whose rotation with respect to the close-packed gold rows reflects the chirality of the cysteine molecules. When both enantiomeric forms are present at the surface at the same time, exclusively homochiral dimers are found on the surface, demonstrating chiral specificity during the cysteine dimerisation. In close cooperation with theory – performed by B. HAMMER and L. MOLINA from the University of Aarhus – the mechanism for this chiral recognition process is identified, disclosing the critical role of the particular adsorption geometry of the cysteine dimers on the gold surface. The reason for the chi-

ral discrimination is found in the simultaneous optimisation of three bonds on each cysteine molecule that require both cysteine molecules within a dimer to be of the same conformation. Hence, the observed cysteine dimers constitute a molecular-level model system for studying the mechanism that underlies chiral recognition, which was already formulated in 1933 in the well-known three-point contact model for chiral recognition [55,56].

Cysteine adsorption on Au(110) has been studied in a wide temperature range both with scanning tunnelling microscopy and reflection absorption infrared spectroscopy. Depending on temperature and surface coverage, a variety of different molecular overlayers have been observed whose formation is found to be governed by the surface geometry. The already mentioned molecular dimers are found to align on the surface in an ordered array that involves an extended restructuring of the surface, demonstrating the ability of these sulphur-containing molecules to modify the local surface geometry in order to optimise the molecule-surface interaction. Coexisting with the molecular dimers, extended double rows form on the surface, whose uni-directional growth is directed by the interaction with the gold surface. A lifting of the missing-row reconstruction underneath the rows has been identified as the driving force for the chain growth, demonstrating the strong influence of molecule-substrate interactions on the structure formation.

When cysteine is deposited at low temperatures, a self-assembly process into identical nanoclusters of uniform size was observed. In contrast to chemisorbed structures observed at room temperature, these clusters are physisorbed and all functional groups seem to be saturated internally, forming a hydrogen-bonded network. Compared to formerly observed metallic clusters [57] that rely on magic shell closing, these molecular clusters seem to represent a more complex formation mechanism that may be of interest when size uniformity is desired. To complement the STM data on the Au(110) surface by spectroscopic measurements in order to gain information on the binding configuration of the cysteine molecules, infrared spectroscopy data have been obtained in collaboration with Q. CHEN and N. V. RICHARDSON from the University of St. Andrews, UK.

In contrast to the observations on the Au(110) surface, the molecular structures that have been revealed on the comparably unreactive Au(111) surface are found to be much less influenced by the surface geometry. In particular, an ordered structure has been observed that interacts only weakly with the substrate surface as it is found not to affect the herringbone reconstruction. For high cysteine coverages, variations of a hexagonal structure are found, most likely reflecting the many different possibilities of the molecules to interact with each other on an unstructured substrate surface. Not until annealing, a superstructure is formed that is very similar to that of alkanethiols on Au(111), indicating

that thermal energy is needed to introduce the transition from a physisorbed to a chemisorbed species. Compared to alkanethiol films, however, the annealed cysteine structure is less well developed, a fact that can be explained by the absence of the stabilising intermolecular VAN-DER-WAALS forces of the hydrocarbon chains found in the alkanethiol SAMs.

The dodecanethiol adsorption has been studied in cooperation with S. VOLLMER and G. WITTE from the University of Bochum, Germany, who have performed temperature-programmed desorption, X-ray photoelectron spectroscopy and low-energy electron diffraction experiments, complementing the STM data. This multi-technique study reveals structural changes accompanying the transition from lying-down physisorbed molecules at low temperatures to standing-up, chemisorbed species at room temperature that have lost their hydrogen atoms at the mercapto group and now form a strong sulphur-copper bond. This standing-up phase exhibits a moiré pattern reflecting the compromise between the covalent sulphur-copper bonds and the weaker VAN-DER-WAALS interactions among the alkane chains.

In the following chapter, the experimental and theoretical methods used in this thesis are described. Besides scanning tunnelling microscopy, both low-energy electron diffraction and the different spectroscopic methods utilised in this work are described briefly as well as the two theoretical approaches: Density-functional and embedded-medium theory. Chapter 3 gives a literature survey on adsorption and self-assembly of molecules with emphasis on sulphur-containing molecules and amino acids. The chapter is completed by a review on chiral phenomena at surfaces. The experiments regarding cysteine adsorption on Au(110) are presented in chapter 4. After a brief description of cysteine and the geometry of the reconstructed Au(110) surface, the room-temperature adsorption experiments are discussed, followed by the chiral structures observed at slightly elevated temperatures, namely the cysteine dimers and molecular double-row structure. In section 4.5, the structures formed after increasing the cysteine coverage are described, and the results after further annealing are presented. An interesting phenomenon demonstrating the breaking of chiral symmetry has been observed in this work and is discussed in section 4.6, although a comprehensive explanation of this effect is still missing. The chapter on cysteine adsorption on Au(110) is completed by the presentation of the low-temperature experiments, which demonstrate self-assembly of cysteine nanoclusters. Hydrogen sulphide adsorption experiments that have been carried out to supplement the adsorption studies of the two sulphur-containing molecules investigated in this thesis are presented in chapter 5. In chapter 6, the experiments on cysteine adsorption on Au(111) are discussed. After a

brief introduction to other cysteine adsorption experiments performed on this surface, the adsorption results obtained in this work are presented. The experiments on dodecanethiol adsorption on Cu(110) are described in chapter 7, including thermal desorption and X-ray photoelectron spectroscopy data as well as low-energy electron diffraction results.

2 Methods

In this chapter, the basic principles behind the main experimental techniques and theoretical approaches utilised for this work are outlined. The aim is to provide an introductory overview as well as references for further reading.

2.1 Scanning tunnelling microscopy

Since its development in the early 1980ies by G. BINNIG and H. ROHRER, *scanning tunnelling microscopy* (STM) has become an important standard technique in surface science [32]. In contrast to averaging methods such as low-energy electron diffraction, STM is a local probe which gives real-space insight into physical phenomena occurring at surfaces. The basic principle is as follows: A metallic tip, the probe, is brought into close proximity of a conducting surface. At a distance of a few Ångströms ($1\text{Å} = 10^{-10}\text{ m}$), the wavefunctions of the topmost tip atom and the surface atoms overlap sufficiently to allow for quantum mechanical tunnelling of electrons between tip and sample when a bias voltage is applied.

2.1.1 STM Theory

A very simple, one-dimensional quantum mechanical model (Fig. 4) compares the STM tunnelling situation with a constant potential barrier with a height U and a width d [58]. The wavefunction ψ of an electron with mass m and energy E at a distance z in the barrier is given as:

$$\psi(z) = \psi(0) e^{-\kappa z} \text{ where } \kappa = \frac{1}{\hbar} \sqrt{2m(U - E)}. \quad (1)$$

In this model, the work functions ϕ of the tip and the metal surface are assumed to be the same. The variable κ is the inverse decay length. Then, for electrons at the FERMI energy ϵ_F , the barrier height equals the work function. Depending

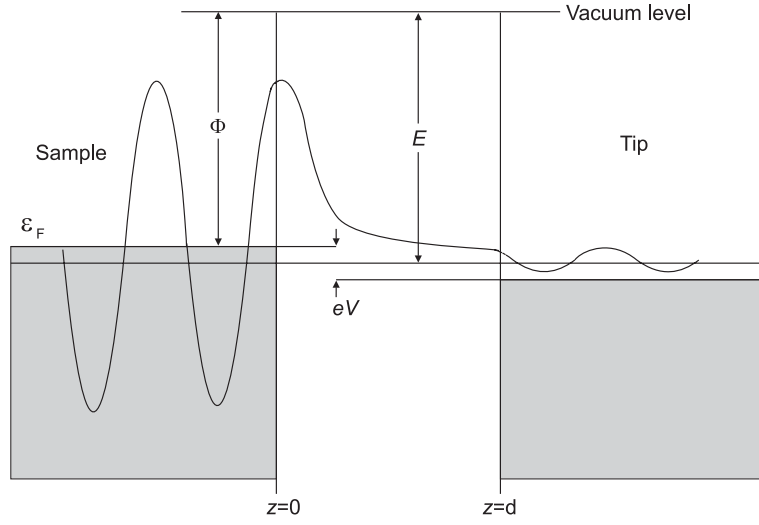


Figure 4: One-dimensional tunnelling junction.

To the left, the sample is depicted with a one-dimensional wavefunction penetrating into the barrier region between the sample and the tip to the right, leading to a non-zero probability for an electron to tunnel from the sample into the tip.

on the polarity of the bias voltage, V , the electrons tunnel from the filled tip states into empty sample states or *vice versa*. The tunnelling current is proportional to the sum over the squares of sample states ψ_n with energy ϵ_n within the energy interval eV , defined by the bias voltage [58]. For small eV , the tunnelling current reads:

$$I \propto \sum_{\epsilon_n = \epsilon_F - eV}^{\epsilon_F} |\psi_n(0)|^2 e^{-\frac{2}{\hbar} \sqrt{2m\phi} z} \quad (2)$$

$$\implies I \propto e^{-\frac{2}{\hbar} \sqrt{2m\phi} z} = e^{-1.025 \sqrt{\phi[\text{eV}]} z[\text{\AA}]} \quad (3)$$

From equation 3 it can be seen that the tunnelling current is exponentially dependent on the distance between tip and surface, since the wavefunctions decay exponentially into the vacuum gap. A very useful understanding can be deduced directly from this equation, namely, if a typical value of $\phi = 4 \text{ eV}$ is

assumed for the work function,³ the tunnelling current changes about an order of magnitude by varying the gap distance by just $z \approx 1 \text{ \AA}$.

The qualitative consideration above makes the extreme sensitivity of STM probable. To gain quantitative knowledge of the situation, however, the three-dimensional wavefunctions must be calculated explicitly by solving the SCHRÖDINGER equation of the combined tip/sample system. Considering the number of atoms involved, this is very complex for a realistic situation, and, therefore, approximations must be employed. A detailed discussion of these approaches is not feasible within the scope of this introduction; nevertheless, two concepts should be mentioned briefly: J. BARDEEN treated the tip and the sample as non-interacting systems and calculated the tunnelling current from the separate wavefunctions of the tip, ψ_t , and the sample, ψ_s [59]. Within this approach, the tunnelling matrix element M is given by:

$$M = \frac{\hbar^2}{2m} \int_{S_0} (\psi_t^* \nabla \psi_s - \psi_s \nabla \psi_t^*) dS, \quad (4)$$

where S_0 is any surface placed entirely in the vacuum gap region. Using time-dependent perturbation theory, the tunnelling current can be calculated as an integral over all electrons tunnelling elastically between the sample and the tip.

$$I = \frac{2\pi e}{\hbar} \int_{-\infty}^{+\infty} [f(\epsilon - eV) - f(\epsilon)] \cdot \rho_s(\epsilon - eV) \cdot \rho_t(\epsilon) |M|^2 d\epsilon, \quad (5)$$

with ρ being the electron density of states of the sample and the tip, respectively. The FERMI-DIRAC function $f(\epsilon)$ can be approximated as a step function for $k_B T \ll \epsilon - \epsilon_F$, leading to the following simplification:

$$I = \frac{2\pi e}{\hbar} \int_{\epsilon_F}^{\epsilon_F + eV} \rho_s(\epsilon - eV) \cdot \rho_t(\epsilon) |M|^2 d\epsilon. \quad (6)$$

Based on this transfer Hamiltonian description, J. TERSOFF and D. HAMANN modelled the tip function as an s -wave [60] and showed that STM images reflect the topography of the *local density of states* (LDOS) at the FERMI energy at the centre of the curvature of the tip. The LDOS $\rho(z, E)$ is defined as the number of electrons per unit volume and per unit energy at a position z and energy ϵ , as shown in equation 7 for small energies E .

$$\rho(z, \epsilon) = \frac{1}{E} \sum_{\epsilon_n = \epsilon - E}^{\epsilon} |\psi_n(z)|^2. \quad (7)$$

³The work function ϕ is 4.6 eV for Cu and 5.4 eV for Au [58].

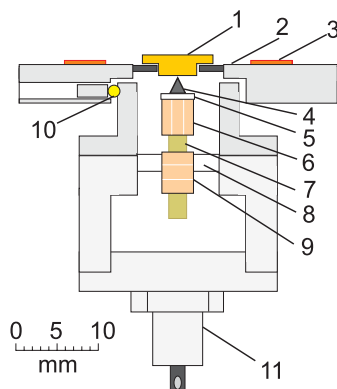


Figure 5: Setup of the Aarhus STM.

Legend: 1) sample, 2) tantalum holder, 3) springs, 4) tip, 5) macor holder, 6) scanner tube, 7) rod, 8) macor ring, 9) inch worm, 10) quartz ball and 11) zener diode. Design and construction by E. LÆGSGAARD.

The real situation is often more complicated than s -wave tip model suggests, since other orbitals can contribute to the tip wavefunction. Moreover, the tip frequently changes, for example when molecules are attached to the tip apex [61, 62].

2.1.2 The Aarhus STM

To acquire an STM image, the tip is scanned over the substrate surface. In the commonly used *constant-current mode*, the tip/sample distance is adjusted to maintain the tunnelling current constant. In the Aarhus STM, two piezoelectric tubes are utilised to perform the tip movement. One piezo tube, the so-called *inch-worm*, performs the coarse approach of a shaft carrying the second piezo crystal on which the tip is mounted. The coarse approach is realised by an “inch-wormish” procedure: The lower part of the three-divided hollow piezo crystal clamps the shaft while the middle part contracts. Then the upper part fixes the shaft, the lower part is unclamped, and the middle part expands. In this way, the shaft with the tip is moved upwards to the sample until a tunnelling current is detected. The second piezo tube, the scanner tube, performs the lateral and vertical movement of the tip during scanning. It is a hollow piezo tube with one inner and four outer electrodes. When biasing

two opposite outer electrodes with antisymmetric voltages, the piezo is bent, leading to a lateral deflection of the tip. Correct wiring of the four electrodes is important, since, for instance, the exchange of the +X and -X wires would result in a mirrored image. As the studies in this thesis are on chiral molecule adsorption, the connections of the STM have been checked to confirm that the acquired images represent the real situation at the surface. Upon biasing the inner electrode with respect to the outer ones, the scanner tube expands and contracts, resulting in the vertical tip movement. As a voltage of the order of 1 V leads to a deflection of only 10 Å, the movement of the piezoelectric tubes can be controlled very precisely, allowing for sub-atomic step sizes. The compact design of the Aarhus STM unit makes it very vibration resistant by suppressing all low-frequency components, while high frequencies are damped out by suspending the STM from four soft springs.

The STM images shown in this thesis have been acquired in three different *ultrahigh-vacuum* (UHV) systems with a base pressure of about 10^{-10} mbar. The chambers are equipped with standard UHV facilities and sample manipulators allowing for cooling to 120 K and heating the sample. The STM in the chamber used for the cysteine experiments presented in chapters 4 and 6 reaches a minimum temperature of 110 K upon cooling with liquid nitrogen (LN₂). During the short transfer time (less than 1 min) from the manipulator into the STM, cooling of the sample is not possible, which leads to an estimated temperature rise of about 20 K for the lowest temperatures.

2.2 Reflection absorption infrared spectroscopy

Infrared spectroscopy facilitates the detection of changes in a molecule's spatial configuration such as bending or stretching vibrations, which are associated with frequencies from 10^{12} to 10^{14} Hz. Conventional infrared spectroscopy is performed by passing a beam of infrared radiation through a sample and recording which frequencies are absorbed. This is obviously not applicable for surface studies since a metal sample is not transparent, but reflects an infrared beam. In this case, RAIRS is utilised, where the beam is aligned so as to strike the surface at grazing incidence and pass through the adsorbed molecules twice – once on the way in and once on the way out. This is sufficient to monitor an absorption spectrum although the demand on sensitivity is very high compared to transmission absorption spectroscopy.

Vibrating dipoles introduce image dipoles of opposite sign in the metal surface, resulting in the so-called *metal-surface selection rule*: The dipole moments of vibrations parallel to the surface cancel with the induced image dipole moment. On the other hand, dipoles vibrating perpendicular to the surface plane are

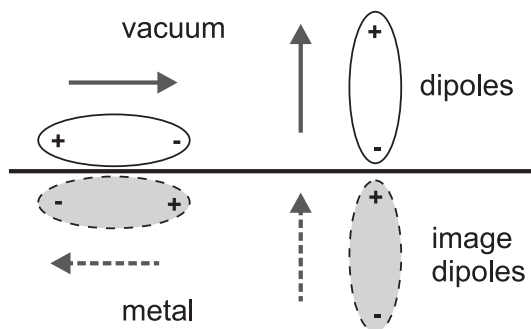


Figure 6: RAIRS metal surface selection rule.

A vibration dipole oriented parallel to the surface induces an image dipole of opposite sign and equal magnitude in the metal, cancelling the overall dipole moment. A perpendicular dipole moment is enhanced by this effect.

enhanced for the same reason by a factor of two, as illustrated in Fig. 6.

2.3 Low-energy electron diffraction

Low-energy electron diffraction (LEED) is an important technique for the investigation of periodic surface structures. With this area-averaging method, lattice parameters can be obtained very accurately and the pattern of ordered overlayers is obtained qualitatively; the overlayer pattern is disclosed, but the absolute position of adatoms or molecules on the substrate cannot be determined. LEED is used extensively in surface science as a routine to examine the surface quality or to determine superstructures.

The basic principle behind LEED is the BRAGG diffraction of low-energy electrons with an associated DE BROGLIE wavelength λ from the substrate surface lattice. The kinetic energy of the electrons is varied in the range of 10 – 300 eV. In this energy region, the mean free path of the electrons in solids is limited to the surface region according to the “universal curve” [63], making LEED a surface sensitive technique. To a first approximation, the so-called kinematic approximation, the situation can therefore be simplified to the case where only the topmost atomic layer with a lattice distance d is involved in the scattering process and multi-scattering events are neglected. The beam of electrons hits the surface at an angle of incidence θ_i and of reflection θ_f , which results in

diffraction spots only when the BRAGG condition is fulfilled:

$$2d(\sin\theta_f - \sin\theta_i) = n\lambda. \quad (8)$$

The diffracted electrons are monitored on a fluorescent screen and represent the reciprocal lattice, whose lattice parameters are inversely proportional to those of the direct lattice.

2.4 X-ray photoelectron spectroscopy

The governing principle behind *X-ray photoelectron spectroscopy* (XPS) is the photoelectric effect. A sample is irradiated with X-rays of a given energy $\hbar\omega$ in the range of 1200 – 1400 eV, leading to the emission of core-level electrons. The kinetic energy of the photoelectrons E_{kin} is both element-specific and a reflection of the chemical state of the emitting atom as it includes the binding energy E_b of the electron. It also includes the difference ϕ between sample and detector work functions:

$$E_{\text{kin}} = \hbar\omega - E_b - \phi. \quad (9)$$

As in the case of LEED, the mean free path of the photoelectrons is very short in solids, making this technique surface sensitive as well. When the chemical state of a surface atom or adsorbate is changed, the characteristic position of the XPS peak is shifted accordingly, allowing for a surface-sensitive determination of changes in bonding and environment.

2.5 Temperature-programmed desorption

Temperature-programmed desorption (TPD) allows for the investigation of desorption mechanisms and the determination of desorption energies of adsorbates by programmed heating of the substrate with a fixed rate β while the desorbing species are monitored by a mass spectrometer. The shape of the monitored desorption curves is related to the order of the desorption process,⁴ while the temperature T associated with the desorption peak gives a measure of the desorption energy E_{des} . In the case of first order desorption, the REDHEAD formula [64] reads:

$$\frac{E_{\text{des}}}{k_B T} \approx \ln\left(\frac{\nu T}{\beta}\right) - 3.64, \quad (10)$$

where k_B is the BOLTZMANN constant and ν the pre-exponential factor associated with the surface potential felt by the adsorbate.

⁴The order of the desorption, x , is defined by the dependence of the rate of desorption on the coverage, Θ : $\frac{\partial\Theta}{\partial t} \propto \Theta^x$.

2.6 Calculations

The *density-functional theory* (DFT) calculations presented in this thesis were performed by B. HAMMER and L. MOLINA from the Department of Physics and Astronomy of the University of Aarhus. As the calculations crucially contribute to the understanding of the experimental results obtained in this work, a brief overview of this theoretical approach will be given along with a description of the more approximative *effective-medium theory* (EMT) that has been used to obtain estimates for the formation energies of several surface reconstructions revealed by STM.

2.6.1 Density-functional theory

In principle, every system can be completely described within the formalism of wavefunctions derived in 1926 by E. SCHRÖDINGER. The calculation of the electronic structure and the total energy of a given system using wavefunction-based methods [65] becomes, however, challenging when the number of particles considered exceeds a critical value, and in most cases an exact description is impossible for larger many-body problems involving more than 10 particles.

DFT offers an alternative approach by focussing on the electron density $n(r)$ of the system rather than the wavefunctions [66], giving a complementary, real-space perspective of the situation. Compared to the problem of solving the many-body SCHRÖDINGER equation, the computational cost for DFT calculations rises much more moderately with the number of atoms, allowing for an *ab initio* description of many-particle problems that cannot be handled by wavefunction-based methods.

The basis for this electron-density formalism was laid in 1964 by P. HOHENBERG and W. KOHN, who demonstrated that “the ground state density of a bound system of interacting electrons in some external potential $V(r)$ determines this potential uniquely” [67]. Therefore, the electron density implicitly determines both the Hamilton operator \hat{H} and the ground state wavefunctions $\Psi\{r_i\}$, where r_i is the set of coordinates of all participating particles:

$$n(r) \Rightarrow V(r) \Rightarrow \hat{H} \Rightarrow \Psi\{r_i\}. \quad (11)$$

Finally, as the total energy E of the system is uniquely defined by \hat{H} and Ψ , the total energy can be regarded as a functional of the electron density:

$$E = \langle \Psi | \hat{H} | \Psi \rangle \Rightarrow E = E[n(r)]. \quad (12)$$

Using the RAYLEIGH-RITZ variation principle, the total energy can be calculated by minimising the total energy obtained from a given trial ground state

electron density $\tilde{n}(r)$:

$$E = \min_{\tilde{n}(r)} E_V[\tilde{n}(r)]. \quad (13)$$

This approach reduces the many-body problem from the wavefunction-based formalism to the solution of a set of one-electron SCHRÖDINGER equations, the so-called KOHN-SHAM equations:

$$\left(-\frac{1}{2}\nabla^2 + v_{eff}(r) - \epsilon_j \right) \varphi_j(r) = 0. \quad (14)$$

In this equation, the effective external potential v_{eff} is split into terms originating from non-interacting and interacting electrons [68]. The Hamiltonian is therefore divided correspondingly:

$$\hat{H} = \hat{T} + \hat{U} + \bar{V}, \quad (15)$$

where \hat{T} and \hat{U} represent the kinetic and the classical COULOMB potential for non-interacting particles, while the latter term \bar{V} has been defined as the exchange correlation potential. The total energy can then be derived from

$$E[n] = T[n] + U[n] + E_{xc}[n]. \quad (16)$$

In this equation, the exchange correlation E_{xc} includes the only approximations to be made. In its simplest form, the exchange correlation energy can be obtained from a uniform electron distribution in the so-called *local density approximation* (LDA) [69]. This approximation is exact for a uniform electron density and yields respectable results for slowly varying electron densities. More advanced, *generalised gradient approximations* (GGAs) have been derived to handle systems with electron distributions differing from slowly varying electron densities [70–73], and those used in this thesis are Perdew-Wang 91 (PW91) [71] and revised Perdew-Burke-Ernzerhof (RPBE) [73].

With these approximations, DFT has become a powerful tool for an *ab initio* description of many-particle systems. However, the GGAs fail when the basic assumption of slowly varying electron densities becomes increasingly inappropriate. In particular, VAN-DER-WAALS interactions are not included in the DFT formalism, nor into the vacuum evanescent electron densities at surfaces.

2.6.2 Effective-medium theory

EMT is a well-suited method when fast and simple calculations are needed to elucidate overall trends and give insight into the dominating mechanism behind observed effects. EMT [74, 75] is an approach aiming at describing interactions between atoms in a metallic system while reducing the computational effort

enormously. As EMT is based on experimental input, it is not an *ab-initio* method.

In this theory, the energy of a system is expressed as the embedding energy $E_c(i)$ for each atom i in a homogenous electron gas plus an atomic-sphere correction term $\Delta E_{AS}(i)$ and a correction term E_{1el} that includes the difference in the electron density to the model of free electrons:

$$E = \sum_i E_c(i) + \Delta E_{AS}(i) + E_{1el}(i). \quad (17)$$

The density of the homogenous electron gas is given by the average of the electron density of the surrounding atoms, that is, the energy of an atom is determined by the effect of the surrounding atoms. The embedding electron density $\bar{n}_i(s)$ around an atom is defined to depend exponentially on the radius s of a chosen sphere around the atom:

$$\bar{n}_i(s) \propto e^{-\eta s}. \quad (18)$$

Within this approach, the embedding energy can be calculated self-consistently, when values for several parameters – including the parameter η – are provided. For the specific geometry of a *face-centred cubic* (fcc) crystal, the number of unknown parameters can be reduced and the above-mentioned atomic-sphere correction term vanishes. Remaining parameters can be calculated from given structural data or derived from DFT, and all are available for a set of fcc metals [76].

With these parameters, the calculation of total energies of metallic systems is reduced to the determination of the number of the nearest neighbours, and surface or vacancy-formation energies are easily calculated by simply considering the change in the number of nearest-neighbour atoms. Other problems that can be handled by EMT are adatom diffusion, the calculation of reconstruction and relaxation energies and metal-atom adsorption [77].

The total energy for gold atoms as a function of coordination number as used in this thesis is listed below [76, 78].

n	12	11	10	9	8	7	6	5
$E(n)$	-3.81	-3.73	-3.66	-3.58	-3.48	-3.36	-3.20	-3.02

Table 1: Total energy $E(n)$ for gold atoms in an fcc crystal as a function of coordination number n derived from EMT [76].

3 Literature survey

Before presenting my own results, in this chapter I will introduce two concepts that are of relevance for this thesis, namely chirality and self-assembly. After the discussion of these two terms, I will give a short survey of earlier molecular-adsorption studies and self-assembly on various metal surfaces, with emphasis on sulphur-containing and chiral molecules.

3.1 Chirality

An object is referred to as *chiral* when it is non-superimposable with its mirror image. This holds when the mirror transformation is a non-identity operation. In particular, a molecule is *chiral* when the *enantiomers* – the different spatial configurations of the molecule – cannot be superimposed by any rotation or translation.

Chiral molecules are optically active, that is, the plane of linearly polarised light is rotated when the light passes through the molecule. Assuming one enantiomer of a given molecule rotates the polarisation of light clockwise, the other enantiomer turns it counter-clockwise by the same angle. A mixture of 50% of both enantiomers, which is referred to as the *racemic* mixture, causes no net rotation.

Hydrocarbons are chiral if they have an optically active carbon atom.⁵ Such a carbon atom is identified by its four different substituents. For α amino acids this is the second carbon atom, which is linked to the carboxylic group, the amino group, one hydrogen atom and the residue specifying the amino acid. In the case of glycine the residue is just a hydrogen atom and thus this amino acid is the only achiral α amino acid. Historically, the enantiomers of α amino acids

⁵A molecule can also have two or more optically active carbon atoms. In this case, 2^n different enantiomers exist, where n is the number of optically active carbon atoms.

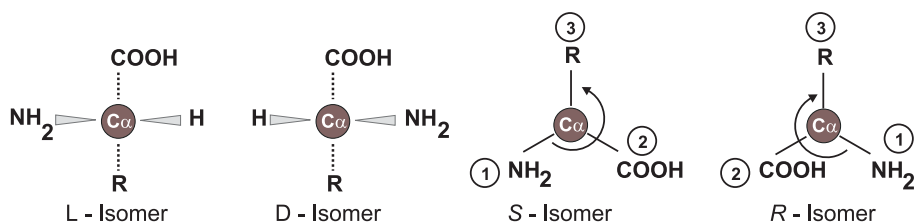


Figure 7: Notation for chiral molecules.

Definition for L and D amino acids and the more general definition for *S* and *R* molecules. In the latter case the hydrogen atom points into the plane.

are labelled with “D” (for “dexter”, lat. right) and “L” (for “laevus”, lat. left), depending on the conformation of the substituents around the second carbon atom, as depicted in Fig. 7. This system, which is still used for amino acids and sugars, is referred to as the FISCHER convention.

A newer notation, the CAHN-INGOLD-PRELOG convention, allows for the absolute determination of the chiral conformation of an enantiomer from its chemical structure. In the simplest case the substituents around the optically active carbon atom are ordered with respect to the atomic numbers of the atoms directly attached to the active carbon atom. The molecule is then viewed in such a way that the hydrogen atom is pointing away, as sketched in Fig. 7. Now, if an arrow drawn from the highest to the lowest atomic number turns clockwise, the molecule is called “*R*” (for “rectus”, lat. right), otherwise “*S*” (for “sinister”, lat. left). It is important to note that neither the descriptors D, L nor *R* and *S* are related to the actual physical direction in which the polarisation of light is turned.

In racemic crystals of chiral molecules, two different situations for the unit cell exist. One possibility is the formation of a homochiral unit cell, leading to homochiral crystal grains. The racemate of this type thus consists of a mixture of homochiral crystallites of the two enantiomers and it is referred to as a *racemic conglomerate*. The first experiment regarding the segregation of a racemic conglomerate was performed already in 1848 with tweezers under a light microscope by L. PASTEUR [79], who manually separated the enantiomers of sodium ammonium tartrate tetrahydrate, which crystallises in microscopic mirror-symmetric crystallites.

About 90% of all racemates belong, however, to another type of racemic crystals, *racemic compounds*, where the unit cell consists of both enantiomers. Also

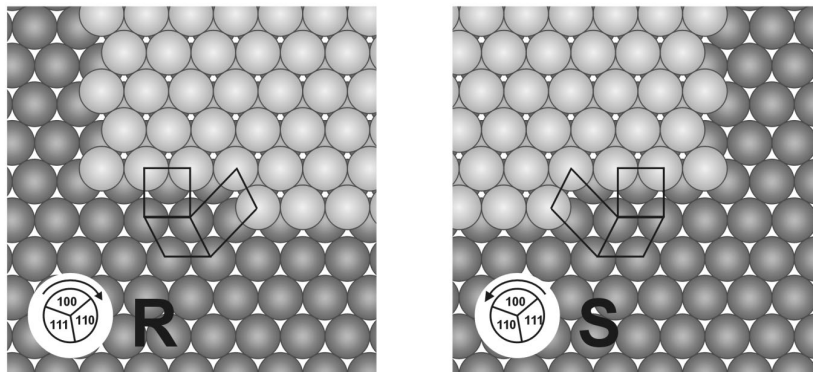


Figure 8: CAHN-INGOLD-PRELOG analogy to define the absolute chirality of a kinked fcc(111) surface.

A kink site of an fcc(111) surface and its mirror image. In accordance to the CAHN-INGOLD-PRELOG convention for molecules, the surface chirality is determined according to the surface density of the microfacets at the kink site.

the chiral molecule investigated in this thesis, cysteine, forms a racemic compound [80]. The existing database for two-dimensional adsorption systems is rather limited, but it appears, in contrast to the situation in bulk crystals, that most racemates studied so far segregate into homochiral domains upon adsorption onto a surface rather than forming overlayers with both enantiomers in the unit cell.

Recently, the inherent chirality of single-crystal surfaces has been exploited for enantioselective catalysis [81–85]. Although a flat single-crystal surface is mirror-symmetric and thus possesses no chirality, chirality can be induced by kink sites [86]. This is illustrated in Fig. 8, where two kinked, mirror-imaged surfaces are shown. In analogy to the CAHN-INGOLD-PRELOG convention for molecules, the absolute stereochemistry of the kink site is determined by the sequence of vicinal microfacets that meet at the kink site. If the sequence of microfacets ordered after decreasing density $(111) \rightarrow (100) \rightarrow (110)$ runs clockwise, the kink is referred to as an R kink, if it runs counter-clockwise, it is associated with an S kink site [86].

3.2 Self-assembly

Self-assembly is a phenomenon that has been recognised as a promising strategy for creating materials with controlled structures and properties at different length scales and has consequently attracted a lot of interdisciplinary research efforts.⁶

Main common aspects of self-assembly are the ability of preexisting components to move with respect to each other, the existence of an interaction between the individual components (such as VAN-DER-WAALS, electrostatic or hydrophobic interactions and hydrogen bondings or, more generally in the case of mesoscopic or macroscopic objects, gravitational attraction, magnetic, capillary or entropic interactions) and equilibration, which is usually required to obtain ordered structures.

Self-assembly is referred to as *static* when the system is stable once it is formed (e.g. folded proteins) or *dynamic* when it needs to dissipate energy to persist (e.g. biological cells). When the interaction of the self-assembling components with the environment determines the structure formation, the process can be described as *templated*. From a surface science point of view, however, it is difficult to draw a distinct border between templated self-assembly and the formation of a conventional adsorption structure.

Molecular self-assembly has been defined as the “spontaneous association of molecules under equilibrium conditions into stable, structurally well-defined aggregates joined by non-covalent bonds” [34]. Weak hydrogen bonds or dipole-dipole interactions are thus frequently central to molecular self-assembly. Usually, the molecules must be able to move with respect to each other, and equilibrium is required, as no ordered structure can be formed if the molecules stick firmly to each other when they collide [35].

3.3 Molecular adsorption studies

3.3.1 Molecular self-assembly

This review is limited to some prominent studies exemplifying self-assembly among molecules at surfaces into quasi one-dimensional and two-dimensional structures. The formation of self-assembled molecular surface structures can be influenced by an intelligent design of the molecules involved [87] or by changing the properties of the substrate surface. In a recent work, the clever use of functional groups has been demonstrated to allow the rationally controlled formation of desired structures of porphyrin molecules [88]. Depending on the

⁶For a recent review see the special *Science* issue “Supramolecular Chemistry and Self-assembly” **295** (2002).

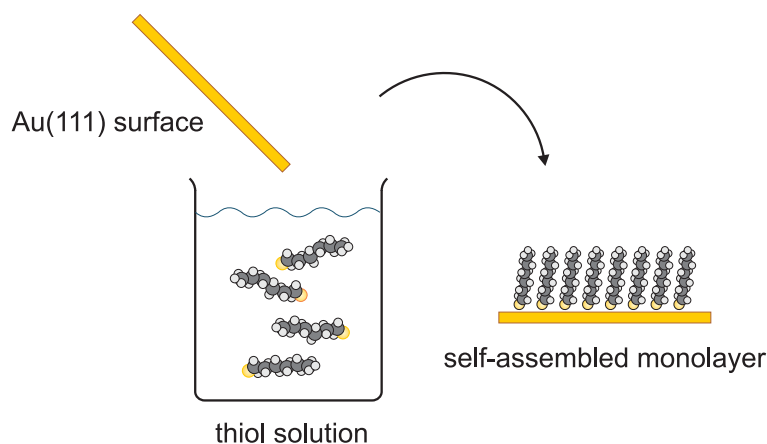


Figure 9: Self-assembled monolayer of alkanethiols on a Au(111) surface.

After dipping a Au(111) substrate into an alkanethiol solution the surface is believed to be covered with an ordered alkanethiol film in the so-called “standing-up” phase.

number and position of substituents, trimers, tetramers and extended molecular chains form on a Au(111) surface due to dipole-dipole interactions between the substituents on the porphyrin molecules. Various other approaches to form self-assembled “one-dimensional”, wire-like structures have been presented [89–96]. These studies include a demonstration of the uni-directional growth of molecular chains on a silicon surface [96], where the interaction with the surface directs the growth of the molecular chains. In another study, the selectivity and directionality of hydrogen bonds have been exploited for the formation of molecular double rows on a Ag(111) surface [90–92].

Apart from uni-directional molecular structures, also molecular clusters have been observed based on hydrogen bonds, such as clusters of nitro-naphthalene molecules on a Au(111) surface [97]. These molecules aggregate into decamers, undecamers and tetramers similar to the geometric shell closing that has been observed in atomic clusters.

The formation of extended, two-dimensional self-assembled structures on surfaces has now been studied for decades, and monolayers of alkanethiols on Au(111) in particular have become an archetype for *self-assembled monolayers* (SAMs). The term SAM originates from structures achieved at liquid-air

interfaces by the LANGMUIR-BLODGETT technique [98], where the ordering is governed solely by molecule-molecule interactions. Self-assembly of alkanethiols on gold, on the other hand, is driven by both the formation of strong sulphur-gold bonds and weak VAN-DER-WAALS forces between the alkane chains of the molecules. As the surface interaction crucially influences the structure formation, this type of self-assembly can be referred to as “templated” [35].

Due to the ease of preparation, alkanethiol SAMs produced by dipping a gold sample into a solution have been used as a standard system for studying SAMs and to functionalise surfaces (Fig. 9). One of the most extensive STM studies in UHV was carried out by G. POIRIER on Au(111), describing the transition from the low-coverage “lying-down” phase to the high-coverage “standing-up” phase [47, 99, 100]. A substantial number of UHV studies have been performed in order to disclose the adsorption structures of different thiols on Au(111) by means of LEED [101], *helium-atom scattering* (HAS) and TPD [102], STM [103] and various other techniques [46, 104]. Depending on the alkane chain length, the lying-down phase adopts different superstructures, whereas the standing-up phase is frequently reported to form a $(\sqrt{3} \times \sqrt{3})R30^\circ$ structure on Au(111) along with a so-called $c(4 \times 2)$ superstructure on top that has been motivated by a closer proximity of the sulphur atoms in the $c(4 \times 2)$ structure compared to the ordinary $(\sqrt{3} \times \sqrt{3})R30^\circ$ structure. In this ordered, saturated phase, the molecules are believed to chemisorb by forming covalent bonds between the sulphur atoms and the gold surface after dissociation of the hydrogen atom of the mercapto group. After this dehydrogenation, the molecules are referred to as *thiolate*. A more detailed review on alkanethiol SAMs is given in chapter 7.

3.3.2 Sulphur-containing molecules

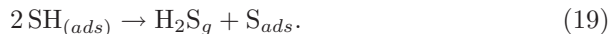
A general motif of the molecules investigated in this thesis is that they contain sulphur and that the bonding and orientation of the molecules depend on the interaction of the sulphur atoms with the surface. For that reason, a review on adsorption studies of several sulphur-containing molecules is given here with emphasis on Au(111) and Au(110) surfaces, and including theoretical papers elucidating the binding of sulphur to gold surfaces.

The adsorption of sulphur and sulphur-containing molecules on gold and various other surfaces has been the subject of many studies in recent years (see [105–107] and references therein) for various reasons. First, the sulphur-gold interaction is believed to influence the self-assembly in alkanethiol SAMs. Although, as mentioned above, the alkanethiol SAMs on gold are commonly reported to form a $(\sqrt{3} \times \sqrt{3})R30^\circ$ structure, several issues remain unclear such as the exact adsorption position of the sulphur atoms, the reason for the $c(4 \times 2)$

superstructure, and the driving force for a frequently observed vacancy formation in the gold substrate, calling for a more detailed understanding of the sulphur–gold interaction. These monatomically deep gold vacancies are commonly referred to as “etch pits” and have been explained by the dissolution of gold atoms in the liquid when preparing the alkanethiol SAM by dipping the gold sample into a thiol solution. However, vacancies in the gold surface also form after molecular-beam deposition of alkanethiols in UHV, demonstrating that these vacancies are a rather general phenomenon associated with SAM formation. Second, sulphur-containing molecules are now routinely used to anchor biomolecules at gold surfaces [108–110]. Third, the interaction of sulphur and sulphur-containing species with metal surfaces is technologically important to understand catalyst poisoning and designing hydrodesulphurisation processes [111,112].

The adsorption of sulphur on metal surfaces is usually described by the formation of a strong covalent bond, including perturbations in the electronic structure of the metal surface due to charge transfer from the metallic d -band to the sulphur atom, which, in turn, significantly changes the chemical and especially catalytic properties of the surface [113,114].

Adsorption of H_2S from the gas phase is commonly used as a method of depositing sulphur in UHV. Most adsorption studies on gold have been performed on the (111) facet due to the ease of preparing this facet and its practical importance [105,115]. Temperature-programmed desorption [105] disclosed that H_2S adsorbs only at low temperatures and desorbs already at temperatures around 160 K as intact molecules. When irradiated with electrons, however, the molecules decompose at the surface into adsorbed SH groups and hydrogen. While the hydrogen desorbs molecularly, the SH groups remain on the surface, and heating leads to the following reaction:



Atomic sulphur is left behind on the surface, which is reported to desorb at a temperature above 900 K.

In contrast to these results, either a high H_2S flux or an environment different from UHV seem to lead to H_2S adsorption also at room temperature, as has been shown in an STM study, where the adsorption of H_2S onto Au(111) from a dry He atmosphere was investigated [115]. While high H_2S concentrations have been found to corrode the surface severely, reducing the H_2S concentration yielded domains of a rectangular ($2 \times 3\sqrt{3}$) structure with three molecules in the unit cell. Intriguingly, this structure is different from the $(\sqrt{3} \times \sqrt{3})R30^\circ$ pattern found for alkanethiols on Au(111), although the adsorbed SH layer may be viewed as the simplest alkanethiol SAM in which the alkane backbone

is absent. This may be taken to highlight the influence of the alkane chains during the SAM formation.

Other sulphur-containing molecules, such as thiophene, sulphur dioxide and methanethiol, have been studied by STM, TPD and XPS on Au(111) [116], revealing very different adsorption behaviours for these three molecules. Whereas thiophene and sulphur dioxide – similar to H₂S – desorb as intact molecules at rather low temperatures, methanethiol is found to desorb dissociatively forming dimethyl disulphide and methyl radicals. From XPS data it is concluded that the sulphur–hydrogen bond cleavage in methanethiol takes place already at 100 K [116]. At this low temperature, chemisorbed thiolate species, CH₃S, co-exist with physisorbed thiol molecules. At slightly higher temperatures (200 K) also atomic sulphur is found, and this is the only species remaining at the surface above 600 K. In agreement with previous studies, the atomic sulphur is stable until 900 K.

Considerably fewer studies have been performed on other gold facets such as Au(100) [117] and Au(110) [118–120]. The hydrogen-sulphide adsorption on Au(110) has been investigated by means of LEED and *auger electron spectroscopy* (AES) [118], and TPD [119], revealing that almost all H₂S molecules stay intact when desorbing from a Au(110) surface.⁷ It has, however, been shown that the sulphur–hydrogen bond cleavage can be observed on Au(110) for high H₂S pressures [118], leading to the conclusion that the onset temperature for desorption coincides with the temperature needed for H₂S dissociation on Au(110). As in the case of Au(111), electron irradiation causes decomposition to SH_(ads) and adsorbed hydrogen H_(ads), which recombines to molecular H_{2(g)} and desorbs at 215 K. Adsorbed SH_(ads) has been found to dissociate above 250 K, following the reaction path given in equation 19. A LEED investigation of the sulphur structure on Au(110) disclosed a p(1 × 2) pattern for low sulphur coverage, while a c(4 × 2) structure has been observed for higher coverages. At intermediate coverages both structures have been found to co-exist.

Several theoretical studies exist on the adsorption of sulphur-containing molecules, mainly alkanethiols, on gold [121–123]. DFT calculations generally find rather weak sulphur–gold bonds compared to experimental values. In a comparative adsorption study, the binding energy and adsorption sites of sulphur, mercapto and methylthiolate on Au(111) have been investigated [121]. While atomic sulphur is found to adsorb on the high-coordinated fcc hollow sites, the adsorption site moves towards a bridge and bridge-like position when an

⁷This is in contrast to a number of more reactive surfaces such as polycrystalline Cr, Pt(111), Rh(100), Cu(100), Ru(100) and Ni(100) where the H₂S dissociation has been observed (see references in [105]).

additional hydrogen atom or methyl group is attached to the sulphur atom.⁸ The adsorption of atomic sulphur is clearly exothermic with an energy gain of about -3.9 eV (PW91). However, the dissociation of hydrogen from hydrogen disulphide and methanethiol requires nearly as much energy (+1.9 and +1.6 eV, respectively) as is gained subsequently by the adsorption of mercapto and methylthiolate to the gold surface (-2.0 and -1.7 eV).

Recently, extended surface reconstructions have been suggested to account for both the strong binding of the sulphur and the gold-vacancy formation [124,125]. In the latter study, the adsorption of methylthiolate has been found to be stabilised by -0.8 eV on a so-called “honeycomb”-reconstructed Au(111) surface, compared to the energy of +0.6 eV needed for the vacancy formation.

3.3.3 Adsorption of amino acids

The adsorption of amino acids on metal surfaces under clean UHV conditions has attracted considerable attention, mainly focussing on glycine and alanine. Apart from a few studies on Pt(111) [126,127], most of the UHV adsorption studies on the simplest amino acid, glycine ($\text{NH}_2\text{-CH}_2\text{-COOH}$), carried out so far have been performed on Cu(110) with a variety of surface-science techniques, including spectroscopic [128,129] and diffraction-based [128,130] techniques as well as STM [131]. These studies resulted in a fairly detailed understanding of the adsorption of this molecule on Cu(110). Large-scale changes of the surface morphology upon glycine adsorption have been reported by several groups. The Cu(001) surface has been found to become faceted by step-bunching after glycine adsorption, indicating a considerable mass transport [132].

In the case of the next-larger amino acid alanine, ($\text{CH}_3\text{-CH(NH}_2\text{)-COOH}$), compared to glycine one hydrogen atom is replaced by a methyl group, turning the molecule into a chiral species. Adsorption studies of alanine have been performed on Cu(001) [133] and Cu(110) [134].

The amino acid studied in this thesis, cysteine ($\text{HS-CH}_2\text{-CH(NH}_2\text{)-COOH}$), resembles alanine except for the sulphur-containing mercapto group ($-\text{SH}$), substituting one hydrogen atom in the methyl group of alanine. Only few STM-based investigations of cysteine adsorption on Au(111) have been performed so far. In all these cases, however, deposition was done from solution by dipping a Au(111) surface into an organic or aqueous solvent containing the amino acid [135–142], apart from one investigation where cysteine adsorption was performed in UHV on a polycrystalline surface [143]. A more detailed

⁸The influence of the adsorption site has been found to be relatively strong in the case of atomic sulphur, yielding a difference of 1.5 eV between the on-top and the bridge site, while it is not as pronounced for the mercapto group and methylthiolate, where the difference is only about 0.3 eV (PW91).

discussion of these investigations is given in chapter 6. In chapter 4 cysteine adsorption studies that have been carried out on Au(110) are presented.

3.3.4 Inducing surface chirality by molecular adsorption

Surfaces with chiral properties are of interest in the field of enantioselective catalysis, as the enantiospecific interaction with a chiral surface may be utilised to increase the enantiomeric excess in chemical reactions. A simple approach to fabricating chiral surfaces is adsorbing chiral molecules onto surfaces as discussed by R. RAVAL *et al.* in the case of tartaric acid on Cu(110) and Ni(110) [144–146]. Many experiments have, however, been performed with an achiral species that becomes chiral only upon confinement to the two-dimensional surface plane. These molecules are referred to as *prochiral* molecules. The majority of the studies was devoted to the segregation of chiral or prochiral molecules into homochiral domains upon monolayer deposition [147–150]. In contrast to the situation in the bulk, it appears that most racemates studied so far segregate into homochiral domains upon adsorption, rather than forming superstructures with both enantiomers in the unit cell.

Among other molecules, the adsorption of a number of chiral amino acids has been investigated recently on metal surfaces by various techniques such as STM, TPD, RAIRS and XPS, including alanine [133, 134], lysine [151, 152] and phenylglycine [153]. A detailed discussion of all these studies is beyond the scope of this review. The main finding, however, is the segregation of the racemic mixture into homochiral domains upon monolayer adsorption. The formation of an extended molecular network via hydrogen bonds, VAN-DER-WAALS forces or dipole-dipole interactions is the origin of the observed homochiral domains [154–156], as a mirrored molecule with a different spatial morphology would destroy the periodicity of the network.

Only few studies demonstrate self-assembly within submonolayers of chiral or prochiral molecules. The already mentioned hydrogen-bonded molecular chains [90, 91] and clusters [157] appear to exhibit chirality when confined to two dimensions. The latter study also represents a “nano-analogue” of PASTEUR’s separation experiment [79] by utilising the manipulation abilities of the STM: The chiral clusters have been moved laterally with the STM tip, separating the two enantiomers on the Au(111) surface.

The absolute chirality of individual molecules has been disclosed in the case of the prochiral molecule *trans*-butene on a silicon surface, using the ultimate resolution capability of the STM [158].

Recently, the modification of silica nanotubes with antibodies has been proven to selectively transport certain enantiomers of a drug [159]. Another strategy is

to employ the ability of adsorbed chiral molecules to restructure the underlying surface, thereby creating chiral centres on the surface [152,160].

Finally, high Miller index surfaces of pure crystals possess intrinsic chirality due to chiral kink sites [81–85], and the enantioselectivity of these surfaces has been demonstrated by the enantioselective oxidation of L and D glucose on Pt(634)^S and Pt(634)^R [86,161].

4 Cysteine on Au(110)

4.1 Introduction

In this introduction both the dimensions and special properties of the Au(110) surface and the characteristics of cysteine will be presented briefly. This is followed by an overview of the various cysteine structures observed on Au(110) in order to introduce the following sections of this chapter.

4.1.1 Au(110)

In contrast to a large number of metals whose surfaces are stabilised by a small surface relaxation, the surfaces of some metals reconstruct into new structures with unit cells different from the bulk [50, 162, 163]. In the case of the three *5d* fcc metals Au, Pt and Ir, this complex rearrangement has been explained by the reduced repulsion of the *d*-band electrons at the surface compared to the bulk [162].

The Au(110) surface has a rectangular unit cell with the dimensions $d_1 = 2.88 \text{ \AA}$ and $d_2 = 4.08 \text{ \AA}$. This facet of gold is a well-known example of a (1×2) *missing-row* reconstructed surface [50, 51, 164, 165], and the main characteristic of this particular surface reconstruction is the formation of energetically favourable (111) microfacets, which leads to the removal of every second atomic row along the $[\bar{1}\bar{1}0]$ direction, as shown in Fig. 10a. The missing-row reconstruction is routinely observed in the STM images, leading to bright, equidistant stripes separated by darker regions, while atomic resolution within the atomic rows is more difficult to obtain, but can be achieved, as demonstrated in Fig. 10b. The corrugation amounts to 0.6 - 1.0 \AA perpendicular to the $[\bar{1}\bar{1}0]$ direction and to about 0.2 \AA within the close-packed gold rows.

The (1×2) missing-row reconstruction makes the formation of steps energetically favourable and leads to large-scale surface patterning, the so-called *fish-scale pattern* [166], which is shown in Fig. 10c.

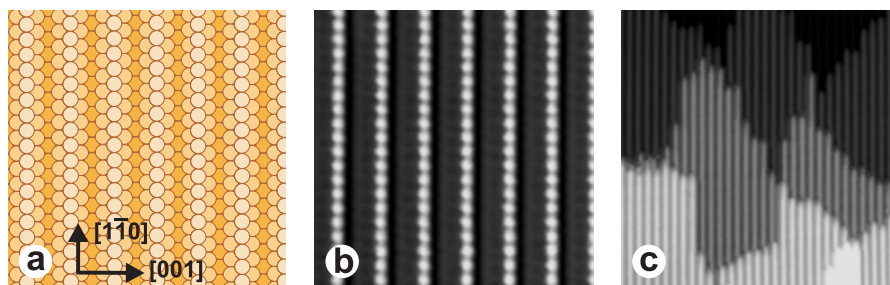


Figure 10: The (1×2) missing-row reconstructed Au(110) surface.

(a) Model of the reconstructed surface. Light atoms lie above dark ones.

(b) Atomic resolution within the gold rows. Image size: $51 \text{ \AA} \times 56 \text{ \AA}$.

(c) Large-scale image showing the so-called *fish-scale pattern*. Image size: $277 \text{ \AA} \times 299 \text{ \AA}$.

The gold surfaces used in this work have been prepared by repeated cycles of Ar^+ ion sputtering at 1.5 keV and annealing at 800 K. Typical contaminants found in gold are calcium and silicon [167], and even very low impurity concentrations lead to perturbations in the (1×2) missing-row reconstruction, resulting in various $(1 \times n)$ reconstructions [51]. In the crystals used here, calcium has been identified as the main impurity by AES. Annealing of the sample in an oxygen atmosphere of $\sim 10^{-6}$ mbar followed by ordinary cleaning cycles has been found to efficiently remove the calcium from the surface region.

Unless otherwise specified, the images presented in this thesis were recorded with -1.2 V bias on the sample using a tunnelling current of around -0.1 nA. These conditions allow for sufficient tunnelling from filled sample states into empty tip states to achieve high resolution while, on the other hand, the tip is still sufficiently far away to enable stable imaging.

4.1.2 Cysteine

Cysteine ($\text{HS-CH}_2\text{-CH(NH}_2\text{)-COOH}$, see model in Fig. 11) is one amino acid out of the set of 20 amino acids found in naturally occurring proteins. At room temperature, cysteine is a white, crystalline powder that melts and decomposes at ~ 490 K. Its relative molecular weight is 121.16. Cysteine in solution is cationic, anionic or zwitterionic depending on the pH value of the solution

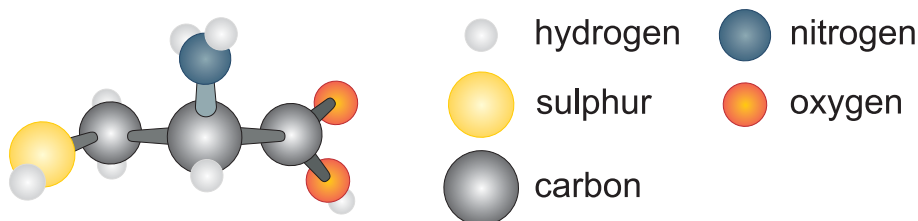


Figure 11: Ball model of the cysteine molecule.

as are all amino acids, and the isoelectric point for cysteine is at a pH value of 5.06 [168].

As discussed in section 3.3.3, the adsorption of cysteine onto metal surfaces has recently been studied in a number of instances, mainly on Au(111) [135–143]. A detailed discussion of cysteine adsorption studies on Au(111) is presented in chapter 6.

Upon adsorption on metal surfaces, the hydrogen atom of the mercapto group (HS^-) is often dissociated, enabling a strong covalent bond to be formed between the sulphur atom and the metal surface. The dehydrogenated molecule ($\text{S-CH}_2\text{-CH(NH}_2\text{)-COOH}$) is referred to as *cysteinate*, in analogy to the terminology for thiols. Cysteine is routinely used to link proteins to gold surfaces: In proteins, cysteine molecules are often linked via a disulphide bond, forming *cystine* ($\text{HOOC-CH(NH}_2\text{)-CH}_2\text{-S-S-CH}_2\text{-CH(NH}_2\text{)-COOH}$). Upon adsorption onto gold, the disulphide bond breaks, enabling the binding of cysteinate via the formation of a strong sulphur–gold bond [108,109]. Similarly, cysteine is commonly used to link protein strands to a cantilever when performing protein unfolding experiments [110].

4.1.3 Overview of the cysteine adsorption on Au(110)

Depending on the cysteine coverage and temperature, a rich variety of structures have been identified on Au(110)-(1 × 2), whose formation is influenced by the special geometry and reactivity of this particular gold facet. In the following, a brief overview of the different structures will be given to illustrate the multitude of observed molecular structures and to introduce the upcoming sections that present the details of the cysteine-adsorption experiments.

Upon cysteine deposition at low temperatures, individual cysteine molecules exist on the surface, agglomerating into disordered molecular islands of various sizes. When increasing the substrate temperature to about 260 K, however,

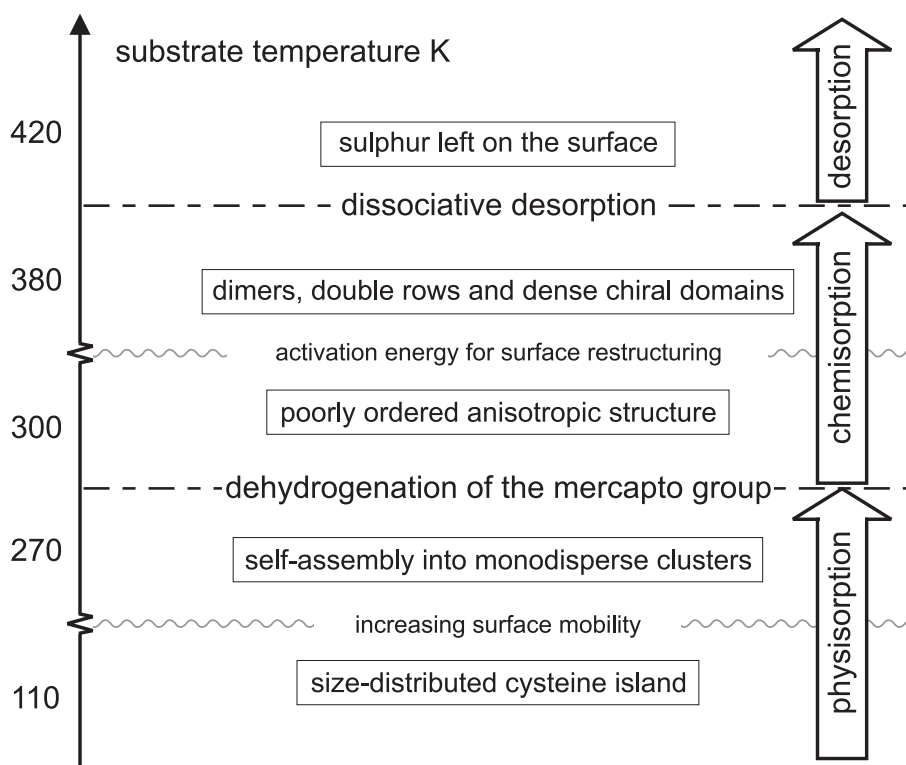


Figure 12: Overview of the cysteine structures on Au(110)-(1 × 2).

the molecules rearrange and self-assemble into monodisperse molecular clusters. This self-assembly process will be discussed in section 4.7. At this low temperature, the molecules are physisorbed on the surface and the hydrogen atom of the mercapto group is not yet dissociated, preventing from a strong covalent sulphur–gold bond to be formed.

Increasing the temperature above 270 K, however, causes the nanoclusters to dissolve. At this temperature, the dehydrogenation of the cysteine molecules is introduced and the molecules are chemisorbed on the surface via a covalent sulphur–gold bond, forming a new structure, which is stable up to 380 K. This room-temperature structure consists of poorly ordered, anisotropic agglomerates of cysteine that have been studied by STM and RAIRS (section 4.2). Further annealing of the low-coverage cysteine layer at 380 K supplies the

activation energy for adsorbate-induced surface reconstruction. The possibility of an adsorbate-induced restructuring of the substrate surface allows new structures to be formed. An interesting observation is the formation of chiral molecular dimers. These dimers appear to be a very interesting model system that has allowed us to study the important concepts of chiral recognition at the molecular scale, as presented in section 4.3. The molecular pairs are found to coexist with a chain-like molecular structure, consisting of double rows of cysteine that are aligned along the $[1\bar{1}0]$ direction (section 4.4). When the coverage is increased to a few percent of a monolayer, dense molecular islands form on the surface, while the remaining surface is covered by the molecular pairs and double rows. The individual cysteine pairs align in an ordered two-dimensional array on the surface, where the gold surface exhibits a complex adsorbate-induced restructuring. Indications exist that the dense cysteine domains grow on top of these ordered arrays, as will be discussed in section 4.5. Even higher coverages result in the formation of a full layer of cysteine on the surface that adopts a $c(2 \times 2)$ structure when annealed at 330 K.

Upon annealing at temperatures above 420 K, dissociative desorption is induced, leaving atomic sulphur behind on the surface. This sulphur structure, which exhibits a $c(4 \times 2)$ pattern, is fully developed after annealing above 440 K, where the surface shows a substantial refaceting. In the temperature interval between these two temperatures, a surprising phenomenon has been observed: The chiral symmetry appears to break as the remaining cysteine pairs from a racemic mixture have been identified not to reflect a 1:1 distribution of L and D cysteine. The possible origins of this chiral symmetry breaking will be discussed in section 4.6.

4.2 Room-temperature structures

4.2.1 STM results

Upon submonolayer evaporation of L cysteine onto a Au(110)-(1×2) surface held at room temperature, a poorly ordered, anisotropic structure of agglomerated cysteine molecules is observed, as shown in Fig. 13a. Rows of cysteine are found on the surface, aligned along the $[1\bar{1}0]$ direction with an average apparent height of about 3 Å. A zoom-in on these agglomerates reveals some internal structure, but still shows only limited ordering (Fig. 13b).

4.2.2 RAIRS experiments

To complement the room-temperature STM data with information on the bonding and orientation of the molecules on the surface, infrared spectra have been obtained. The infrared spectra were recorded while L cysteine was evaporated onto Au(110)-(1 × 2) held at room temperature. Although the pres-

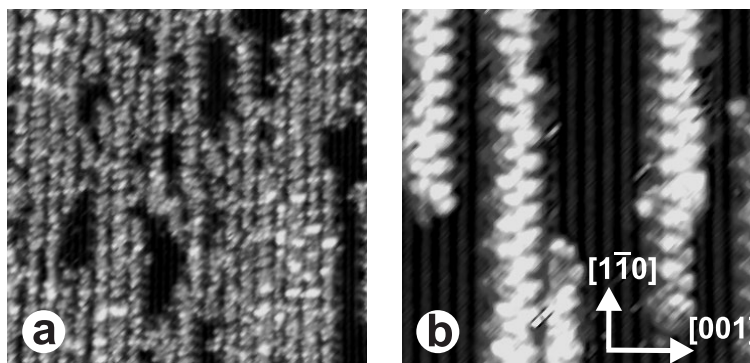


Figure 13: STM images after evaporation of L cysteine on Au(110) held at room temperature.

(a) Terrace of a gold (110)-(1×2) surface after deposition of L cysteine at room temperature. The surface is covered with cysteine molecules, arranged in rows along the $[1\bar{1}0]$ direction. In some areas, the close-packed rows of the gold substrate are still visible (dark regions in the STM image). Image size: 400 Å×400 Å. (b) Zoom-in on the as-deposited structure showing some internal resolution within the cysteine rows. Image size: 160 Å×160 Å.

ence of a surface and a different bonding environment compared to the bulk form might somewhat alter the precise position of the absorption peaks, the assignment of the observed cysteine vibrational modes can be guided by comparison with spectra recorded from bulk cysteine and related molecules such as glycine ($\text{CH}_2(\text{NH}_2)\text{-COOH}$) and mercaptopropionic acid ($\text{HS-CH}_2\text{-CH}_2\text{-COOH}$) [128, 168–170]. In the following, some prominent adsorption peaks of these spectra known from literature are briefly summarised. Depending on the state of ionisation, the spectra exhibit vibrations originating from the non-ionic carbonyl (C=O) and amino (NH_2) groups or from the anionic carboxylate (CO_2^-) or cationic ammonium (NH_3^+) groups. In the solid form, cysteine is zwitterionic, which is why the otherwise strong C=O stretching peak around 1720 cm^{-1} and the stretching and scissoring modes from the amino group are not present. Upon vapor deposition, the cysteine molecules are thought to exist in their non-ionic form. No carboxylate or ammonium bands should therefore be observed in the spectra presented here. Stretching modes from the amino group are usually found around 3360 cm^{-1} and 3295 cm^{-1} for asymmetric and symmetric stretching, respectively. A vibrational peak originating from the S-H stretching is commonly observed around 2550 cm^{-1} , while the normally strong NH_2 scissoring mode is obtained at 1590 cm^{-1} . Degenerate and symmetric deformation of NH_3^+ result in peaks at 1640 cm^{-1} and 1540 cm^{-1} , and CO_2^- asymmetric and symmetric stretching is located around 1600 cm^{-1} and 1400 cm^{-1} . C-H stretching vibrations are known to result in a broad band around 3000 cm^{-1} .

The spectra presented here were obtained at a cysteine background pressure of $2 \cdot 10^{-9}$ mbar. At this pressure, a peak around 1650 cm^{-1} is the first to appear, and after ~ 10 min of dosing time, this peak reaches a saturation intensity of $\sim 0.4\%$ in reflectance.

Typical room-temperature spectra are shown in Fig. 14, recorded (a) after 7 min deposition and (b) well after saturation (after 49 min). Apart from a strong peak at 1650 cm^{-1} , a broad band around 3030 cm^{-1} is obtained. A very weak band at 1710 cm^{-1} can be seen in the inset, resulting in a shoulder of the band at 1650 cm^{-1} . Additionally, a small peak at 1520 cm^{-1} , a double peak at 1425 and 1390 cm^{-1} and a rather small peak around 1130 cm^{-1} are observed. Interestingly, no peak was found at 3360 cm^{-1} , nor at 2550 cm^{-1} . Comparison with unsaturated spectra shows that the observed peaks only change in intensity, not in position, upon increasing coverage.

The presented spectra offer some important insight into the bonding configuration of cysteine adsorbed onto Au(110) at room temperature, although an unambiguous assignment of the observed absorption peaks largely remains unresolved.

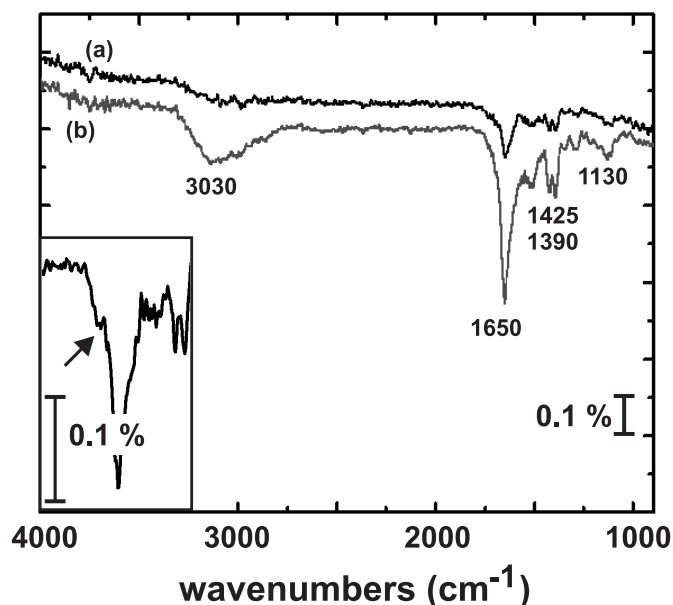


Figure 14: RAIRS spectrum of cysteine adsorbed onto Au(110) held at room temperature.

(a) Spectrum recorded after 7 min cysteine deposition. (b) Spectrum showing the saturated vibrational bands for cysteine adsorbed onto Au(110)-(1×2) after a deposition time of 49 min at a background pressure of $2 \cdot 10^{-9}$ mbar. In the inset, a zoom-in of peak at 1650 cm^{-1} is shown, and an arrow points to the small peak at 1710 cm^{-1} .

The adsorption geometry seems to be independent of the coverage, as the observed peaks only change in intensity, not in position, upon increasing coverage at room temperature. The absence of the S-H stretching mode band (2550 cm^{-1}) suggests that the mercapto group is involved in the bonding to the gold surface, thereby preventing an S-H vibration to be seen. This is a strong indication that the mercapto group is dehydrogenated, that is, the transition from thiol to thiolate has occurred at room temperature.

Furthermore, since the spectrum given in Fig. 14b represents a saturation spectrum, no bilayer cysteine growth is observed at room temperature, as bi- and multilayers should exhibit an S-H vibration peak.

As mentioned above, the C=O stretching mode located around 1730 cm^{-1} usually results in a very strong absorption peak in the infrared spectrum. In the present case, at most only a very weak peak (hidden by the strong peak at 1650 cm^{-1}) is observed, which can be explained by the metal surface selection rule. For a parallel alignment of the carboxylic group relative to the gold surface, the C=O stretching dipole lies parallel to the surface and is, therefore, forbidden in the RAIR spectrum. The existence of the small peak at 1710 cm^{-1} could be explained by the fact that the plane formed by the bonds between the carbon and oxygen atoms is not perfectly parallel to the gold substrate surface. Then, however, the peak should grow in accordance with the other peaks when increasing the coverage. Since this peak rather seems to saturate before the other peaks, the presence of the C=O stretching mode may be due to cysteine adsorption at step edges and defects, where the geometrical constraints may change the cysteine adsorption geometry compared to the adsorption on the terraces.

In summary, the combined STM and RAIRS study showed that cysteine forms only poorly ordered, anisotropic molecular rows at room temperature, aligned with the $[1\bar{1}0]$ direction of the substrate surface. RAIRS measurements reveal no S-H stretching vibration, indicating that the mercapto group is dehydrogenated, i.e., the molecules have undergone a transition from the thiol (cysteine) to the thiolate (cysteinate) species at room temperature. As in the case of alkanethiols on Au(111), cysteine is anchored to the surface via the sulphur atom. Additionally, the carboxylic group of the molecule is found to align parallel to the surface, independently of the coverage. Finally, the formation of molecular bilayers is not observed at room temperature.

4.3 Molecular chiral recognition

4.3.1 STM results

As presented in the previous section, submonolayer deposition of L cysteine on Au(110) held at room temperature results in poorly ordered, anisotropic agglomerates of cysteine molecules (Fig. 13). This situation, however, changes upon annealing of the surface at 380 K for about 15 min [171]. The molecular agglomerates dissolve and the molecules diffuse on the surface, rearranging into new molecular structures, which eventually desorb upon further annealing at 440 K. For submonolayer coverages, a dilute cysteine phase is observed as shown in Fig. 15a. In this image, the reconstructed gold substrate is recognised by the dark stripes running along the $[1\bar{1}0]$ direction that originate from the atomic troughs separating the close-packed gold rows. Additionally, bright protrusions exist on the surface at the sides of the close-packed gold rows. These protrusions always exist as pairs with a centre-to-centre distance of about 9 Å, and the dimension of an individual protrusion is about 7 Å (see height profile in Fig. 15c), corresponding to the size of a cysteine molecule. The cysteine molecules thus arrange themselves in molecular pairs on the Au(110) surface and no unpaired protrusions interpretable as isolated molecules are present on the surface. The main axis through these double-lobe features is always rotated 20° clockwise with respect to the $[1\bar{1}0]$ direction. This breaks the mirror symmetry of the system and is therefore an expression of the chirality of the molecules. To confirm this, the same experiment has been performed with the other enantiomer, D cysteine. The STM image shown in Fig. 16, obtained with D cysteine, discloses similar pairs, but now exclusively rotated counter-clockwise. The fact that the molecules retain their chirality within the molecular dimers demonstrates that they cannot be fragmented to any significant degree.

Having observed the molecular dimer formation for the pure enantiomers, the question arises what happens when the racemic mixture is deposited such that both enantiomers are present at the surface at the same time. Upon DL cysteine deposition, molecular dimers are again formed, as depicted in Fig. 17, which are identical to those obtained for the pure enantiomers. These dimers exhibit either the LL dimer signature, when being rotated clockwise, or the DD dimer counter-clockwise rotation. Thus, by comparison with the STM experiments performed with the pure enantiomers, the absolute chirality of the individual cysteine dimers is obtained by STM [158].

Most importantly, no other structures such as pairs with both lobes on one side of the close-packed gold row are observed, even though a total amount of more than 6200 pairs was examined. This indicates that when the individual

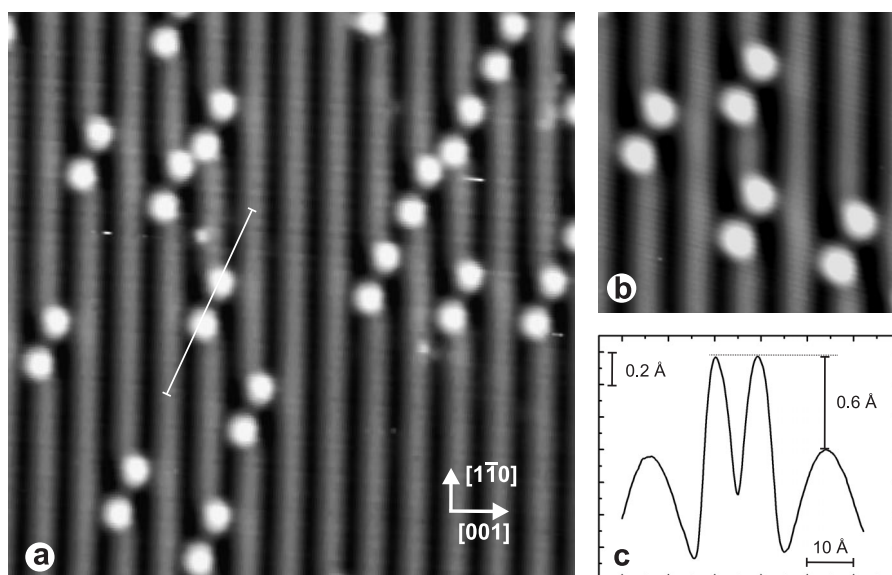


Figure 15: Low coverage of L cysteine on Au(110) after annealing at 380 K.

(a) Au(110)-(1 \times 2) surface after submonolayer deposition of L cysteine and subsequent annealing at 380 K. Double-lobe, bright protrusions are seen to have their main axes exclusively rotated 20° clockwise. The centre-to-centre distance between the protrusions in the pair is about 9 Å and the extent of the individual protrusion is around 7 Å. Image size: 113 Å \times 122 Å. (b) High-resolution image of the L cysteine pairs. Image size: 49 Å \times 53 Å. (c) Height profile over a cysteine pair. The position of the profile line is indicated by the white line in (a). The apparent height of the dimer is about 0.6 Å with respect to the height of the topmost gold row.

molecules⁹ diffuse on the surface and collide with other molecules, the chiral sense of the molecules is recognised and dimerisation is excluded for heterochiral cysteine pairs. Thus, the experiments show that the cysteine molecules

⁹Evidence that the molecules are adsorbed individually is given in section 4.7 where low-temperature adsorption experiments are presented. For adsorption at 110 K, islands of individual cysteine molecules are formed, ruling out the possibility of preexisting cysteine dimers that might have been formed in the gas phase.

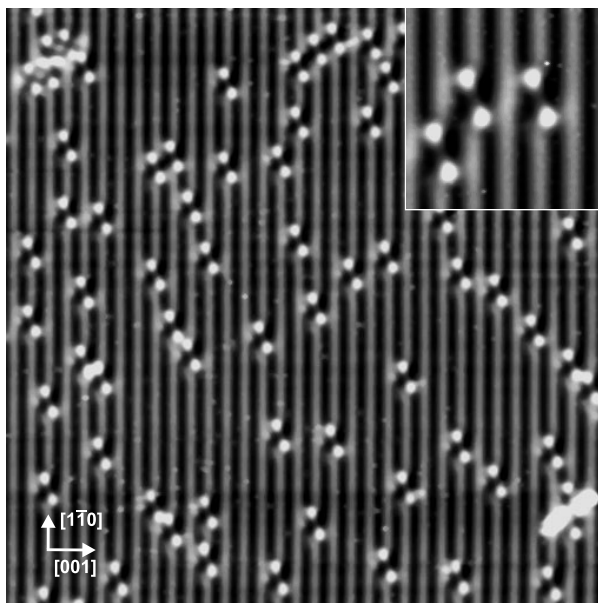


Figure 16: D cysteine dimers on Au(110).

Molecular pairs of D cysteine with the opposite, counter-clockwise rotation.
Image size: $270 \text{ \AA} \times 290 \text{ \AA}$. Inset: High-resolution image of the molecular pairs.
Image size: $49 \text{ \AA} \times 53 \text{ \AA}$.

exclusively bind to a molecule of the same conformation although the exact same functional groups are present in both enantiomeric forms.

The pairs are immobile at room temperature, and it was not possible to manipulate them with the STM tip, even when applying a high tunnelling current up to 3 nA and a tunnelling bias down to 30 mV, corresponding to a tunnelling resistance of only 10 M Ω , which brings the tip in close proximity to the surface and thus increases the interaction with the molecules. This suggests a high dimer-surface binding energy.

The pair formation is accompanied by the removal of four substrate gold atoms underneath the molecular dimer. Evidence for this adsorbate-induced surface reconstruction is given by STM images reproduced in Fig. 18. In Fig. 18a, an image is shown recorded under special, accidental tip conditions where the dimers appear transparent, disclosing holes in the underlying gold substrate.

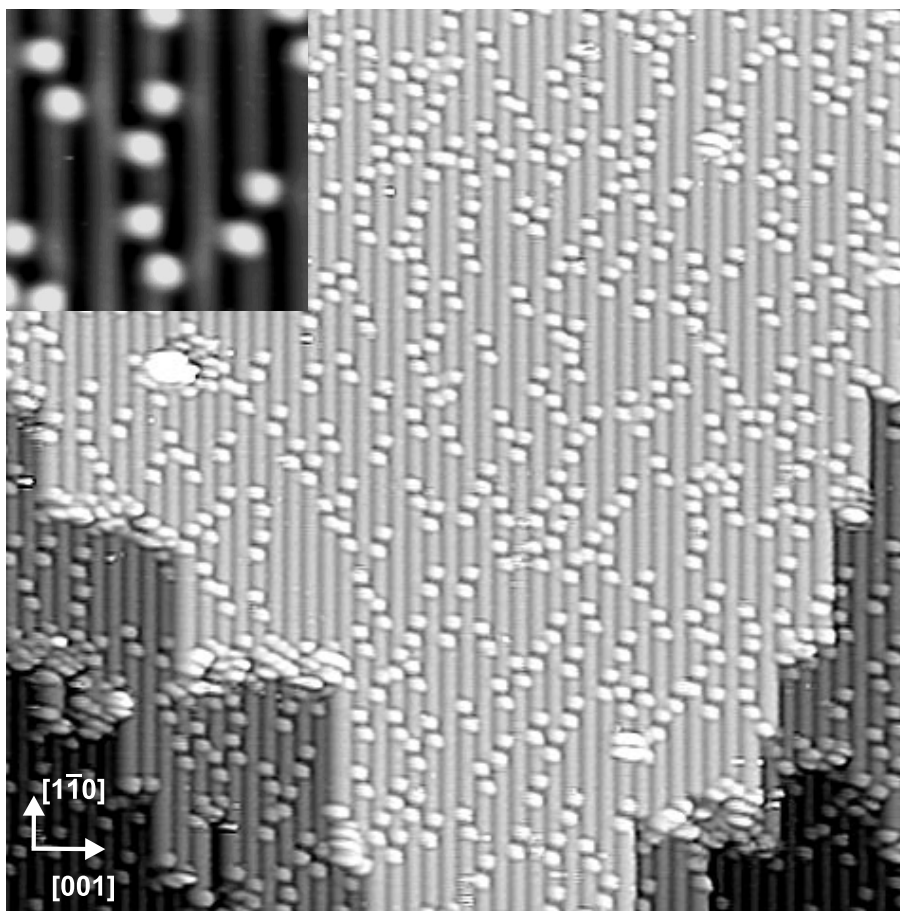


Figure 17: DL cysteine dimers.

Terrace with molecular pairs obtained from the racemic cysteine mixture. The pairs resemble those obtained for the pure enantiomers. Image size: $424 \text{ \AA} \times 459 \text{ \AA}$. Inset: Zoom-in on the structure. Image size: $49 \text{ \AA} \times 53 \text{ \AA}$.

Since these holes lack the 20° rotational signature, it is excluded that the depressions are due to an image inversion effect, which is frequently observed when the tip apex is modified, for instance with an attached molecule [62].

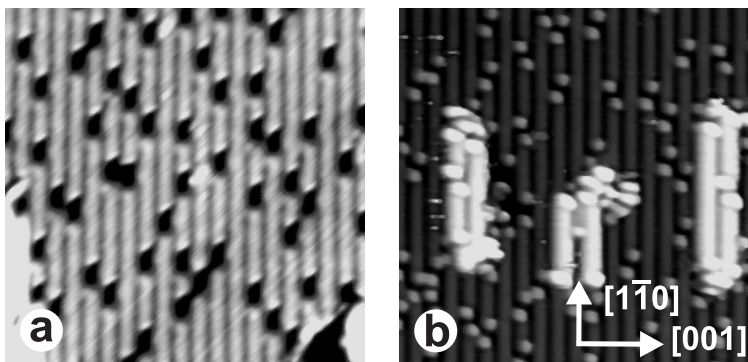


Figure 18: Adsorbate-induced surface reconstruction.

- (a) Terrace imaged with a modified tip, making the cysteine pairs transparent and disclosing holes in the underlying gold substrate. Image size: $163 \text{ \AA} \times 177 \text{ \AA}$.
 (b) The expelled gold atoms nucleate and grow as added gold rows on the terrace. Same size.

The expelled gold atoms nucleate on the surface and form added gold rows on top of large terraces, which is shown in Fig. 18b, giving a typical picture of a large, dimer-covered terrace. On small terraces, no added gold atoms are observed, which can be explained by the expelled gold atoms attaching to the step edges. The activation energy needed to create vacancies in the gold surface explains why annealing is necessary to form the molecular dimers.

4.3.2 DFT calculations

To gain insight into the adsorption geometry at the molecular level and to unravel the atomic-scale origin of the observed chiral recognition, B. HAMMER has performed extended *ab-initio* DFT calculations. The DFT calculations include full structural optimisation, using the non-local density gradient approximation PW91 [71]. First, two molecules interacting in the gas phase were considered in order to determine the most stable configuration for dimer formation in the gas phase [172]. A cysteine dimer formed by one hydrogen bond between the amino group of one cysteine molecule and the carboxylic group of the other has been found to be only slightly more stable ($\sim -0.01 \text{ eV}$) than two individual cysteine molecules, while a dimerisation involving two N–OH hydrogen bonds results in a relative energy gain of -0.40 eV . The formation of pairs via a disulphide bond

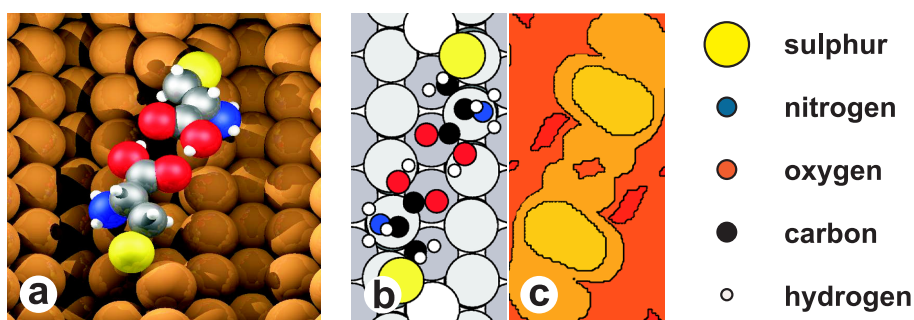


Figure 19: DFT calculation of an LL cysteine dimer.

The most stable configuration of an LL cysteine dimer in a three-dimensional (a) and two-dimensional view (b). The sulphur atoms are moved to a bridge position while simultaneously both amino groups are pointing towards the surface. (c) Simulated STM image showing the surface of constant LDOS. The contours of constant height are separated by 1.0 \AA .

costs $+0.30 \text{ eV}$, due to the energy needed for dehydrogenation and does therefore not exist in the gas phase, although the resulting disulphide, cystine, is a stable molecule. The most stable configuration has been identified as a dimer formed via two hydrogen bonds between the oxygen atoms of the carboxylic groups and is favourable by -0.68 eV relative to the energy of the two individual monomers, as could be expected from the general tendency of carboxylic groups to form strong hydrogen bonds. Therefore, molecular dimers formed by hydrogen bonds between the two carboxylic groups have been considered for the calculation of the pairs bound to the gold surface. In agreement with the room-temperature RAIRS study (see section 4.2.2), and since thiols are known to undergo hydrogen dissociation on gold surfaces and bind to the surface via a strong sulphur–gold interaction [46, 104, 123], the cysteine molecules were anchored to the surface via the dehydrogenated sulphur atoms. The DFT calculations on the surface were performed with 38 independent gold atoms arranged in a slab geometry modelling four layers of the reconstructed gold surface. The upper two layers and all atoms within the two cysteine molecules of the dimer were relaxed until the total residual force was below 0.4 eV \AA^{-1} . Inspired by the experimental findings, a variety of different adsorption geometries was explored for a cysteine dimer on top of a four-atom wide gold vacancy. The most stable configuration is shown in Fig. 19 along with a simulated im-

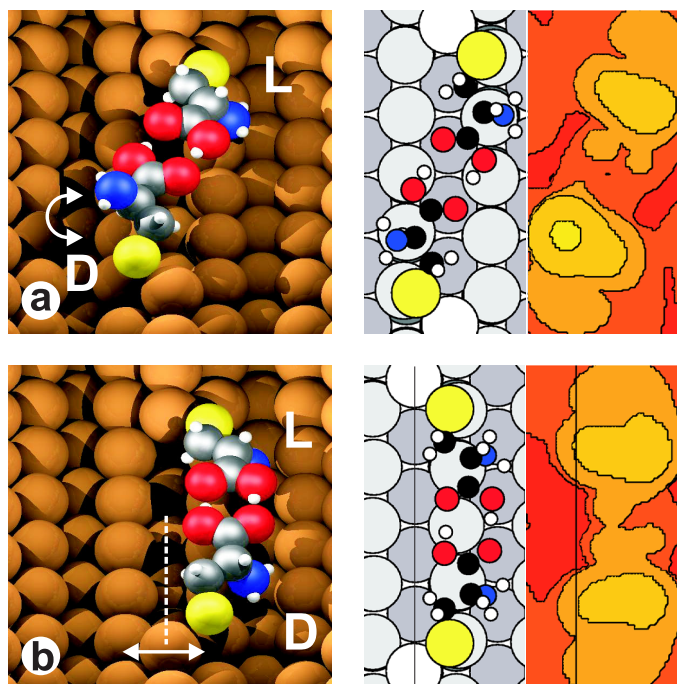


Figure 20: DFT calculation of DL cysteine dimers.

- (a) The first strategy to obtain a DL dimer is to exchange the amino group with the hydrogen atom at the asymmetric carbon atom on one cysteine molecule.
- (b) Another strategy for a DL dimer formation is to mirror one molecule within the LL dimer.

age, showing the surface of constant local density of states. Bright lobes are positioned over the cysteine molecules, and the main axis of this double-lobe feature exhibits a 20° clockwise rotation in accordance with the experimental results. As L and D cysteine molecules are mirror images of each other, a DD dimer is consequently obtained by mirroring Fig. 19. The DD dimer has the same stability, but exhibits the 20° counter-clockwise signature of the experimentally observed DD dimers.

The clockwise rotation of the LL dimer originates from the fact that the optimum adsorption position for the sulphur atom within the cysteine molecule

is a bridge site (see section 3.3.2), while it is energetically favourable for the amino group to interact with the gold surface via its lone pair. The simultaneous fulfillment of these two constraints leads to the 20° rotation of the pair in a direction, exclusively determined by the position of the amino group, i.e., the chirality of the molecule. Additionally, the preference of sulphur to bind to reactive, low-coordinated sites constitutes the driving force for the vacancy formation. As the interaction of the carboxylic groups with the gold surface has been found to be energetically unfavourable [173], the formation of a vacancy structure underneath a cysteine pair may also be favoured by increasing the carboxyl–gold distance.

Having established a reasonable model for the adsorption geometry of the cysteine dimers, the origin of the observed chiral recognition, that is, the absence of heterochiral dimers, can be discussed. Possible DL dimer configurations can be formed by exchanging one L cysteine molecule in the dimer shown in Fig. 19 with a D cysteine molecule. The simplest way to achieve such a DL dimer is shown in Fig. 20a, where the amino group and the hydrogen atom are exchanged on the asymmetric carbon atom. While preserving the strong sulphur–gold and carboxylic–carboxylic bonds, this strategy leads to the loss of one of the amino–gold bonds. This dimer is consequently less favourable than the homochiral pair by about +0.2 eV, which is of the order of the amino–gold interaction energy [173]. Another way to form a DL dimer is to mirror one molecule within the LL dimer, as shown in Fig. 20b. This results in a mismatch in the strong carboxylic–carboxylic interaction, which is compensated by relaxation at the expense of increasing the amino–gold distances from 2.4 to 2.7 Å. This is associated with an energy cost of +0.5 eV, which is about twice the amino–gold interaction energy. In addition to the higher formation energies, the simulated STM images of the DL dimers shown in Fig. 20 do not agree with the observed data, as they do not show the experimentally observed C_2 symmetry, ruling out the possibility that the images in fact show DL pairs with the same rotation signature as homochiral cysteine pairs. Another argument for why no DL pairs exist, having accidentally the same appearance as homochiral pairs, goes as follows: Assume it would be possible to exchange at an energy cost of E_{DL} one molecule within an LL pair by a D cysteine molecule, while preserving the appearance of the molecular dimer. It is reasonable to assume that the additional energy cost for exchanging the *second* molecule within the pair is of the same order (i.e. $2E_{DL}$ in total). It is furthermore assumed that this would still not change the rotational signature of the pair.

If the temperature is sufficiently high to allow for the existence of DL pairs with LL signature, that is $k_B T \approx E_{DL}$, then the probability for an object associated with an energy of $2E_{DL}$ is of the order of some percent (13%). Thus, at least

a few counter-clockwise rotated dimers should exist on the surface in the case of pure L cysteine. Counter-clockwise rotated dimers (and clockwise for D cysteine) have, however, never been observed among the more than 1000 observed cysteine dimers.

An overview of the energetics involved in the cysteine adsorption is given in Fig. 21. The adsorption of two individual cysteine molecules onto a Au(110)-(1×2) with a four-atom wide vacancy structure is associated with an energy gain of -1.9 eV, excluding the energy cost of +0.43 eV needed for creating the vacancy structure (PW91). This energy can be compared with the formation energies of the separated steps of the adsorption process. As an estimate for the cysteine dehydrogenation and sulphur-gold bond formation, DFT results that have been obtained previously for methylthiol [121] are listed in Fig. 21. The energy gain associated with the adsorption of ammoniac [173] can be considered as a value for the adsorption energy of the amino group. The sum over these separate adsorption steps amounts to -1.5 eV, which corresponds well to the energy of -1.9 eV obtained here, demonstrating that the adsorption process can be well understood by considering the formation of the local bonds separately [173].

In summary, the DFT calculations reveal that the origin of the observed chiral recognition can be explained in terms of the three bonds formed on each molecule: The carboxylic-carboxylic hydrogen bond, the sulphur-gold, and the amino-gold interaction (note that the first bonding mentioned is inter-molecular, while the other two are between the cysteine molecule and the gold surface). The simultaneous optimisation of these three bonds is only possible for homochiral dimers, as the geometry of heterochiral dimers inevitably results in the breaking of one of these bonds.

With these three bonds involved, the cysteine dimers constitute a direct illustration of the well-known three-point contact model for chiral recognition introduced by L. H. EASSON and E. STEDMAN in 1933 [55, 56]. This model gives a geometric explanation of the fact that at least three contact points have to be involved for chiral recognition to occur, and that two enantiomeric forms can be differentiated by the successful or unsuccessful docking to an adsorption site with at least three contact points, as illustrated in Fig. 22. By directly pinpointing the three bonds involved in the chiral recognition process observed for the cysteine pairs, a molecular-level demonstration of this generic, conceptual model is given.

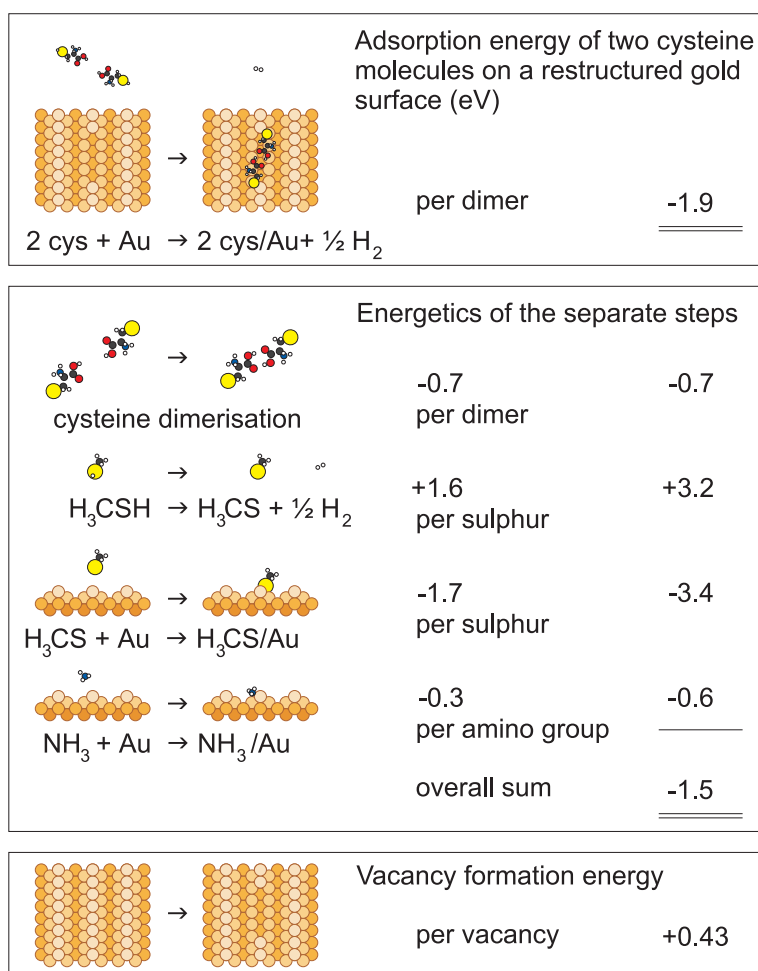


Figure 21: Summary of the DFT results.

Adsorption of two cysteine molecules on a vacancy-structured Au(110)-(1×2) surface is associated with an energy gain of -1.9 eV (PW91). This energy can be compared with the energetics of the separate steps involved in the adsorption process (the energies given are taken from [171], [121] and [173]), which amount to -1.5 eV. An energy cost of +0.43 eV for creating the vacancy structure must be added to these energies.

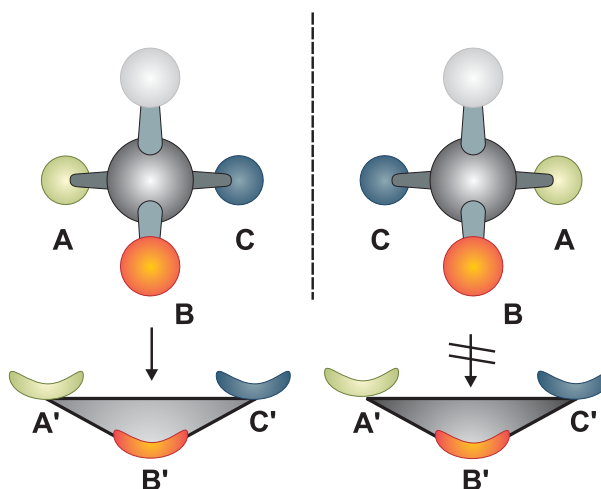


Figure 22: Sketch of the three-point contact model.

Two enantiomers can be differentiated by the successful or unsuccessful docking to an adsorption site with at least three contact points.

4.3.3 Cysteine pairs at kink sites

The model obtained for the adsorption geometry of the cysteine pairs discussed in the previous section can now be employed to understand the cysteine pair adsorption at special adsorption sites such as kink sites. As discussed in section 3.1, kink sites constitute chiral centres at the surface. In the following, the appearance of the cysteine dimers at kink sites is presented and discussed in terms of the optimum adsorption sites previously identified.

The characteristic appearance of a D cysteine pair adsorbed at an *S* kink site is shown in Fig. 23a. This pair resembles the pairs adsorbed on the terraces in shape and size; however, it is only rotated about 10° with respect to the close-packed gold rows compared to a 20° rotation observed for pairs adsorbed on terraces. This difference in appearance can be understood when considering the local adsorption geometry of the cysteine pair. A possible model that explains the observed rotation by about 10° is given in Fig. 23b. As discussed in the previous section, the sulphur atoms of the pairs on the terrace bind to the low-coordinated gold atoms that terminate the four-atom wide gold vacancy structure underneath the pairs. Exactly the same binding configuration

is found at the terminating gold atom at a kink site, and it seems reasonable to assume that a kink site constitutes a well-suited adsorption site for one sulphur atom within a cysteine pair. This binding site has the advantage that no energy is needed for restructuring the surface underneath the pair as otherwise observed on the terraces, since the local geometry of the step edge already resembles the vacancy structure on the surface. The binding of the second sulphur atom in the pair constitutes a change compared to the situation on the terrace: On the terrace, this sulphur atom binds to a gold atom in the topmost gold row. In order to achieve the same adsorption site on the lower terrace, the D cysteine pair has to rotate clockwise, as the topmost gold row of the lower terrace is shifted by half a unit cell dimension in the $[001]$ direction with respect to the topmost gold row of the upper terrace. Thereby the overall counter-clockwise rotation of this D cysteine pair is less than what is observed

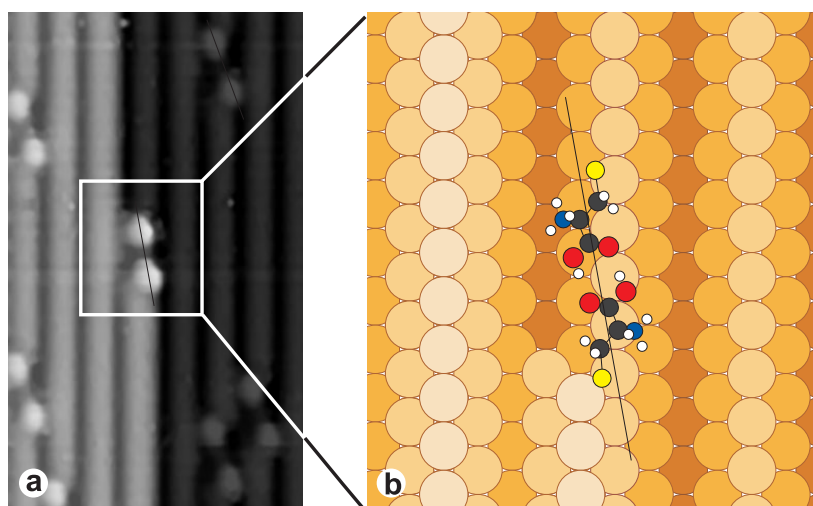


Figure 23: D cysteine pairs on the terrace and at an S kink site.

The rotation of a cysteine pair adsorbed at a step edge is only about 10° with respect to the close-packed direction compared to the 20° rotation observed for pairs adsorbed on terraces.

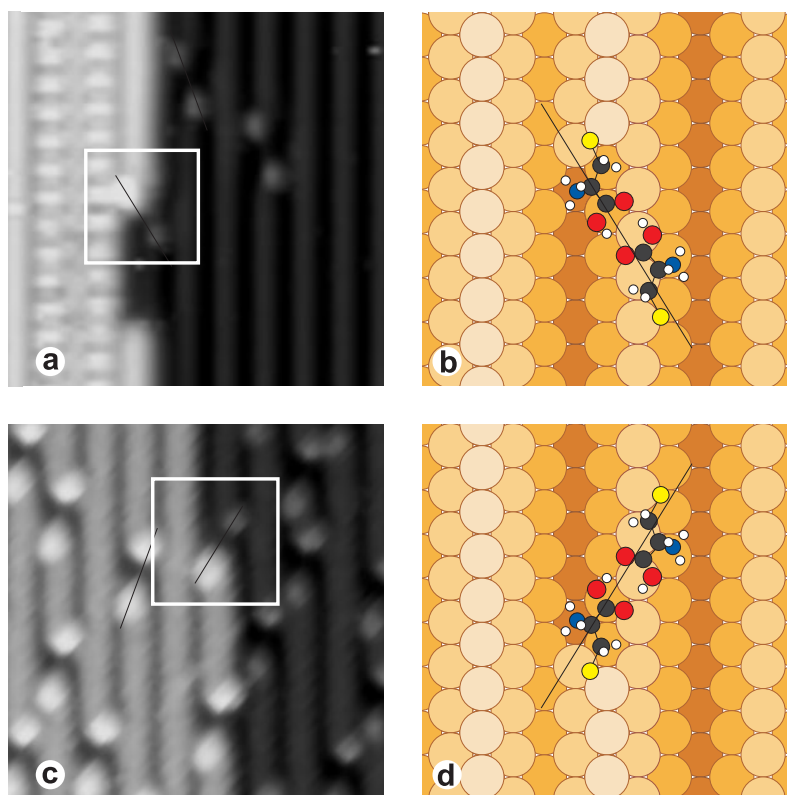


Figure 24: D cysteine pair adsorbed at an R kink site and L cysteine pair adsorbed at an S kink site.

(a) At an R kink site, the D cysteine pair has to be rotated additionally counter-clockwise in order to match the optimum adsorption positions for the sulphur atoms (see model in (b)). To the left, a chain-like cysteine structure is seen that is discussed in section 4.4. (c) The similar, but mirror-imaged situation is found for an L cysteine pair adsorbed at an S kink site.

on the terraces.

The opposite effect is observed at a mirror-image kink site: Figure 24a dis-

plays a D cysteine pair adsorbed at an *R* kink site. As illustrated in the image, this cysteine pair is rotated about 30° counter-clockwise with respect to the close-packed gold rows. Again, the binding of the sulphur atom to the upper terrace is identical to the situation on the terrace. In the case of an *R* kink site, the pair has to rotate slightly counter-clockwise in order to match the optimum adsorption position on the lower terrace, leading to an increase in the net counter-clockwise rotation of this D cysteine pair.

Since the adsorption of L cysteine yields the same, but mirror-imaged situation, the adsorption of L cysteine pairs at an *S* kink site results in the opposite, 30° clockwise rotation as is demonstrated in Figs. 24c and d.

4.4 Self-assembly of molecular chains

4.4.1 STM results

Coexisting with the molecular dimers, another molecular structure is observed upon submonolayer deposition, depicted to the right in Fig. 25a. As shown in the high-resolution STM image in Fig. 25b, bean-shaped entities stack along the $[\bar{1}\bar{1}0]$ direction, forming rows. These rows always pair together to form the double-row structures shown. The characteristic rows of bean-shaped structures within a double row are separated by about ~ 10 Å in the $[001]$ direction, as evident from the height profile in Fig. 25c. The individual features within a row have a top-to-top distance of 5.8 Å along the $[\bar{1}\bar{1}0]$ direction. These dimensions strongly suggest that each double row consists of two rows of cysteine molecules aligned along the $[\bar{1}\bar{1}0]$ direction. Compared to the topmost gold atoms, the cysteine rows protrude by only 0.16 Å (see height profile in Fig. 25c). This small protrusion suggests that the cysteine molecules are not adsorbed on top of underlying added gold rows of the (1×2) reconstruction, but

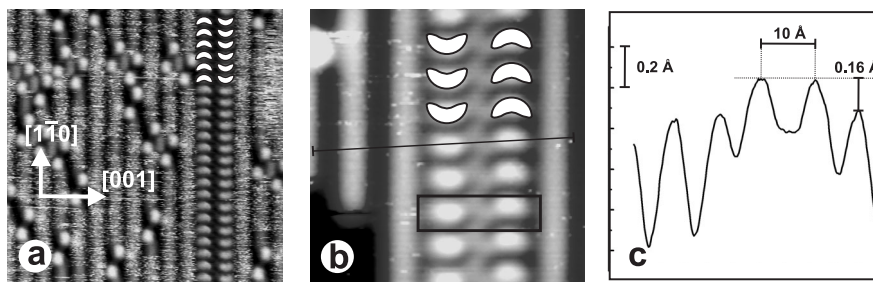


Figure 25: Cysteine double-row structure.

(a) L cysteine structures after annealing the sample to 380 K. Apart from molecular dimers, extended molecular double rows are observed, aligned along the $[\bar{1}\bar{1}0]$ direction. The molecules within the double-row structure possess a bean-like shape, as indicated by the white symbols in the figure. Image size: $120 \text{ Å} \times 120 \text{ Å}$. (b) Zoom-in on a double row formed from D cysteine molecules. In this case, the shape of the molecules within the rows is mirror-imaged compared to the situation for L cysteine. The (2×5) unit cell of this structure is given in this image. Image size: $40 \text{ Å} \times 40 \text{ Å}$. (c) Height profile over a double-row structure. The position of the height profile is indicated by the white line in (b).

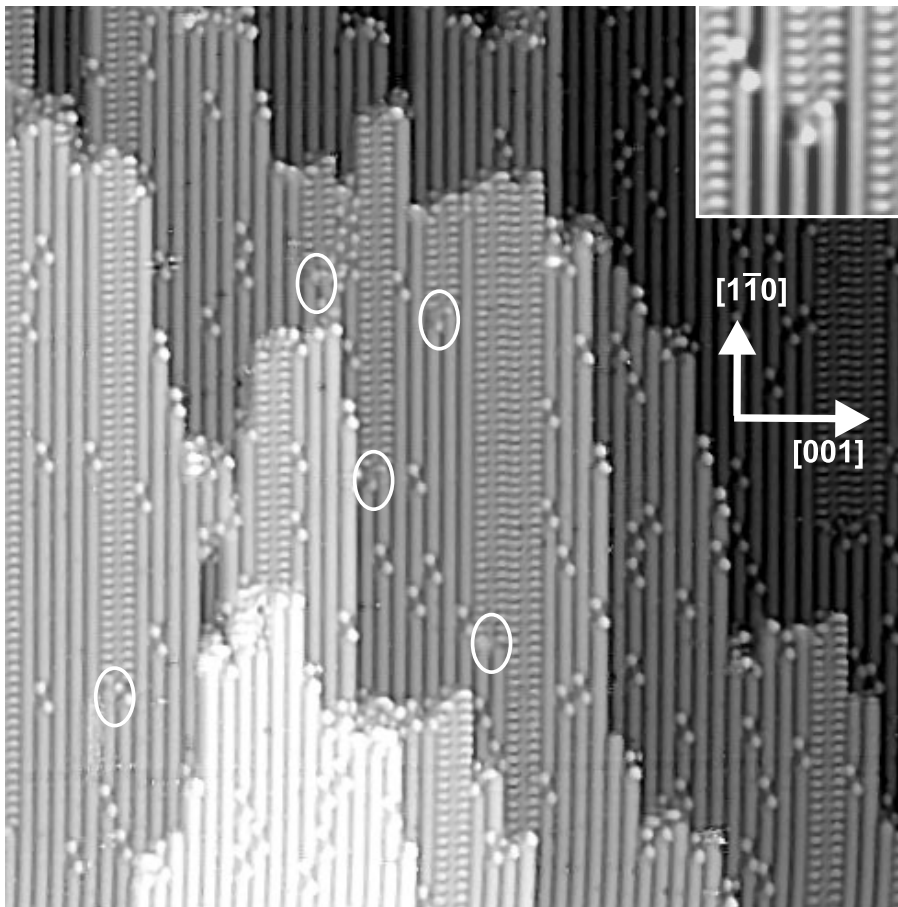


Figure 26: Large-scale STM image of molecular chains of cysteine on Au(110).

(a) Large-scale STM image showing the coexisting molecular structures of D cysteine on a gold (110)-(1×2) surface. The molecular double-row structure is terminated at descending step edges or at defects on the terraces as marked. Image size: 425 Å×425 Å. Inset: Typical termination of a double row on the terrace. Image size: 57 Å×57 Å.

rather that the formation of the molecular double rows is accompanied by the

removal of gold atoms underneath the cysteine structure. By comparison, the individual cysteine dimers discussed in the previous section protrude by 0.6 Å, although they also form over vacancies in the gold rows. The bean-like shape of the molecular features within the double-row structure breaks the mirror symmetry of the double rows, reflecting the chirality of the cysteine molecules, as indicated by the exaggerated white symbols in Fig. 25a. Evaporation of the other enantiomer, D cysteine, indeed results in a similar, but mirror-imaged structure, as demonstrated in Fig. 25b.

On large terraces, the cysteine double rows extend over several hundreds of Ångströms and terminate at step edges, as demonstrated in Fig. 26. The nucleation of the double-row structures appears to take place at step edges as shown by the following argument. By analysing a total of 138 double rows that are imaged in their entirety (i.e., where both ends are observed within one STM image), 69 (50%) were found with both ends at step edges, 67 (49%) with one end at a terrace and the other at a *descending* step edge (five of such rows are marked in the overview in Fig. 26), while only two (1%) were found with one end at a terrace and the other at an *ascending* step edge. No rows were observed with both terminations at a terrace. If the double rows nucleated on the terraces, the number of rows ending at descending and ascending step edges should be equal for symmetry reasons, and one would also expect to see rows with both ends on a terrace. It is therefore concluded that the descending step edges constitute the nucleation site of the double rows which grow until they reach an ascending step edge or are otherwise terminated. It is noteworthy that the terminations at the terraces are typically associated with a specific double-lobe structure that is shown in the inset in Fig. 26.

4.4.2 DFT calculations

To complement the experimental findings, DFT calculations have been performed by L. MOLINA and B. HAMMER. The calculations were carried out using the DACAPO code with a plane wave basis set, ultrasoft pseudopotentials and the PW91 XC functional [71]. The gold surface has been modelled using a slab geometry of 3 layers plus added gold atoms or gold rows of which all apart from the two bottom layers are relaxed. Calculations with 5 gold layers confirmed that the obtained adsorption energies for 3 layers are converged to the 0.1 eV/cysteine level.¹⁰

¹⁰As the energy obtained by DFT depends on the level of relaxation and the number of gold layers considered, the formation energies given in this section differ slightly from corresponding energies stated in the previous section. The periodicity of the double-row structure along the $[1\bar{1}0]$ direction facilitates the DFT calculations compared to the case of the individual cysteine dimers, making more precise calculations possible. In order to

The aim of conducting the DFT calculations has been twofold, namely to provide a structural model of the double rows and to disclose the driving force for the uni-directional growth of these structures. The calculations include not only the added-row reconstructed Au(110)-(1×2) surface, but also the unreconstructed Au(110)-(1×1) surface. Additionally, some gold surfaces with gold atoms added in patterns that are compatible with the observed STM images have been considered, which may originate from trapping of expelled surface atoms between the molecules. These restructured surfaces lead, however, to energetically unfavourable structures, and in the following only the structures on the unperturbed (1 × 2) surface and the (1 × 1) surface with lifted reconstruction are presented.

The gold surfaces are realised in (2 × 5) unit cells (5.77 by 20.40 Å) and are illustrated in Figs. 27a and b. The energy cost for lifting the surface reconstruction of +0.4 eV per unit cell is compensated by an increased adsorption strength of the cysteine molecules on this modified surface.

Guided by the STM images and the knowledge of how alkanethiols adsorb on gold [46, 121, 122, 174, 175], the cysteine molecules have been anchored at the gold surface via the dehydrogenated sulphur atoms, a bond known to be energetically favourable by -1.7 eV [176]. Two dehydrogenated cysteine molecules per unit cell have been considered, allowing for full relaxation starting from a number of different initial configurations. The most favorable structures determined by the calculations are shown in Figs. 27c-f, along with indications of the adsorption energies.

The energetically most stable double-row structure is found on a gold surface where the added-row reconstruction has been lifted. This double-row structure, shown in Fig. 27c and superimposed onto an STM image in Fig. 28, involves a dimerisation of the cysteine molecules with hydrogen bonds along the [001] direction, while no direct inter-dimer bonding is found in the [1 $\bar{1}$ 0] direction. The cysteine molecules are further anchored to the surface by bonds between the lone pair on the amino groups and surface gold atoms. The binding energy is calculated to be -2.50 eV per dimer which reduces to -2.10 eV, when the +0.40 eV cost of lifting the surface reconstruction is included.

Motivated by the appearance of the double rows in the STM images and to investigate the influence from changing the molecule adsorption geometry, other configurations were explored, as given in Figs. 27d-f. These structures, however, were less stable and suffer from mismatches in the bonding of various kinds, as discussed in the following. In Fig. 27d, a configuration with the sulphur positions on the right shifted by one lattice distance is shown, leading

maintain consistency, only energies with the same level of relaxation and the same number of modelled gold layers may be compared.

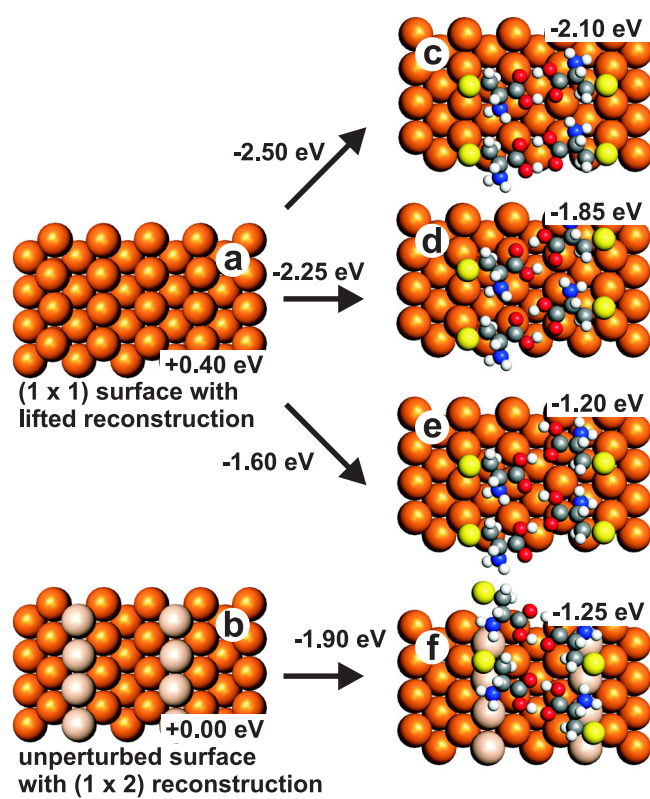


Figure 27: Ball models of the most stable D cysteine double-row structures.

- (a) Au(110) surface where the missing-row reconstruction has been lifted.
 (b) Unperturbed Au(110)-(1 × 2) surface. (c) Unit cell of the most stable D cysteine double-row structure, where each cysteine molecule forms two hydrogen bonds via the carboxylic group to the neighbouring cysteine molecule.
 (d) Same structure as in (c), but here the sulphur atoms to the right have been shifted by one lattice distance along the $[1\bar{1}0]$ direction. (e) Cysteine double-row structure where each molecule forms hydrogen bonds via the carboxylic group with two neighbouring cysteine molecules in the adjacent row, leading to a “zig-zag” structure. (f) Structure placed on an unperturbed (1 × 2) missing-row reconstructed gold surface.

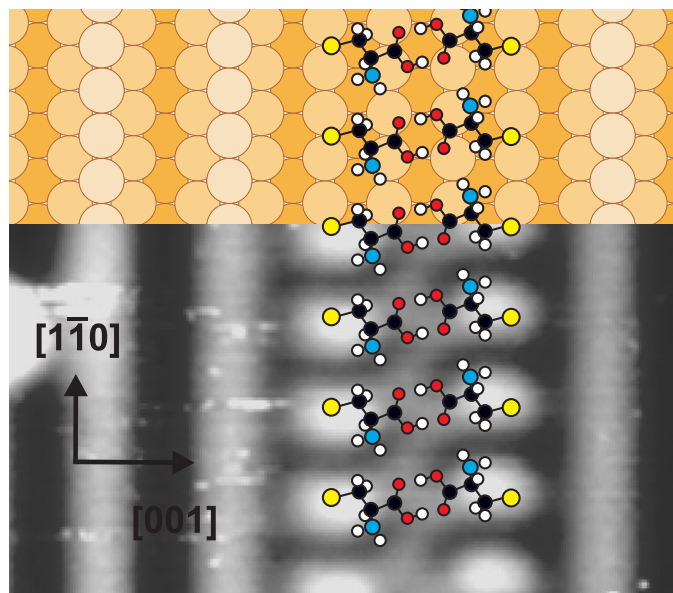


Figure 28: Most stable D cysteine double-row structure.

Most stable D cysteine double-row structure as obtained from the DFT calculations superimposed onto an STM image.

to a stretching of the O–HO bonds from 1.6 to 1.7 Å. In this context, the dependence of the hydrogen-bond energy on the bond length has been analysed, revealing the most stable binding with an energy gain of about -0.85 eV for an O–HO distance of 1.52 Å. Increasing the distance results in a drastic loss in binding energy, as illustrated in Fig. 29. In Fig. 27e, a situation is shown where the cysteine molecules are interconnected along the $[1\bar{1}0]$ direction. This is appealing since such an interconnection would provide a clear rationale for the uni-directional growth. In this structure, however, the gold–nitrogen bonds are stretched from 2.4 to 2.9 Å, reducing the energy gain associated with the nitrogen–gold bonds. Finally, in Fig. 27f an unchanged Au(110)-(1×2) surface is considered. For an unchanged Au(110)-(1×2) surface, however, the bonding is diminished by the coordination of one surface gold atom to both the sulphur

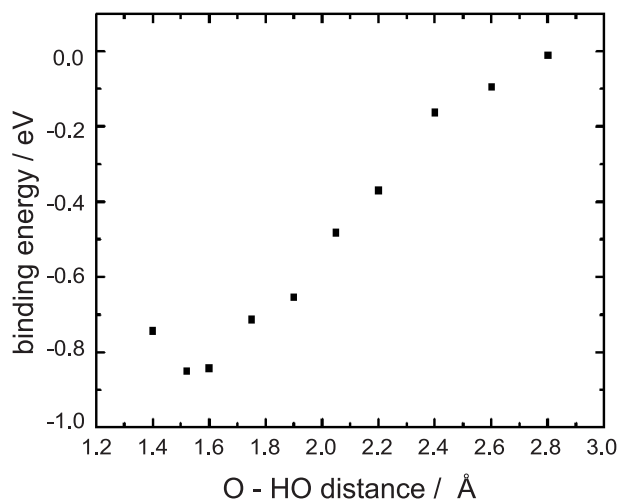


Figure 29: Dependence of the binding energy of hydrogen bonds on the O–HO distance.

The most stable hydrogen bonding is achieved for an O–HO distance of around 1.52 Å with an energy gain of about -0.85 eV.

and the nitrogen atom on one cysteine molecule, which is less stable than the situation in Figs. 27c–e, where different gold atoms are involved in the bonds to the sulphur and the nitrogen atom.

It is interesting to note that the structure in Fig. 27e, in which the cysteine molecules interact with two cysteine molecules in the neighbouring row, is the least stable structure compared to the two other double-row structures on the unreconstructed gold surface. Other structures (not shown) with hydrogen bonds between the cysteine molecules in the direction of the double row, did not lead to more stable structures either. These include the situation of hydrogen bonds formed between the carboxylic and amino groups as a precursor of a peptide bond formation. The DFT calculations presented so far do, therefore, not provide an explanation for the growth of extended double rows along the $[1\bar{1}0]$ direction, since no direct inter-dimer interaction is identified. This points to an interaction of a more indirect nature, suggesting that the formation of the structural rearrangement within the gold surface is responsible for the row formation.

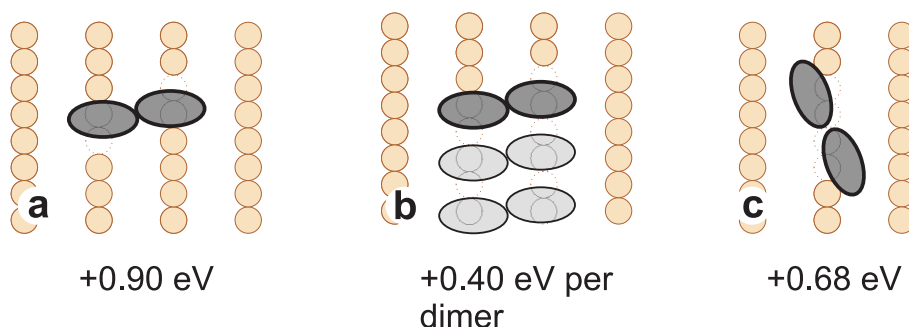


Figure 30: Growth mechanism of the cysteine chains.

The energy cost for initiating a double row on the terrace is +0.90 eV, while the energy needed to create the four-atom wide vacancy is +0.68 eV.

In Fig. 30, a scheme is presented of how a double row may nucleate. For a double row to *form* on a terrace, a single cysteine dimer must first carve out four gold atoms from the reconstructed gold surface, as illustrated in Fig. 30a. According to the DFT calculations, this costs +0.90 eV, since four kink sites are created in the added gold rows (removing the first and second gold atom in each row costs +0.31 and +0.14 eV, respectively). For a double row to *grow* (Fig. 30b), however, the additional cost of lifting the gold reconstruction is only +0.40 eV per segment, as no new kink sites have to be created.

Figure 30 thus indicates that two cysteine molecules must overcome a much larger barrier for creating a nucleation site for a new double row (+0.90 eV) than for continuing the growth of an existing double row (+0.40 eV). The energetics of the surface restructuring thereby readily explains the experimental observation of the extended double rows, rather than many short double rows. In fact, it is found in the experiment that the only active nucleation site is the descending step edge. This is easily understood using the present picture – at the descending step edge the gold kink sites already exist, reducing the cost of creating the nucleation site for the double-row structure.

For completeness, Fig. 30c also shows the formation energy of the vacancy structure underneath the isolated dimers, obtained within the same level of relaxation as the other DFT results presented in this section. The formation energy of +0.68 eV (removing the first to fourth gold atom in the row costs +0.31, +0.14, +0.12 and +0.11 eV, respectively) is consistent with the upper bound of +0.9 eV given by the inactive processes of Fig. 30a.

In conclusion, the presented STM measurements and DFT calculations demonstrate how adsorbate-induced surface restructuring during molecular adsorption can provide a driving force for the uni-directional growth of molecular structures even when direct adsorbate-adsorbate bonding along the growth direction is lacking.

4.5 Cysteine adsorption at higher coverages

4.5.1 Extended surface restructuring

When the cysteine coverage is increased to a few percent of a monolayer, a substantial amount of molecular pairs are present at the surface after annealing at 380 K. A closer inspection of the molecular dimers discloses that they tend to align both “sideways” along the (2,-2) direction¹¹ and “head-to-tail” along the (5,2) direction, as shown in Fig. 31a. The position of some selected cysteine pairs from Fig. 31a are reproduced in Fig. 31b, demonstrating the preferential ordering of the pairs along the (2,-2) direction, as seen on the right-hand side, and along the (5,2) direction, as seen to the left in the image. As reported in section 4.3, the formation of the cysteine dimers involves a surface reconstruction with four gold atoms removed from the close-packed row underneath the dimer. For isolated cysteine dimers it has been observed that these gold atoms nucleate and grow as added gold rows on top of large gold terraces (Fig. 18b). When the dimers are aligned sideways along the (2,-2) direction, however, additional features are found in the troughs between the cysteine pairs that are interpreted as additional gold atoms. This is demonstrated in Fig. 31a, where an arrow points at one trough with additional gold atoms, and the position of the added gold atoms in the troughs is reproduced with grey circles in Fig. 31b. The added gold rows in the troughs are four gold atoms wide, suggesting that the expelled gold atoms from the vacancies underneath the pairs are trapped in the neighbouring atomic trough, when the molecular pairs align along the (2,-2) direction.

When the molecular pairs arrange both along the (2,-2) and (5,2) directions at the same time, they form an ordered molecular array on a highly restructured surface with a (7×2) unit cell. Such an area is shown in the lower right corner in Fig. 31c, and the positions of the cysteine dimers are reproduced in Fig. 31d.

4.5.2 EMT calculations

In order to determine the driving force behind the observed restructuring of the gold surface, EMT calculations (see section 2.6.2) have been performed. Compared to the *ab initio* DFT calculations presented in the previous sections, EMT provides an approximative approach which does not have the same high accuracy. The following EMT calculations do, however, offer the general trends in formation energies that are useful when analysing the possible ori-

¹¹Conventionally, the first integer refers to the $[\bar{1}10]$ direction and is given in units of the lattice vector $d_1 = 2.88 \text{ \AA}$, while the second integer refers to the $[001]$ direction in units of $d_2 = 4.08 \text{ \AA}$.

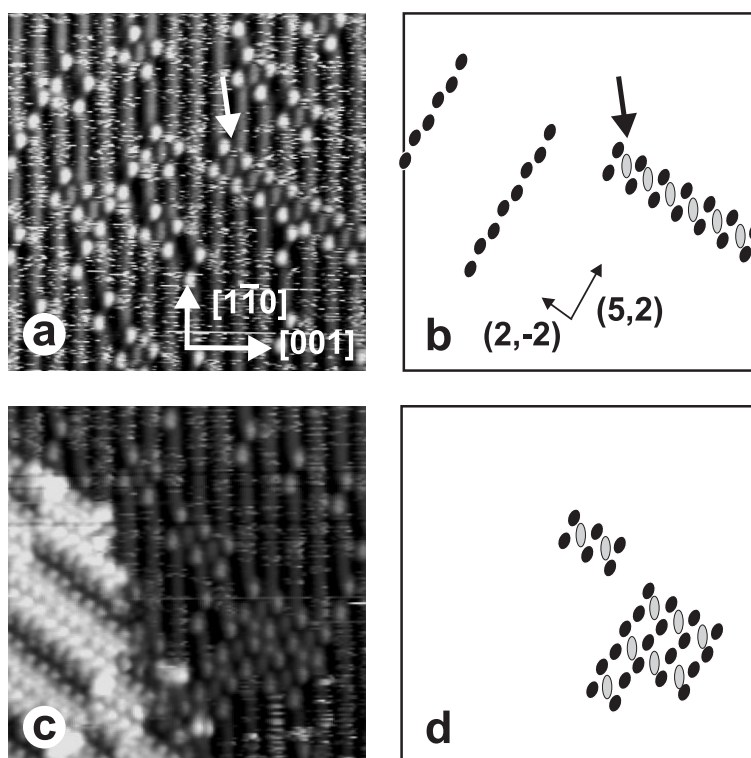


Figure 31: Alignment of L cysteine pairs.

(a) Terrace with cysteine pairs. The molecular pairs tend to align both along the (2,-2) and the (5,2) direction. The black spots in (b) represent the positions of selected cysteine pairs. Grey circles show areas with added gold atoms in the atomic troughs. Image size: $122 \text{ \AA} \times 122 \text{ \AA}$. (c) Terrace showing an area with assembled cysteine pairs. The cysteine positions are marked in panel (d). To the left, a more dense cysteine structure, discussed below, is visible. Same image size.

gin of the observed surface restructuring. The overall formation energy for a four-atom wide vacancy and an added gold row in the neighbouring atomic trough is obtained within the EMT formalism by evaluating the change in the number of nearest neighbours of the gold atoms [76,78]. A model of the surface

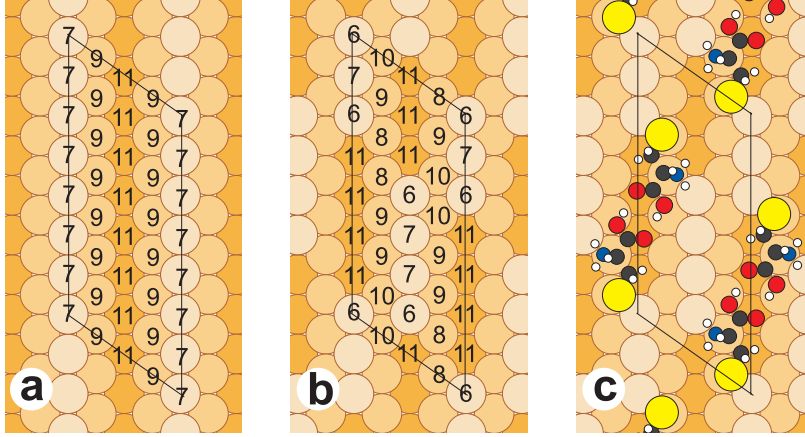


Figure 32: Unit cell of the surface restructuring.

Unit cell of the array structure superimposed onto an unmodified (a) and a restructured (b) Au(110)-(1 × 2) surface, showing the change in the number of nearest neighbours for each surface atom. (c) Model with the cysteine pairs superimposed.

reconstruction, showing the changes in coordination of the surface gold atoms, is given in Fig. 32. With the appropriate energies for gold, the energy cost per unit cell of the present reconstruction amounts to

$$\Delta E = 8E(9) + 4E(7) - 4E(10) - 4E(8) - 4E(6) = +0.72 \text{ eV}. \quad (20)$$

In order to estimate the accuracy of this approach, the formation energies for several periodic vacancy structures in a close-packed row obtained by EMT have been compared to those revealed from DFT calculations. For a four-atomic vacancy structure as shown in Fig. 33a, the energy cost is calculated by EMT to +0.56 eV per unit cell compared to +0.53 eV obtained from DFT (RPBE), respectively +0.43 eV (PW91). Additionally, three other periodic structures are depicted in Fig. 33, and the formation energies calculated by EMT and DFT are given. In general, the results from EMT become unreliable

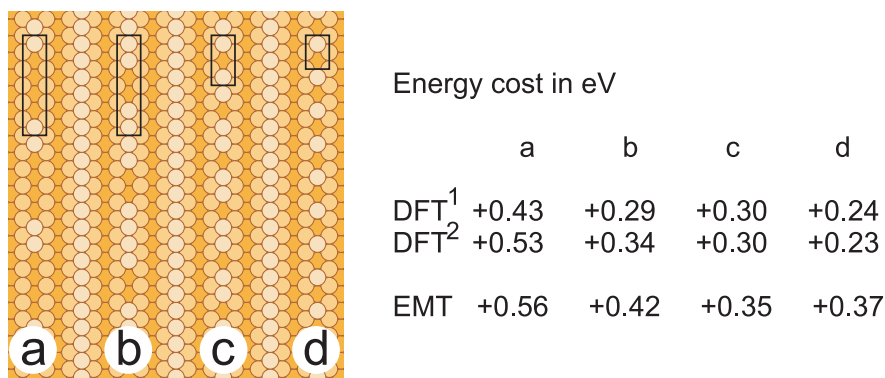


Figure 33: Vacancy structure formation energy calculated by DFT and EMT.

Difference in the formation energy for several periodic vacancy structures calculated by DFT (¹ PW91 and ² RPBE) and EMT. The unit cells are marked by rectangles. (a) Periodic four-atom vacancy structure. (b) Two-atom vacancy structure separated by four atoms. (c) Monatomic vacancy separated by two gold atoms and (d) monatomic vacancy separated by only one gold atom.

when applied to monatomic vacancies. On the other hand, however, the results agree fairly well with the DFT calculations when applied to vacancy islands with four gold atoms. From this consideration, it can be concluded that the formation energy of +0.72 eV per unit cell obtained by EMT to create the observed surface restructuring represents a reasonable estimate.

To understand why the pairs align, the formation energy of +0.72 eV must be compared with the formation energy of the four-atom wide vacancy structure underneath individual, unaligned cysteine pairs, where the expelled atoms are added to step edges. As listed in Fig. 33a, this structure is associated with an energy cost of +0.56 eV, when calculated within the EMT formalism. Compared to the formation of such individual vacancies, the present structure requires more energy due to the low-coordinated gold atoms at the ends of the four-atom wide structure in the atomic troughs. The energy difference of 0.16 eV per molecular dimer must be compensated by the modified adsorption configuration of the molecular dimers on the restructured surface. Interestingly, the added gold rows in the neighbouring troughs are terminated at the

amino groups (see Fig. 32c), allowing for a closer proximity of both amino groups within a pair to the gold surface. As it has been shown to be energetically favourable for the amino group to be in close proximity of the gold surface in order to form a bond via the lone-pair (section 4.3), this reduction in the nitrogen–gold distance may be the driving force for the alignment along the (2,-2) direction and the formation of the short, otherwise energetically unfavourable gold rows with low-coordinated atoms at the terminations. From the EMT estimation, an energy gain of about $-\frac{1}{2} \cdot 0.16 = -0.08$ eV per amino group due to the closer proximity of the amino group towards the gold would be sufficient to activate the observed surface restructuring, as every unit cell contains two amino groups.

The driving force for the alignment along the (5,2) direction is more difficult to envision. A possible explanation could be the close proximity between the sulphur atoms, which are separated by about 5 Å in this aligned structure. This distance is comparable to that found in alkanethiol films on Au(111), where it has been reported that the formation of a $c(4 \times 2)$ superstructure on top of the well-known $(\sqrt{3} \times \sqrt{3})R30^\circ$ structure may be due to a slight movement of the sulphur headgroups to reduce the sulphur–sulphur distance to 4.16 Å [46].

4.5.3 Dense cysteine domains

Upon increasing exposure from coverages of a few percent to coverages close to one monolayer and subsequent annealing at 380 K, islands of a dense cysteine overlayer appear, coexisting with the molecular pairs and double chains, covering the remaining terraces. These islands are often found growing from kinked step edges with predominantly one type of kink sites involved, as demonstrated for L cysteine in Fig. 34a, where a kinked step edge is seen in the STM image. The dense cysteine phase grows from the *R* kink sites of this step edge, marked by arrows and illustrated in the inset in Fig. 34a. In the case of D cysteine, the dense phase seems to grow predominantly from the opposite, *S* kink sites, as shown in Fig. 34b. It is important to note that this dense phase is not observed when the racemic mixture is adsorbed.

A zoom-in on a dense layer formed from L cysteine is shown in Fig. 35a, disclosing bright and dark areas formed by features with a top-to-top distance of about 5 Å. The brighter areas protrude by 0.7 Å compared to the darker areas. The molecular structure has a high-symmetry direction, rotated 55° counter-clockwise with respect to the $[\bar{1}\bar{1}0]$ direction, as marked by the black line in Fig. 35a. Domains with the opposite, clockwise rotation are not found for L cysteine. When performing the experiment with D cysteine, however, the same dense phase is formed, but now with a clockwise rotation, as shown in

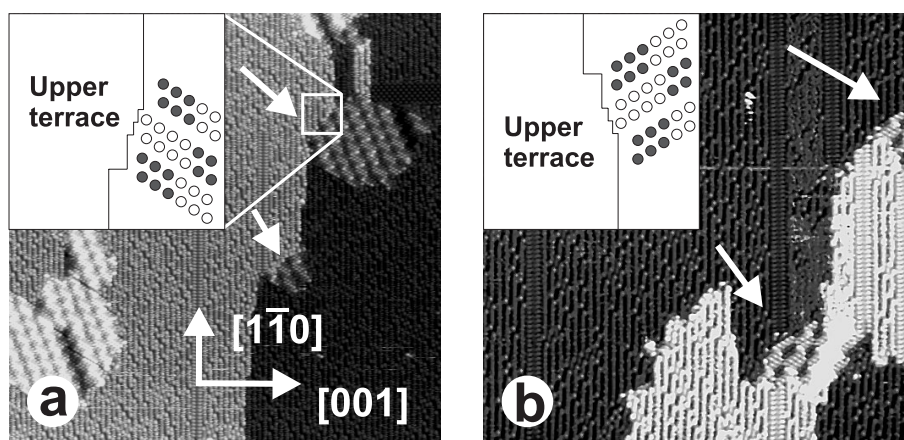


Figure 34: Cysteine structures on Au(110) after annealing the sample to 380 K.

(a) Terraces with islands of a dense L cysteine phase (marked by arrows) growing from *R* kinked step edges. Image size: $628 \text{ \AA} \times 694 \text{ \AA}$. Inset: Schematic model illustrating the bright and dark entities of the dense phase growing from a step edge. (b) Dense phase from D cysteine growing from the opposite, *S* kink sites, as sketched in the inset. Image size: $449 \text{ \AA} \times 495 \text{ \AA}$.

Fig. 35b, again demonstrating that the chirality of the cysteine molecules is reflected in the chirality of the molecular overlayer.

The formation of these chiral cysteine overlayers is interesting since it seems to involve more than one molecular layer and a substantial surface reconstruction, as will be discussed in the following. The mentioned height difference of 0.7 \AA between the bright and dark regions suggests that the bright regions constitute a second molecular layer. Furthermore, the angle of 55° and the orientation of the dense domains correspond to those defined by the alignment of the molecular dimers along the $(2,-2)$ direction, which results in an angle of 54.7° . This strongly indicates that the dense domains evolve from the highly reconstructed surface area formed by the aligned dimer arrays. This interpretation also explains why no dense phases are found in the case of adsorption of the racemic mixture. This would require the separation of the cysteine dimers into domains of homochiral ordered arrays. Due to the vacancy structure underneath, however, the dimers are relatively immobile once they have been formed, making the separation into homochiral domains very unlikely as this is accompanied by

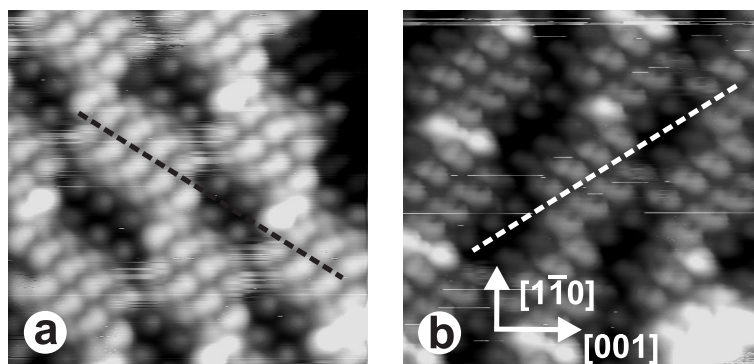


Figure 35: High-resolution image of the dense cysteine phase.

- (a) High-resolution image of the dense L cysteine phase with bright and dark areas suggesting a second layer of cysteine molecules. Image size: $70 \text{ \AA} \times 70 \text{ \AA}$.
 (b) High-resolution image of the dense phase formed by D cysteine. Image size: $70 \text{ \AA} \times 70 \text{ \AA}$.

a large mass transport. The situation is different in the case of enantiomerically pure cysteine on the surface. In this case, the individual dimers only need to diffuse a few lattice constants in order to align into ordered arrays, a process for which the thermal energy supplied during annealing seems to be sufficient.

4.5.4 Full monolayer coverage

When further increasing the cysteine coverage, the whole surface is eventually covered by cysteine. At room temperature, no ordering exists within these films, as discussed in section 4.2. Upon annealing, however, ordered overlayer structures were identified.

When reaching a substrate temperature of about 330 K, molecular islands are formed, which are elongated in the $[1\bar{1}0]$ direction, as shown in the overview in Fig. 36a. A zoom-in of an island is shown in Fig. 36b, and the $c(2 \times 2)$ unit cell of this structure is depicted in the STM image. The corresponding LEED data are depicted in Fig. 37. The LEED patterns were monitored during annealing of the sample from room temperature to 450 K. When reaching a substrate temperature of about 330 K, a diffuse $c(2 \times 2)$ LEED pattern develops, as shown in Fig. 37a, which gradually evolves into a more pronounced $c(2 \times 2)$ pattern. This pattern (Fig. 37b) consists of diffraction spots elongated in the

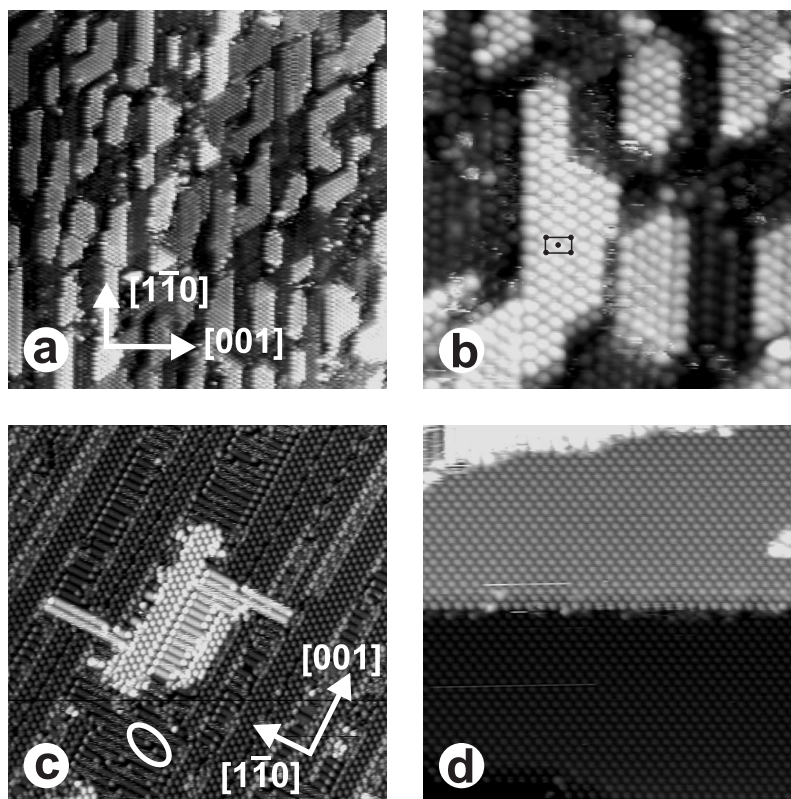


Figure 36: STM images showing the $c(2 \times 2)$ and $c(4 \times 2)$ structures.

(a) STM image after high-coverage cysteine adsorption and subsequent annealing at 380 K. Elongated islands are seen oriented along the $[1\bar{1}0]$ direction. Image size: $500 \text{ \AA} \times 500 \text{ \AA}$. (b) Zoom-in on an island shown in (a) disclosing the $c(2 \times 2)$ cysteine structure. Image size: $150 \text{ \AA} \times 150 \text{ \AA}$. (c) Upon further annealing at 420 K, the molecules partly desorb. The observed $c(4 \times 2)$ structure forms elongated stripes perpendicular to the $[1\bar{1}0]$ direction. Note that this image is rotated with respect to the orientation of the other images in this panel. Image size: $500 \text{ \AA} \times 500 \text{ \AA}$. (d) Eventually the molecules desorb and the remaining sulphur forms extended $c(4 \times 2)$ domains. Image size: $300 \text{ \AA} \times 300 \text{ \AA}$.

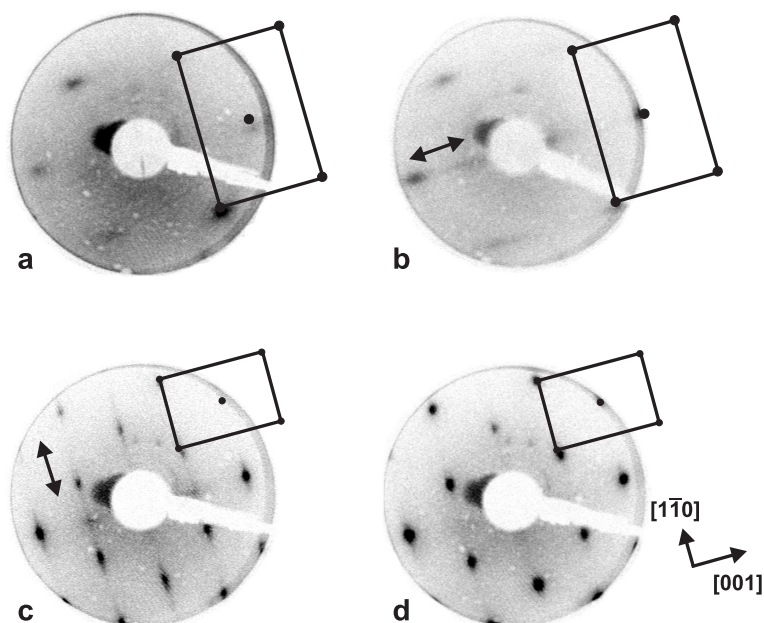


Figure 37: LEED patterns monitored during annealing of a Au(110) surface covered with L cysteine.

(a) A diffuse $c(2 \times 2)$ structured LEED pattern recorded after annealing the gold surface to ~ 330 K (28 eV). (b) Upon further annealing, the $c(2 \times 2)$ structure becomes more pronounced, the spots are elongated along the [001] direction (21 eV). (c) Upon annealing at about 400 K, the diffraction spots evolve into a $c(4 \times 2)$ pattern. For this structure, the diffraction spots are elongated along the $[1\bar{1}0]$ direction (30 eV). (d) Further annealing improves this structure eventually resulting in a clear $c(4 \times 2)$ pattern (27 eV).

[001] direction, in agreement with $c(2 \times 2)$ islands, which are well defined in the $[1\bar{1}0]$ direction, but less well developed along the [001] direction.

It is interesting to note that the $c(2 \times 2)$ structure reflects no chirality. This may be explained by the particular binding geometry of the cysteine molecules in this high-coverage structure. One explanation could be that the cysteine molecules in this very dense, annealed phase adopt a “standing-up” geometry similar to the case of alkanethiols on Au(111) with only the sulphur atom form-

ing a bond to the gold surface. It is, however, not possible to determine the detailed adsorption geometry from the STM images.

When annealing at 400 K, a $c(4 \times 2)$ structure emerges that forms widespread stripes along the $[001]$ direction, as shown in Fig. 36c. Coexisting with the $c(4 \times 2)$ structure, few cysteine dimers exist on the surface, and one dimer is marked in the image by an ellipse. As the $c(4 \times 2)$ structure is stable at temperatures well above the cysteine decomposition temperature, it cannot originate from intact cysteine molecules. Atomic sulphur is known to form a $c(4 \times 2)$ superstructure on Au(110) [118, 119], as discussed in more detail in chapter 5. Accordingly, the observed $c(4 \times 2)$ structure is ascribed to atomic sulphur, emerging after cysteine dissociation and forming stripes perpendicular to the $[1\bar{1}0]$ direction. At this temperature, the surface is refaceted and exhibits rectangular terraces (see also Fig. 38a), which is an indication for a substantial mass transport upon formation of this $c(4 \times 2)$ sulphur structure. The corresponding LEED pattern is reproduced in Fig. 37c, revealing a $c(4 \times 2)$ structure with diffraction spots elongated in the $[1\bar{1}0]$ direction, in accordance with the observed stripes that are less well defined in the $[1\bar{1}0]$ direction.

Upon increasing the annealing temperature to 420 K, the LEED pattern improves and eventually exhibits a well-pronounced $c(4 \times 2)$ structure, as shown in Fig. 37d. At this stage, all cysteine molecules are desorbed from the surface and the remaining sulphur forms extended $c(4 \times 2)$ domains (Fig. 36d), which desorb at a substrate temperature of about 570 K.

4.6 Chiral symmetry breaking

Nature is homochiral in the sense that in general only one enantiomer of a given molecule is involved in life processes. In DNA exclusively D sugars are used, whereas solely L amino acids exist in natural proteins. The origin of this homochirality has attracted substantial attention, since chirality seems to be a prerequisite for life, and the question about chiral asymmetry is thus related to the origin of life [154–156]. While it is conceivable that a given chiral asymmetry is inherited or even amplified for example by an asymmetric autocatalytic process [177], the reason for a possible event breaking the chiral symmetry in the first place is still unknown, although several speculations exist, ranging from parity violation in β decay to extraterrestrial UV radiation of neutron stars [178, 179]. Besides these theories, the enantiospecific adsorption of molecules resembling those that are biologically important onto chiral mineral surfaces such as calcite [155] and quartz [180] has been mentioned as a possible explanation. This discussion may explain the growing interest in experiments demonstrating chiral asymmetry.

The formation of homochiral phases from a racemate or from achiral molecules has been reported before [181, 182]. Chiral symmetry breaking has been demonstrated during crystallisation of sodium chlorate [181], which forms chiral crystals whereas the individual molecule possesses no chirality. When crystallised from a stirred solution, nearly 100% of the chlorate crystals had the same chirality. But in contrast to the results presented here, statistically the chiral symmetry was maintained, since upon repeating the crystallisation experiment both pure L and pure D phases were formed with the same probability. In a recent paper, the autocatalytic amplification of randomly generated trace chiral excess was proposed [183, 184].

4.6.1 STM results

An interesting phenomenon apparently involving a breaking of chiral symmetry was observed for high-coverage evaporation of the racemic mixture of cysteine, DL cysteine.

As discussed in section 4.5.4, the as-deposited, high-coverage films possess only poor ordering at room temperature and gentle annealing results in the formation of small, elongated domains with a $c(2 \times 2)$ structure. Further annealing of the substrate to 420 K, however, results in a prominent change. The surface is now refaceted, forming large rectangular terraces. A terrace subjected to this treatment is shown in Fig. 38a. The terraces are frequently terminated by the previously discussed $c(4 \times 2)$ sulphur structure (see also chapter 5), forming widespread stripes over more than 1000 Å along the [001] direction

(Fig. 38b). The remaining surface is covered with molecular pairs, as depicted in Fig. 38c. The pairs desorb upon further annealing at 440 K in agreement with the observation for submonolayer deposition, whereas the $c(4 \times 2)$ sulphur structure desorbs after annealing at 570 K. Compared to the data presented in the previous sections, the images shown in Fig. 38 exhibit a substantially higher tunnel noise, which can be seen as small, horizontal stripes. This is interpreted as fast diffusing particles on the surface, which is confirmed upon cooling the sample to around 120 K, where the noise vanishes and additional particles are observed. These particles are ascribed to fragments of the molecules emerging during the formation of the sulphur structure.

The observation relating to chiral symmetry breaking is obtained when the chirality of the remaining molecular pairs is analysed. By evaluating the molecular pairs, a striking excess of L cysteine compared to D cysteine pairs is disclosed. Nearly 92% of the 308 dimers analysed are L cysteine dimers, whereas only 8% are D cysteine dimers. This is highly surprising since the racemic mixture (i.e., a 50% - 50% mixture of D and L cysteine) was evaporated. One explanation may be that the excess of L cysteine dimers develops locally on the surface, while overall the 50% - 50% distribution is maintained. To investigate this possibility, several surface areas were examined, always revealing an L cysteine excess. These experiments exclude the observed excess of L cysteine dimers being only a local phenomenon. Additionally, the observed imbalance may possibly result from a process randomly producing an excess of L or D cysteine pairs covering the whole surface with equal probability for L and D cysteine. The repetition of the experiment should then lead to a 50% - 50% distribution of experiments with an L and D cysteine excess, respectively, statistically maintaining the chiral symmetry. For that reason, the experiment was repeated six times, always leading to an L cysteine excess. This rules out the possibility of a statistically effect, as in this case the possibility for six experiments with the same enantiomeric excess would equal $(\frac{1}{2})^6 = \frac{1}{64}$.

4.6.2 Possible origin of the symmetry breaking

Possible origins for the observed excess of L cysteine are discussed in the following. An explanation would be if the used racemic mixture would exhibit an imbalance between L and D cysteine. To ensure that the used powder of DL cysteine is an exact 50% - 50% mixture, the optical rotation of the used powder was measured, confirming a 1:1 mixture within an error of a few tenths of a percent. One may speculate that an imbalance might still be possible by having small crystallites of pure L and D cysteine in the used mixture, and by chance more L cysteine crystallites happen to be evaporated during the de-

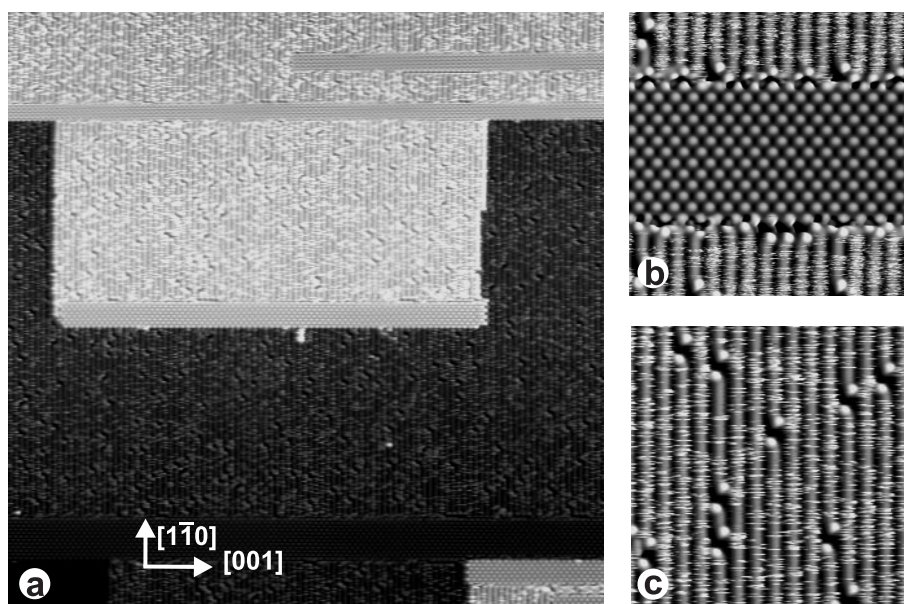


Figure 38: High-coverage DL cysteine after subsequent annealing of the sample to 420 K.

(a) Terraces after high-coverage evaporation and subsequent annealing of the surface at 420 K. Image size: $897 \text{ \AA} \times 991 \text{ \AA}$. A striped phase exists, extended over several 1000 \AA along the $[001]$ direction. A zoom-in on this structure is depicted in panel (b) (Image size: $135 \text{ \AA} \times 149 \text{ \AA}$), and a high-resolution image of the pairs on the remaining terrace is reproduced in (c) (Image size: $269 \text{ \AA} \times 297 \text{ \AA}$). Almost exclusively L cysteine pairs are left on the surface.

position. Cysteine, however, belongs to the class of racemic compounds [80], having both enantiomers in the unit cell. Pure DL cysteine is, therefore, an exact 50% - 50% distribution of both enantiomers at the molecular level.

After having excluded the racemic mixture being the reason for the observed imbalance, the origin of the chiral asymmetry has to be attributed to another component in the experimental setup. The gold surface is the next candidate in this consideration. In order to affect the two enantiomers differently, the surface has to be chiral itself. A flat, reconstructed $(110)-(1 \times 2)$ surface is, however, mirror-symmetric and possesses no chirality. A step edge is not chiral

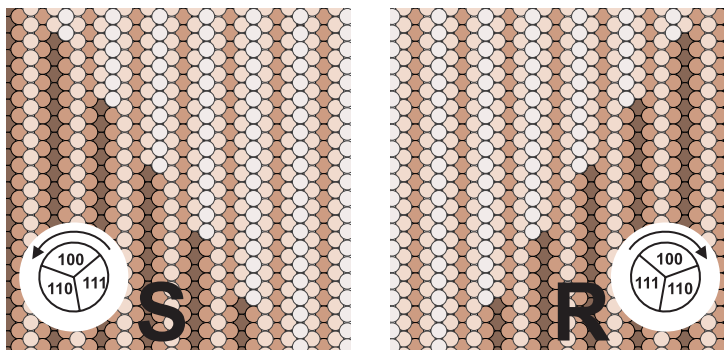


Figure 39: Model of a kinked Au(110) surface.

A kinked Au(110)-(1×2) surface and its mirror image demonstrating the chiral character of kink sites. In accordance with the notation for chiral surfaces introduced previously [161], the surface chirality is determined depending on the surface density of the microfacets at the kink site. On the (110)-(1×2) surface, two types of terraces can be envisioned, either forming (111) or (331) microfacets at the step edges [51]. Long straight steps are, however, always terminated by a (111) microfacet as drawn here, reflecting the high stability of this close-packed surface orientation.

either, but a kink site is indeed a chiral centre [86]. An illustration is given in Fig. 39, where two kinked, mirror-imaged (110)-(1×2) surfaces are shown. An explanation for the excess of L cysteine pairs on the terraces could be that the used gold surface exhibits an excess of kink sites of one type. It was already shown for the low-coverage regime that the two enantiomers of cysteine interact differently with the two types of kinks sites, as evidenced by the STM images given in Fig. 34, showing how high-density domains of L and D cysteine preferentially nucleate at the two different types of kink sites. It is thus possible that the kink sites may also influence the structures in the high-coverage regime discussed here.

To investigate this idea, it was attempted to deliberately introduce chiral surfaces. The experiment was repeated with two specially cut gold surfaces that were polished to represent mirror images of each other. The mirror-image gold surfaces were prepared by polishing two gold crystals cut along the (110) plane under an angle of 0.5° in the $[1\bar{1}0]$ direction and $\pm 0.5^\circ$ $[001]$ direction, respec-

tively, which for an idealised truncation of the bulk structure should yield kink site-terminated terraces with an average terrace size of about 110 Å. This angle of 0.5° is at the limit of the possible precision for aligning the gold crystals. The success of the special polishing of the gold surface is difficult to evaluate by STM due to the fact that STM is a local probe that allows only limited surface areas to be evaluated while the investigated surface may possess different areas on a micrometre length scale. An attempt was, however, made and STM images were recorded at random areas within the $1\mu\text{m} \times 1\mu\text{m}$ accessible range on the surface, evaluating the chirality of the kink sites at every place. Afterwards, the sample was moved macroscopically in the sample holder, thereby ensuring an independent surface area to be analysed. On one of the two specially polished surfaces, in the following referred to as Au(110) A, 101 images from nine macroscopically different areas were evaluated, revealing 76 areas with *S* kinks and 25 exhibiting *R* kinks, corresponding to 75% and 25%, respectively. The second surface, Au(110) B, was examined at 126 different places and showed 29 areas (23%) with *S* and 97 areas (77%) with *R* kinks. It thus appears that the special polishing of the samples yielded the desired chiral asymmetry of the surfaces.

Surface	D pairs		L pairs		sum
1. Au(110)	26	8%	282	92%	308
2. Au(110) A	173	13%	1163	87%	1336
3. Au(110) B	49	27%	130	73%	179
4. Au(110) C	147	30%	351	70%	498
overall	395	17%	1926	83%	2321

Table 2. Distribution of D and L cysteine pairs on four different gold (110) surface after high-coverage deposition and subsequent annealing at 420 K.

After probing the chiral character of the surface, high-coverage cysteine adsorption experiments as described above were performed on these surfaces as well as on a second Au(110)-(1 × 2) surface (C). Although the excess of L cysteine pairs varies from 92 to 70%, all surfaces show a significant excess of L cysteine pairs and in no instance an excess of D cysteine pairs was obtained, as listed in Table 2.

Having observed the L cysteine excess in the high-coverage regime after annealing at 420 K, the distribution of D and L cysteine pairs was evaluated also for the low-coverage regime upon submonolayer adsorption of the racemic mixture under the same conditions used for the experiments described in section 4.3. As listed in Table 3, analysing a total number of 6280 pairs revealed an excess of L cysteine, which amounts to 56% relatively independent of the surface. Thus,

also in the low-coverage regime the chiral asymmetry is manifest. This slight excess, which is significant on the basis of the large number of cysteine dimers counted, was not recognised in the previous experiments as the amount of some hundred imaged pairs is not sufficient to detect this small imbalance.

Surface	D pairs		L pairs		sum
1. Au(110)	651	42%	892	58%	1543
2. Au(110) A	1194	44%	1546	56%	2740
3. Au(110) B	268	46%	320	54%	588
4. Au(110) C	644	46%	765	54%	1409
overall	2757	44%	3523	56%	6280

Table 3. Distribution of D and L cysteine pairs on four different gold (110) surface after submonolayer deposition and annealing at 380 K, demonstrating an excess of L cysteine pairs for all surfaces.

Although the deposited mixture was carefully checked to be a 50% - 50% mixture within the experimental uncertainty, a small imbalance below this level could possibly be amplified by some autocatalytic process [185]. To test this hypothesis, an enantiomeric excess of D cysteine was deliberately introduced. A mixture of 70% D and 30% L cysteine was prepared, and the resulting distribution of D and L cysteine pairs in the low-coverage regime was counted. A total amount of 649 dimers revealed 312 (48%) D and 337 (52%) L cysteine pairs. Strikingly, also for an initial mixture with a D cysteine excess, the resulting dimers on the surface revealed an excess of L cysteine, excluding the possibility of an autocatalytic amplification.

In summary, chiral symmetry breaking was observed both for low and high cysteine coverages, showing an excess of L cysteine pairs relatively independent of the substrate surface. Although different possible origins for the chiral symmetry breaking were tested, the reason for the observed imbalance remains unclear. A similar problem has been reported recently, concluding that unknown impurities may lead to the observed enantiomeric excess [183, 184]. As the question of chiral symmetry breaking is related to many open questions of the origin of life, the effort of addressing the origin of the observed chiral symmetry breaking is included in this thesis although the results at present remain inconclusive.

4.7 Self-assembly of chiral nanoclusters

The results discussed in the previous sections were obtained at sample temperatures at or above room temperature. Cysteine deposition at low temperatures may result in the formation of other structures, as processes or reactions requiring a certain activation energy such as surface reconstruction or the formation of the dehydrogenated cysteine species, cysteinate, may be hampered or prohibited. Here the observation of a complex self-assembly process of this natural amino acid is presented. As amino acids are the fundamental building blocks of proteins, their intermolecular interactions and self-assembly is relevant for the properties and functioning of proteins.

Self-assembly is the basis for many processes in molecular biology and medical chemistry, and living systems involve a rich variety of self-assembly, such as the sophisticated folding of peptides into protein structures with very specialised functions [40, 41]. Understanding self-assembly in biologically relevant systems may therefore contribute to the understanding of life processes and can be related to the question how life emerges from basic interactions between individual molecules.

Also for the fabrication of functionalised nanostructures [35], self-assembly is one of the few practical strategies. The self-assembly of supported molecular structures can be controlled by selectively tuning intermolecular interactions [88], as discussed in section 3.3.1. Recently, self-assembly of molecular nanostructures based on the selectivity and directionality of hydrogen bonds has been demonstrated [90, 186], and molecular nanocluster formation has been reported upon [97], based on a simple closed-shell geometry similar to the situation observed in magic nanoclusters of metals [57, 187].

4.7.1 STM results and discussion

At submonolayer coverages of L cysteine deposited onto a Au(110)-(1 × 2) sample at 120 K, irregular agglomerates are observed, as shown in Fig. 40a. In this STM image, two gold terraces are seen characterised by the bright close-packed rows separated by atomic troughs running in the $[1\bar{1}0]$ direction. The terraces are covered with small, irregular agglomerates of various sizes. These islands are formed by a species, which is about 7 Å in size, corresponding to the size of individual cysteine molecules. The formation of these islands indicates that the molecules possess sufficient mobility to diffuse and nucleate either at 120 K or during the sample transfer from the manipulator into the STM, which results in a rise in temperature to about 140 K. It can thus be concluded that the molecules are mobile at temperatures around 140 K, and probably already below this temperature.

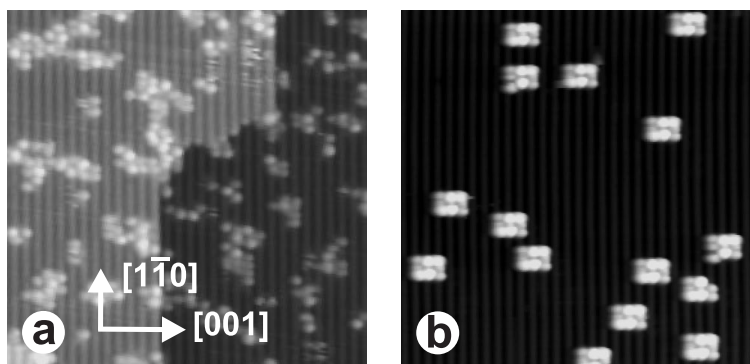


Figure 40: Cysteine as deposited at 120 K and after annealing at 270 K.

(a) Cysteine as deposited at 120 K. Islands varying in size formed by cysteine molecules are observed. Image size: $245 \text{ \AA} \times 245 \text{ \AA}$. (b) After annealing at 270 K perfectly monodisperse clusters are formed. Image size: $245 \text{ \AA} \times 245 \text{ \AA}$.

A self-assembly process is observed when annealing the gold substrate to 270 K. The cysteine islands are dissolved and the cysteine molecules self-assemble into a new structure as the entire surface is now covered with nanoclusters of uniform size, as demonstrated Fig. 40b. A high-resolution image of an L cysteine cluster is shown in Fig. 41a. The clusters have a size of about 24 \AA in the $[001]$ direction and 18 \AA parallel to the $[1\bar{1}0]$ direction, as shown in the height profiles in Figs. 41c and d, respectively. They consist of a centre part composed of two sub-units aligned along the $[1\bar{1}0]$ direction with an apparent height of about 2.3 \AA compared to the height of the gold atoms in the topmost atomic row. This centre is surrounded by three smaller units on each side which lie on top of the neighbouring close-packed rows. These smaller units have a height of about 1.5 \AA , except the upper left and lower right corner entities, which are approximately 0.4 \AA higher. The appearance of the clusters and the heights of the sub-units are slightly modified when imaged under different tip conditions, as shown in Fig. 41b. In this image, the internal structure of the side-entities surrounding the centre parts is resolved with more details compared to the cluster shown in Fig. 41a.

The corner entities, which are imaged brighter, appear to be less strongly bound, since molecular clusters of L cysteine can be found, which lack exclusively the lower right or the upper left or both corner units, as shown in

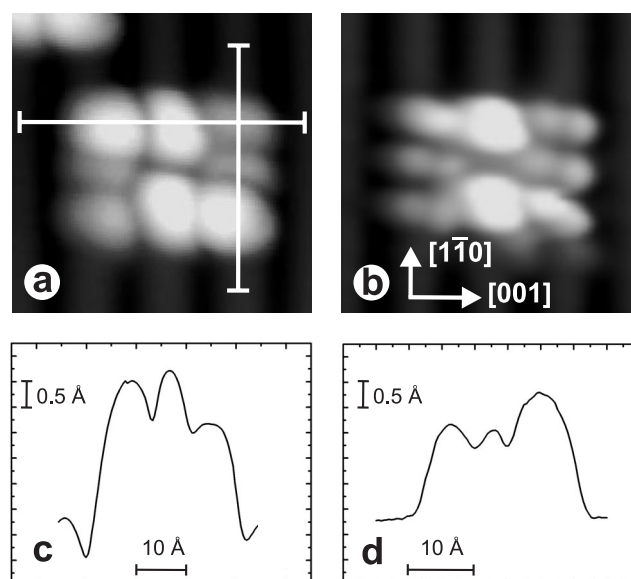


Figure 41: High-resolution cysteine nanoclusters.

- (a) High-resolution image of an L cysteine cluster. Image size: $32 \text{ \AA} \times 32 \text{ \AA}$.
 (b) Imaged under different tip conditions: the appearance of the cluster is slightly modified. Same image size. (c) Height profile over the cluster along the $[001]$ direction and (d) along the $[1\bar{1}0]$ direction as marked by the white lines in (a).

Fig. 42a. Among hundreds of observed nanoclusters assembled after annealing at 270 K, not a single structure has been seen differing in shape apart from the lack of the bright corner entities.

The gradual formation of the clusters can be followed by stepwise increasing the annealing temperature. When annealing at 220 K, the surface is covered with cysteine clusters which still differ in size, but look similar to the clusters reported upon here. Upon annealing at 260 K, the presented clusters are formed, but about 37% lack one corner entity and an amount of 7% lack both corner units. Further annealing at 270 K leads to 71% complete clusters, 26% with one missing entity and 3% clusters where both corners are lacking. The clus-

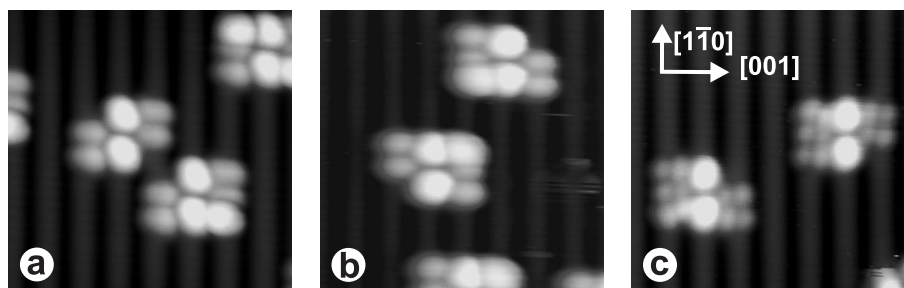


Figure 42: STM images demonstrating the chirality of the nanoclusters.

(a) L cysteine clusters with exclusively the upper left and/or the lower right corner entity missing. Image size: $65 \text{ \AA} \times 65 \text{ \AA}$. (b) In the case of D cysteine nanoclusters, the opposite corner units are missing, namely the upper right and the lower left. Same image size. (c) Nanoclusters formed from the racemic mixture are identical to those observed for pure L and D cysteine.

ters dissolve when the temperature is further increased, and the poorly ordered rows are formed as observed after room-temperature deposition (section 4.2), followed by the formation of cysteine dimers and double rows, as reported upon in the preceding sections.

The different appearance and binding of the corner entities break the mirror symmetry of the system, demonstrating the chirality of these L cysteine nanoclusters. Nanoclusters formed from D cysteine are depicted in Fig. 42b. They are similar to those observed for L cysteine, except that now the lower left and upper right corner entities either appear brighter or are missing. The clusters formed from D cysteine are thus mirror images of those formed from L cysteine. When evaporating the racemic mixture of D and L cysteine such that both chiral forms are present at the surface at the same time, again molecular nanoclusters are formed, as shown in Fig. 42c. The clusters are identical in appearance to those observed when depositing the D and L enantiomers separately. Furthermore, not a single structure was observed, which could give an indication for heterochiral DL clusters such as clusters with bright or missing corner entities at the same side of a cluster. This strongly suggests that the nanoclusters formed from the racemic mixture are homochiral, hence demonstrating chiral recognition during the self-assembly of these supramolecular nanoclusters.

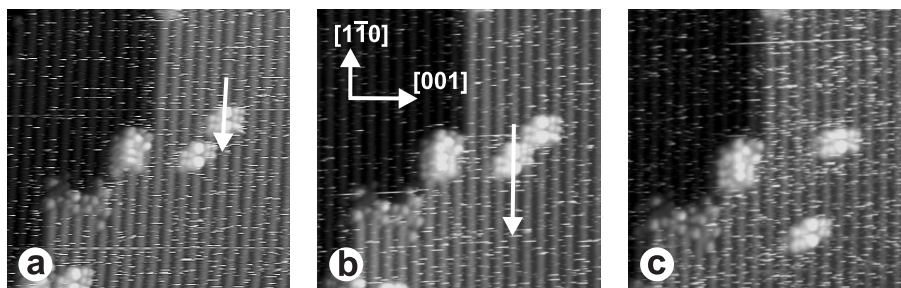


Figure 43: Lateral manipulation of a cysteine nanocluster.

Sequence of STM images showing the lateral manipulation of nanoclusters with the STM tip. The arrows mark the tip movement. Image sizes: $163 \text{ \AA} \times 163 \text{ \AA}$.

4.7.2 Cluster manipulation and diffusion

To probe cluster-cluster as well as cluster-substrate interactions, manipulation experiments were performed. Lateral manipulation of the clusters with the STM tip was carried out at temperatures around 260 K. The tip was brought into close proximity of the surface by increasing the tunnelling current to $\sim 0.8 \text{ nA}$ and decreasing the tunnelling voltage to 80 mV, corresponding to a tunnelling resistance of $100 \text{ M}\Omega$. A line over the cluster was defined and the tip was subsequently moved along this pathway. When the tip apex reaches the cluster, it interacts with the cluster and eventually either pulls or pushes the entire cluster and thereby manipulates the cluster laterally. From the tip-height curves it can be deduced whether the manipulation is performed in the *pushing* or *pulling* mode [188] when manipulating atoms. In the present case, the manipulation mode is, however, difficult to clarify, since many molecules are involved in the manipulation process.

Attempts to manipulate at a temperature of 120 K failed, indicating that thermal activation is necessary to perform the manipulation. With the parameters mentioned above, the entire cluster can be moved along the close-packed rows, whereas it was not possible to manipulate the cluster perpendicular to the $[1\bar{1}0]$ direction. This demonstrates that the diffusion barrier along the $[1\bar{1}0]$ direction is smaller than along the higher corrugated $[001]$ direction. Due to the anisotropic diffusion barriers, the diffusion of the clusters is one-dimensional and along the close-packed row direction. To study the diffusion of the clusters, the movie capability of the Aarhus STM was utilised. A movie recorded

at 260 K demonstrates the one-dimensional diffusion of the nanoclusters along the $[1\bar{1}0]$ direction, showing a smaller diffusion barrier in this direction compared to the $[001]$ direction, in agreement with the findings of the manipulation experiments.

The ability to manipulate the clusters opens up for the possibility to study the interaction between clusters. Preliminary experiments have been performed and are shown in Fig. 43. When moving two clusters into close proximity, they remain in close contact (Fig. 43b), suggesting that no strong repulsion appear between two clusters. In a second step (Fig. 43c), the clusters can be separated again, demonstrating that no strong attraction exist between the clusters either, which is already evident from the uniform size of the nanoclusters.

4.7.3 Possible nanocluster structure

In the following, a tentative model is proposed for the molecular structure of the cysteine nanoclusters. The number of atoms involved in the clusters is beyond the size manageable by DFT, making reliable *ab initio* calculations difficult. As a first approximation, the cluster has therefore been treated in terms of the individual functional groups involved, based on the knowledge that has been gained from the DFT calculations on the cysteine pairs discussed in section 4.3 and another DFT study on cysteine adsorbed on Au(111) [173]. In the latter work, it was demonstrated that the separate treatment of the functional groups of a cysteine molecule adsorbed onto a Au(111) surface agrees well with the calculation considering the entire molecule. This discussion therefore starts by reviewing the interactions of the separate functional group with a gold surface. The formation of hydrogen bonds between the oxygen atoms of the carboxylic group is very favourable since it is associated with an energy gain of about -0.68 eV (PW91) compared to two single cysteine molecules (see section 4.3). On the other hand, an interaction of the carboxylic group with the gold surface results in an increased total energy, confirming the assumption of hydrogen bonds between the oxygen atoms of the carboxylic groups.

The amino group gains about -0.3 eV by interacting with the substrate via the lone pair of the nitrogen atom and the gold surface. Additionally, due to the lone electron pair, the amino group can also be involved in hydrogen bond formation.

For methylthiolate on Au(111), adsorption on a bridge site has been shown to be energetically favourable by about -1.7 eV [121]. This situation differs, of course, from the cysteine molecule, where the mercapto group is bound to a longer carbon chain, but the adsorption on a bridge site may still be a reasonable starting point for the molecule adsorption. Since substantial de-

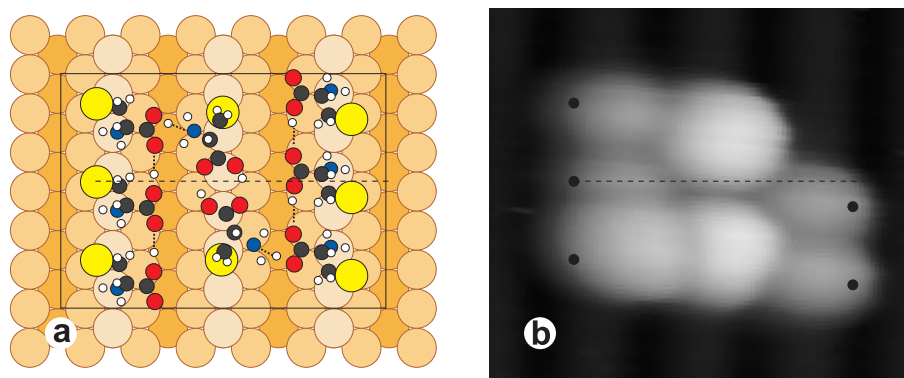


Figure 44: Structure suggestion for the cysteine nanocluster.

Structural model suggesting a possible arrangements of the molecules in a hydrogen-bonded network within a D cysteine nanocluster (a) and the corresponding experimental data (b).

hydrogenation and hence thiolate formation is assumed to occur only around room temperature and above [189], the formation of a strong sulphur–gold bond, as reported upon in the previous sections, seems unlikely in the present case of cysteine clusters. For the same reason, a disulphide bond between two mercapto groups is assumed not to be present here.

With these constraints, a structural model can be suggested, as depicted in Fig. 44a for a D cysteine cluster. The corresponding experimental data is shown in Fig. 44b. The central part of the cluster is formed by two bright features with a top-to-top distance of 8.7 Å, equivalent to three gold distances. These parts are surrounded by three units at both sides, whose maxima are separated by about 5.7 Å, corresponding to two gold distances. As mentioned before, the centre parts appear higher than the surrounding units, and the height difference amounts to 0.8 Å.

In the proposed model, the side entities are formed by cysteine molecules adsorbed with the mercapto group at a bridge site between a top gold atom and an atom in the second row, while the amino group is adsorbed on top of a neighbouring gold atom of the topmost gold row. The carboxylic group points away from the surface, forming hydrogen bonds with the neighbouring cysteine molecule (marked by dashed lines in the figure). The centre unit is formed by two cysteine molecules facing each other on top of the close-packed atomic

row, forming hydrogen bonds between their carboxylic groups. Also the centre molecules are adsorbed via the mercapto groups. In this geometry, the amino groups cannot interact with the surface but point sideways towards the two side entities. Therefore, the amino groups can contribute with the lone electron pair to the formation of an additional hydrogen bond to the side cysteine molecules and in this way stabilise the adsorption of two side cysteine molecules. The third cysteine molecule at the side is too far away to interact with the amino groups of the centre molecules and is therefore only attached to the cluster via one hydrogen bond, resulting in a weakly bound side entity.

The positioning of the mercapto group of the side molecules at a bridge site while simultaneously allowing for a binding of the amino group to the close-packed gold row results in a displacement by 1.44 Å along the $[1\bar{1}0]$ direction of the mercapto group adsorption site. This shift can be seen in the STM image and is visualised by the black dots marking the estimated sulphur positions. The observed height difference between the central and the side units can be explained in this model by both the amino group protruding outwards and the different position of the mercapto group. The higher appearance of the less strongly bound corner entities could be explained by the free oxygen atom of the carboxylic group which is not involved in hydrogen bonding. Thus, the presented model, despite being rather intuitive, seems to account for several features observed in the STM images.

This tentative model, however, also has its weak points. First, the assumption of the mercapto group binding at a bridge site is deduced from the adsorption position of the dehydrogenated thiolate group. With the hydrogen atom still attached to the sulphur atom, the adsorption position at low temperatures may differ from the situation at elevated temperatures. Second, when the less strongly bound corner entity is removed from the cluster, the neighbouring side molecule remains with only one hydrogen bond left. Thus, after removing the corner entity, the neighbouring cysteine molecule is equally weakly bound to the cluster, and clusters with also this molecule missing should exist. This has, however, never been observed experimentally. It must therefore be stressed that the presented model is of tentative nature and calls for a more thorough theoretical analysis that has not been possible in the frame of this thesis.

4.8 Summary and conclusions

The presented experiments allowed a multitude of cysteine structures on the Au(110)-(1 × 2) surface to be observed and various phenomena and mechanisms to be studied. The background for this variety is a subtle balance between molecule-molecule interaction on the one hand, and molecule-surface interaction on the other hand, whose relative influence can be controlled by changing

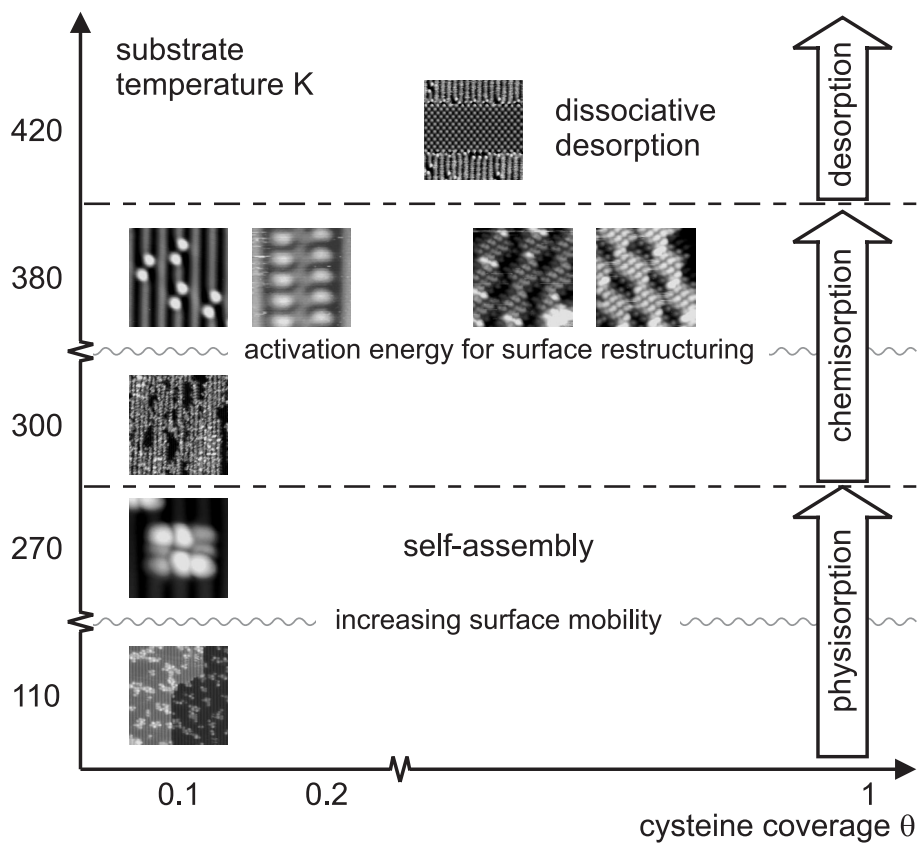


Figure 45: Phase diagram of the cysteine structures on Au(110)-(1 × 2).

Cysteine structures on Au(110)-(1 × 2) in dependence on substrate temperature and cysteine coverage.

the temperature of the system. At low temperatures, dehydrogenation of the mercapto group has not yet taken place, thus a strong molecule–gold interaction via the sulphur atom is not present at these temperatures. Therefore, molecule–molecule interaction dominates this temperature regime, allowing for the formation of the internally saturated nanoclusters, when providing sufficient energy for the diffusion of the individual molecules.

Increasing the temperature above 280 K, however, leads to the dissolution of the nanoclusters, as this temperature is associated with the transition from the cysteine to the dehydrogenated cysteinate species. With the formation of a covalent sulphur–gold bond, the influence of the substrate surface increases, leading to the formation of poorly ordered, anisotropic cysteine agglomerates. When sufficient energy is provided to activate an adsorbate-induced rearrangement of the substrate surface, dimer and double-row structure formation is observed. The ability of the sulphur atom to restructure the surface is based on both the high sulphur–gold binding energy and the particularly reactive (1×2) missing-row reconstructed surface that enables the molecules to locally rebuild the surface to create optimum adsorption sites for both cysteine dimers and rows. When the coverage is increased such that the density of dimers increases, an alignment of cysteine dimers in an ordered array is seen, in which the expelled gold atoms from the vacancy structures underneath the pairs are trapped in between the amino groups of two neighbouring cysteine pairs. This highly restructured surface region seems to be the template for the growth of chiral, more dense cysteine islands.

Upon further increase of the coverage, such that the whole surface is covered by cysteine, and subsequent annealing, the molecules adopt another surface structure, namely a $c(2 \times 2)$ structure. The $c(2 \times 2)$ pattern is achiral, which may be explained by the fact that the cysteine molecules in this very dense phase form a “standing-up” geometry as known from alkanethiol films on Au(111). Annealing above 420 K results in the dissociative desorption of the cysteine molecules, which leaves atomic sulphur behind on the surface. Finally, atomic sulphur lifts the missing-row reconstruction of the Au(110) surface and forms a $c(4 \times 2)$ structure.

5 Sulphur on Au(110)

In the previous chapter, the formation of a $c(4 \times 2)$ superstructure on Au(110) upon decomposition of adsorbed cysteine molecules has been reported. It was speculated that the origin of this structure was atomic sulphur from the decomposed molecules. To validate this idea, hydrogen sulphide (H_2S) adsorption studies have been performed. Based on STM images, a model is proposed for the sulphur adsorption site within this structure, involving the lifting of the missing-row reconstruction.

5.1 H_2S on Au(110)

Hydrogen sulphide has been deposited onto Au(110)- (1×2) by vapor deposition from a gas bottle, which is connected to a ~ 20 cm long dosing tube inside the chamber via a needle valve. The chamber has been backfilled with H_2S at a pressure of about $5 \cdot 10^{-8}$ mbar. To increase the molecular flux at the sample, the sample has been positioned in front of the tube during H_2S dosing. These dosing conditions make it difficult to specify the amount of Langmuir ($1 \text{ L} \equiv 1 \times 10^{-6}$ torr·s) deposited. The gold substrate has been held at 470 K during the molecular deposition in order to decompose the molecules at the surface.

An overview of the surface structures after H_2S dosing is shown in Fig. 46a. Large islands with a $c(4 \times 2)$ structure can be found, which extend over several hundred Ångströms in the [001] direction, while being relatively confined along the $[\bar{1}\bar{1}0]$ direction. A rectangular shape is characteristic for these $c(4 \times 2)$ islands, in agreement with the results presented in section 4.6. Additionally, small islands of another structure are observed. These islands exhibit an elliptic shape, slightly elongated along the [001] direction, as demonstrated in Fig. 46b. The STM images may suggest the elliptic island being adsorbed on top of the $c(4 \times 2)$ structure, however, the characteristics of this structure contradict this possibility, as will be discussed below.

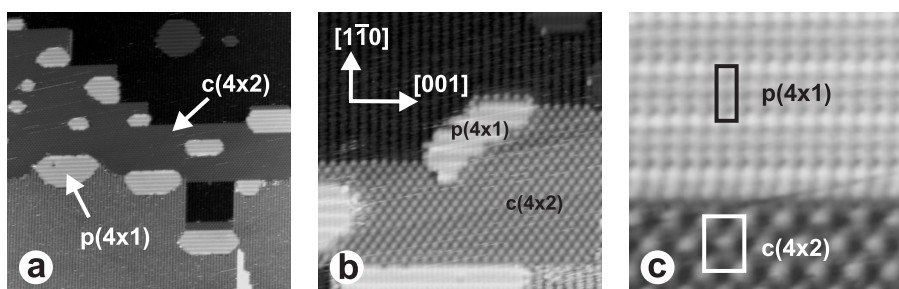


Figure 46: Au(110) after 15 min dosing of H_2S at a sample temperature of 470 K.

- (a) Overview of the surface after H_2S dosing. A large region with a $c(4\times 2)$ structure and smaller islands of elliptic shape is seen. Image size: $783 \text{ \AA} \times 783 \text{ \AA}$.
 (b) Zoom-in on the $c(4\times 2)$ and (4×1) structures. Image size: $228 \text{ \AA} \times 228 \text{ \AA}$.
 (c) High-resolution image of the (4×1) structure shown in the upper part of the image and the $c(4\times 2)$ structure in the lower part. Image size: $60 \text{ \AA} \times 60 \text{ \AA}$.

A zoom-in on both structures is given in Fig. 46c, disclosing a $p(4\times 1)$ periodicity with three entities per unit cell for the elliptic islands and the already mentioned $c(4\times 2)$ structure with two features in the unit cell. From this, the sulphur coverage in the $p(4\times 1)$ structure is calculated to $\theta = \frac{3}{4\times 1} = 0.75$, while it is $\theta = \frac{2}{4\times 2} = 0.25$ for the $c(4\times 2)$ structure.

Upon annealing at 520 K, the $c(4\times 2)$ structure remains stable, in agreement with the observation reported previously for atomic sulphur on Au(110), which has been found to form a $c(4\times 2)$ pattern [118, 119]. The bright protrusions of the $c(4\times 2)$ structure are therefore assigned to originate from atomic sulphur, which is known to be imaged as a protrusion [190]. This $c(4\times 2)$ sulphur structure observed after H_2S dosing is in all dimensions identical to the $c(4\times 2)$ structure revealed after the cysteine decomposition on Au(110). It is therefore concluded that the $c(4\times 2)$ structure obtained after cysteine decomposition is indeed a sulphur structure. To determine the adsorption positions of the sulphur atoms, an image is analysed that shows both the $c(4\times 2)$ structure and molecular cysteine pairs that have been introduced before (section 4.3).

In Fig. 47a, the $c(4\times 2)$ atomic sulphur structure is found to the left in the STM image. A height profile along the $[1\bar{1}0]$ direction given in Fig. 47b demonstrates that the close-packed gold row is about 0.2 \AA higher than the sulphur structure, strongly suggesting that the topmost close-packed gold rows are removed

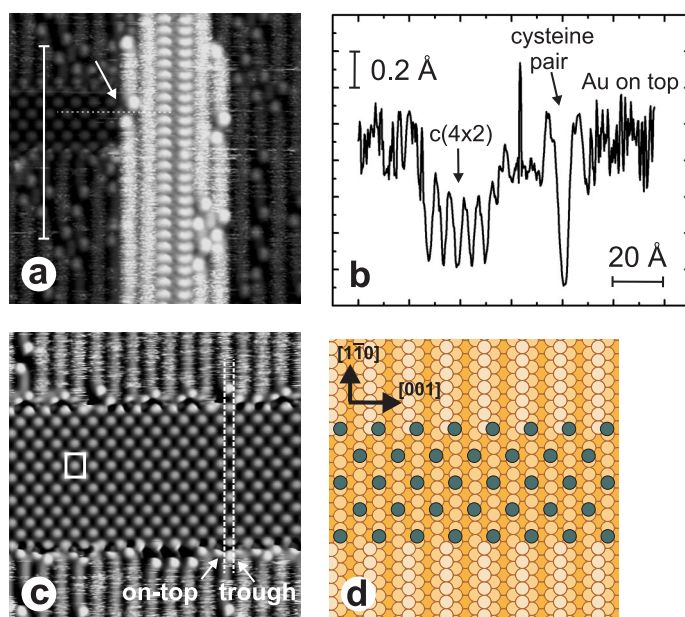


Figure 47: STM image of the $c(4 \times 2)$ sulphur structure.

(a) STM image after cysteine dosing and annealing at 420 K. The $c(4 \times 2)$ structure is seen to the upper left. Image size: $131 \text{ \AA} \times 144 \text{ \AA}$. (b) Height profile over the $c(4 \times 2)$ structure demonstrating that the close-packed gold rows are about 0.2 \AA higher than the $c(4 \times 2)$ structure. The position of this height profile is indicated by the white line in (a). (c) STM image of the $c(4 \times 2)$ structure. A unit cell is marked in the image. Image size: $131 \text{ \AA} \times 144 \text{ \AA}$. (d) Structural model for the adsorption site of the sulphur atoms within this structure, which involves a lifting of the missing-row reconstruction.

underneath the sulphur structure. By removing the topmost close-packed gold rows, the (1×2) missing-row reconstruction is lifted and an unreconstructed $(110)-(1 \times 1)$ surface emerges. Furthermore, in the $[001]$ direction the sulphur position is seen to be centred between the on-top position of the added gold rows and the centre of the atomic troughs, as demonstrated by the white, dashed lines in Fig. 47c. This is an indication that the sulphur atoms are adsorbed on

top of the close-packed gold rows of the second gold layer (see Fig. 47d). To determine the exact sulphur position in the $[1\bar{1}0]$ direction, atomic resolution within the close-packed rows along the $[1\bar{1}0]$ direction is required. With tunnel parameters suitable for imaging molecular and atomic adlayers, atomic resolution within the close-packed rows has not been achieved. However, employing the detailed knowledge of the cysteine pair adsorption site obtained from the DFT calculations (see section 4.3), the exact position of the sulphur atoms in the $c(4\times 2)$ structure can be determined. In Fig. 47a, a cysteine pair is found on a second gold layer on the terrace with the $c(4\times 2)$ sulphur structure. The centre of the molecular pair is known to be positioned over a bridge site of the topmost close-packed gold row. As a bridge position corresponds to an on-top position in the gold layer underneath, the number of gold layers separating the molecular pair and the sulphur atoms has to be considered. The sulphur structure is found in the terrace underneath the smaller gold terrace with the cysteine pair. Additionally, as argued above, the topmost gold row is removed underneath the sulphur structure, and the position of the centre of the cysteine pair thus corresponds to a bridge site in the gold layer where the sulphur atoms are adsorbed. As shown by a dashed line in Fig. 47a, the centre of the cysteine pair coincides with the position of the sulphur atoms in the $[1\bar{1}0]$ direction; the sulphur atoms are thus found to adsorb at a bridge site and a final structure suggestion is given in Fig. 47d. In this model, the sulphur atoms are adsorbed at the bridge sites on top of the topmost close-packed gold rows of an unreconstructed Au(110) surface.

Having established a model for the adsorption position of the sulphur atoms in the $c(4\times 2)$ structure, the position of the entities within the $p(4\times 1)$ structure can be determined. First, it is assumed that this structure is adsorbed onto a gold surface where the missing-row reconstruction has been lifted. This is motivated by the very small corrugation of the (4×1) structure along the $[001]$ direction. This is, however, not proof that the reconstruction is lifted. As shown in Fig. 48a, the rows defined by the position of maxima of the (4×1) structure along the $[1\bar{1}0]$ direction coincide with those of the $c(4\times 2)$ structure; the entities of the (4×1) structure are thus also adsorbed on top of the close-packed rows of the unreconstructed gold surface. One of the three species within the unit cell is imaged brighter, leading to bright stripes running along the $[001]$ direction in the STM image. The different appearance in the STM image can readily be explained by different adsorption sites, which arise from the fact that three species are placed on top of four lattice spacings along the $[1\bar{1}0]$ direction. If a bright feature is associated with species adsorbed at an on-top position, the neighbouring two dimmer protrusions originate from entities adsorbed at bridge positions, resulting in a moiré pattern, as illustrated in the

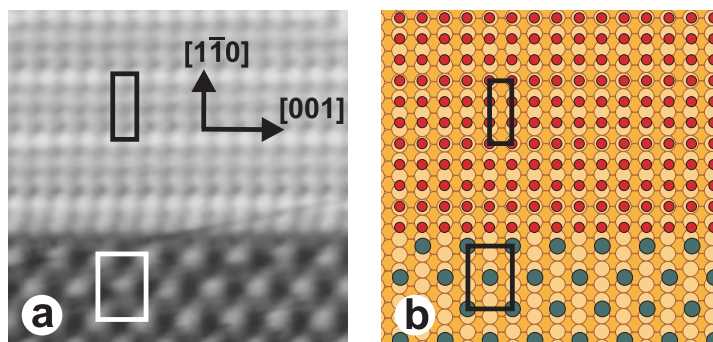


Figure 48: STM image and model of the $p(4\times 1)$ sulphur structure.

(a) STM image showing the $c(4\times 2)$ structure in the lower part and the (4×1) structure (upper part). Unit cells of both structures are marked in the image. Image size: $60 \text{ \AA} \times 60 \text{ \AA}$. (b) Structural model for the adsorption site of the sulphur atoms within the (4×1) structure, showing two inequivalent adsorption sites.

model in Fig. 48b. The correspondence of the observed features of the (4×1) structure with the periodicity of the gold substrate rules out the possibility of the (4×1) structure being a second layer on top of the $c(4\times 2)$ structure, which would not give a clear rationale for the observed bright lines running along the $[001]$ direction. The structure does, however, not contradict the missing-row reconstruction existing underneath the (4×1) structure.

5.2 Conclusion

The presented adsorption study of H_2S on Au(110) confirms that the $c(4\times 2)$ structure observed upon decomposition of adsorbed cysteine indeed originates from atomic sulphur. This structure includes the lifting of the (1×2) missing-row reconstruction underneath, which has been suggested on the basis of LEED studies [118,119]. Within the $c(4\times 2)$ structure, the sulphur atoms were shown to adsorb at bridge positions on top of the close-packed rows of the unreconstructed Au(110). Coexisting with the $c(4\times 2)$ structure, another overlayer was identified on Au(110), forming a $p(4\times 1)$ structure in which the adsorbates

adopt two different adsorption sites, namely on-top and bridge positions. The presented investigation of sulphur on Au(110) demonstrates that surface restructuring upon sulphur adsorption is a common phenomenon, even for an inert surface such as gold. A restructuring of the substrate surface in order to create the most favourable adsorption sites seems thus more frequent than generally acknowledged, especially in the case of the adsorption of the very reactive sulphur [191, 192].

6 Cysteine on Au(111)

6.1 Au(111)

The (111) surface of an fcc crystal is the most densely packed and energetically most favourable plane. Au(111) exhibits the so-called *herring bone reconstruction*, which is due to a slightly compressed topmost layer with 23 surface atoms per $(22 \times \sqrt{3})$ unit cell, creating *hexagonally closed-packed* (hcp) and fcc stacking domains [52]. As mentioned previously, the majority of thiol adsorption studies have been carried out on this facet of gold. This is due to the fact that the (111) surface of gold is comparably easy to prepare and relatively stable in air. Gold (111) surfaces can be obtained by evaporating gold onto freshly cleaved mica or flat glass slides which are often coated with a few nanometres thick layer of chromium to improve adhesion. These gold samples can be exposed to air, and after flame annealing, the surface exhibits atomically flat (111) facets, which are a few hundred nanometres in size. The surfaces are supposed to be clean, although a thin layer of weakly adsorbed organic molecules forms within a short period of time when the surface is exposed to ambient conditions. [193]. For liquid phase adsorption experiments, the gold sample is simply immersed into a solution containing the molecules of interest and either studied *in situ* or subsequently dried and analysed *ex situ*. The ease of preparation turns these samples into a cheap and well-suited metal template for studying molecular adsorption.

6.2 Previous studies

Cysteine adsorption onto Au(111) has been studied in a number of instances during recent years [135–143]. In these studies, the molecule has been deposited from solution, except for one investigation where cysteine adsorption has been carried out from the vapor phase in UHV [143]. In the latter study,

however, polycrystalline surfaces have been used, preventing the determination of ordered superstructures. Several of these investigations have addressed the adsorption geometry and the binding of cysteine on the gold (111) surface [136–141, 143], concluding that the molecules undergo a transition from the thiol to the deprotonated thiolate species upon adsorption at room temperature and then bind covalently to the gold surface via the sulphur atom.

X-ray photoelectron spectroscopy experiments have revealed a shift of the S $2p^{3/2}$ peak corresponding to a gold–sulphur bond formation upon adsorption of cysteine onto Au(111) [137], similar to what is seen for the adsorption of 1-octadecanethiol onto Au(111) [138].

This view is also supported by STM adsorption experiments with the disulphide cysteine species, cystine ($\text{COOH-CH(NH}_2\text{)-CH}_2\text{-S-S-CH}_2\text{-CH(NH}_2\text{)-COOH}$), leading to very similar results as in the cysteine case, suggesting that the disulphide bond is dissociated upon cystine adsorption [140, 141].

Qingwen *et al.* have reported that the N 1s peak remained unchanged upon adsorption, leading to the conclusion that the amino group is not involved in the binding to the gold surface [139]. This is, however, in contrast to the findings of Ihs *et al.* [168] who have performed infrared spectroscopy on cysteine deposited onto thermally evaporated gold films, their results indicate that the amino group forms a bond to the gold surface via the lone pair.

STM studies have been carried out to determine the order within the cysteine adlayers deposited from solution [136, 140, 141]. Ulstrup and coworkers [140] have established a model for a close-packed overlayer of cysteine on Au(111) deposited from solution, consistent with a $(3\sqrt{3} \times 6)R30^\circ$ superstructure. In contrast to this, Dodero *et al.* [136] have presented STM results of a cysteine layer deposited from the liquid phase and imaged in air, showing a $(\sqrt{3} \times \sqrt{3})R30^\circ$ molecular structure. Their STM images demonstrate a lifting of the herringbone reconstruction upon cysteine deposition and the formation of monatomically deep holes in the molecular film.

From this review it appears that the adsorption of cysteine onto Au(111) is still a matter of some debate. When prepared by vapor deposition in UHV, the coverage can be controlled more precisely than when prepared from solution. In addition, the presence of a solvent during deposition from the liquid may influence the adsorption process. Finally, upon vapor deposition the molecule is supposed to adsorb in its neutral state while in solution cysteine exists in different states of ionisation (anionic, cationic, zwitterionic), depending on the pH value of the solution.

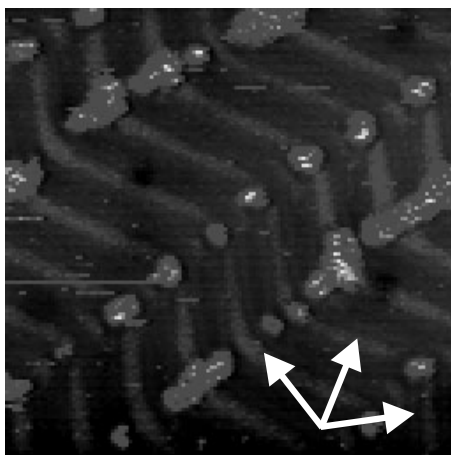


Figure 49: STM images after evaporation of cysteine onto Au(111) held at 120 K.

Nucleation of cysteine in the elbows of the herringbone reconstruction after evaporation at a sample temperature of 120 K. Image size: $500 \text{ \AA} \times 500 \text{ \AA}$.

6.3 Submonolayer coverage

Submonolayer coverages of L cysteine were investigated on Au(111) held at 120 K and at room temperature. Upon evaporation at a sample temperature of 120 K, cysteine molecules decorate step edges and molecular islands nucleate in the elbows of the herringbone reconstruction, similar to the situation observed upon evaporation of some metals on Au(111) [194–197]. This suggests a facile diffusion of the molecules even at such low temperatures. The clusters in the elbows are of various sizes, as apparent in the STM image in Fig. 49.

The situation is similar for evaporation at room temperature, where the molecules also nucleate at the elbows, as depicted in Fig. 50a. Additionally, elongated cysteine islands are observed at this temperature, preferentially growing from step edges and following the directions defined by the herringbone reconstruction. These islands, which exhibit no internal ordering, grow in size upon increasing cysteine exposure, as demonstrated in Fig. 50b. In addition, large domains of an ordered structure are found, coexisting with the unordered islands. A terrace covered with this ordered layer is shown on the upper terrace

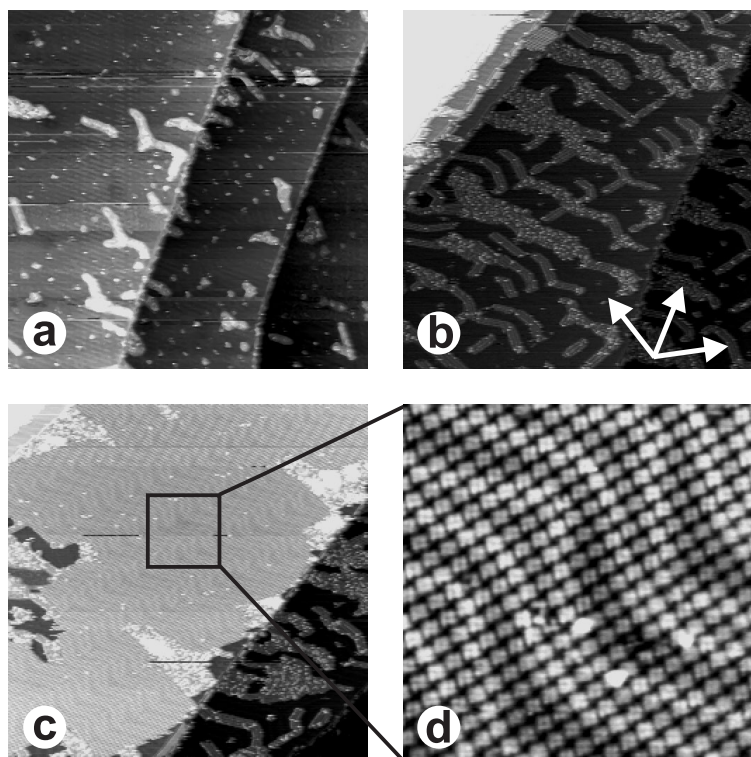


Figure 50: STM images after evaporation of cysteine on Au(111) held at room temperature.

(a) Nucleation in the elbows of the herringbone reconstruction and formation of unordered cysteine islands upon evaporation at room temperature. Image size: $1500 \text{ \AA} \times 1500 \text{ \AA}$. (b) Upon increased exposure time, the cysteine islands grow in size. Image size: $1000 \text{ \AA} \times 1000 \text{ \AA}$. (c) Coexisting with the unordered islands, a highly ordered overlayer structure is found. Image size: $1000 \text{ \AA} \times 1000 \text{ \AA}$. (d) Zoom-in on a terrace with an ordered overlayer of cysteine molecules. The underlying herringbone reconstruction is still seen. Image size: $200 \text{ \AA} \times 200 \text{ \AA}$.

to the left in Fig. 50c, whereas the unordered islands are seen on the lower terrace to the right. The underlying reconstruction of the Au(111) surface is preserved under this cysteine layer, as shown in the high-resolution image in

Fig. 50d, where the herringbone reconstruction modulates the apparent height of the adsorbate layer. Furthermore, for different domains of the overlayer, different orientations with respect to the high-symmetry directions of the substrate surface were observed.

The appearance of this overlayer depends on the tip condition, as demonstrated in Fig. 51a, where a tip change occurs during data acquisition. In the lower part of the image, a structure with bright and dark rectangles is observed, and a high-resolution image acquired with this tip mode is given in Fig. 51b. The unit cell of this structure (superimposed in the STM image in Fig. 51b) is quadratic and possesses fourfold symmetry. It has a side length of 12 Å and consists of four bright features with a top-to-top distance of about 4 Å. As an individual cysteine molecule has a size of about 5 Å, it is suggested that each of these protrusions corresponds to one molecule rather than a part of the molecule imaged with submolecular resolution.

Under different tip conditions, the appearance of this structure changes as shown in the STM image in Fig. 51c, where the four bright features are imaged larger, demonstrating how the measured dimensions depend on the actual tip conditions.

Upon annealing the submonolayer-covered gold sample at 380 K, the ordered structure vanishes. The previously unordered, elongated islands become ordered, as shown in Fig. 52. This ordering is, however, not extended over long distances, but exists only very locally. The structure observed after annealing perturbs the herringbone reconstruction, as seen in Fig. 52a, where the regular herringbone reconstruction lines, imaged by STM as bright lines, are bent in the vicinity of the island. In Fig. 52b, a high-resolution image of a characteristic molecular structure within such an island is presented. Parallelograms assembled by four bright features can be recognised, and the distance of the entities within the structure (~ 5 Å) is comparable with that found in the previously observed ordered structure. These parallelograms are aligned side by side, and an additional row of dimmer entities is found attached to it. Although, this type of pattern is characteristic for the islands, it is important to note that a multitude of slight modifications was observed.

6.4 Increasing coverage

Upon increasing coverage at room temperature, cysteine forms close-packed hexagonal overlayers as shown in Fig. 53. Locally, a (2×2) structure can be identified in Fig. 53a in the upper part of the image, but slight perturbations of this structure are frequently observed, as exemplified in the lower part of the STM image, and the (2×2) pattern is thus not well developed on a large

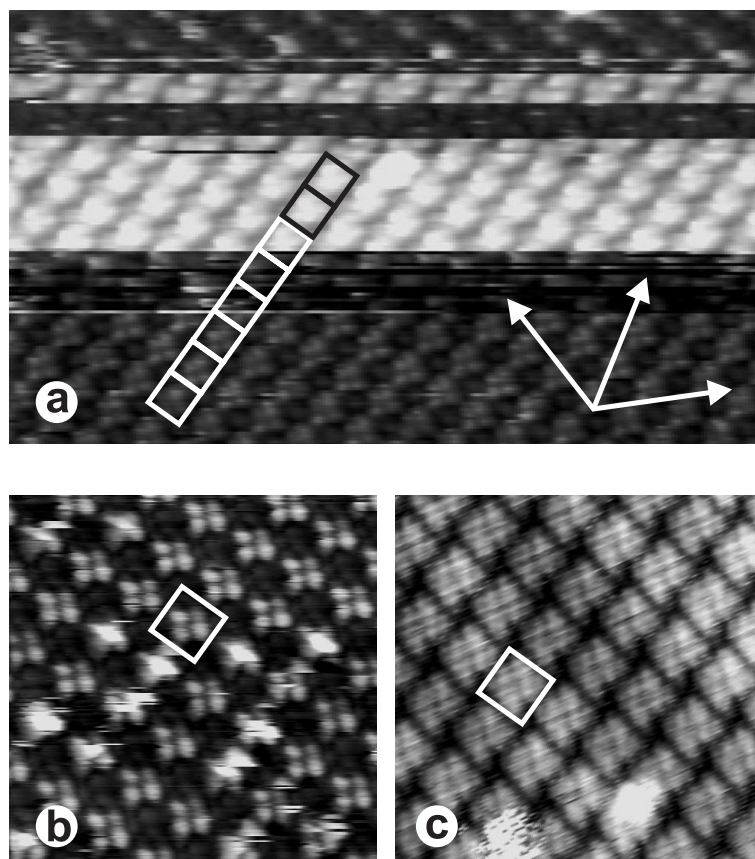


Figure 51: Zoom-in on the ordered structure obtained after evaporation of cysteine onto Au(111) held at room temperature.

(a) Image recorded with a changing tip, demonstrating two different imaging modes for the ordered overlayer. Image size: $200 \text{ \AA} \times 115 \text{ \AA}$. (b) High-resolution image of the overlayer as imaged in the lower part in panel (a). A rectangular unit cell with $d = 12 \text{ \AA}$ is marked in the image. Image size: $70 \text{ \AA} \times 70 \text{ \AA}$. (c) High-resolution image of the overlayer recorded with a different tip state. Same image size.

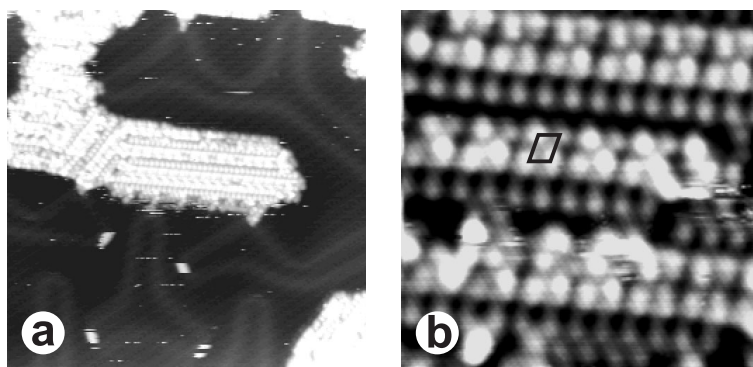


Figure 52: STM images showing the internal structure of the cysteine islands after annealing the sample to 380 K.

- (a) Cysteine island with a perturbed surrounding herringbone reconstruction.
 Image size: $500 \text{ \AA} \times 500 \text{ \AA}$. (b) Zoom-in on a characteristic region of the islands.
 Image size: $100 \text{ \AA} \times 100 \text{ \AA}$.

scale. In some areas, several cysteine molecules are apparently missing in the close-packed overlayer, leading to dark rows with a characteristic “zig-zag” appearance in the STM images. This phenomenon is presented in the STM image in Fig. 53b.

After annealing the high-coverage structures at 380 K, the whole surface is covered with a $(\sqrt{3} \times \sqrt{3})R30^\circ$ structure, that is locally well developed, but with a tendency to form elongated regions (Fig. 54a). A high-resolution image is displayed in the inset, locally disclosing a hexagonal pattern consistent with a $(\sqrt{3} \times \sqrt{3})R30^\circ$ structure. Furthermore, about 2.4 \AA deep holes are observed within the molecular layer. The depth of the holes corresponds well with the step height of 2.35 \AA on Au(111), suggesting these holes to be monatomic holes in the gold surface, as frequently observed for alkanethiol films on Au(111) [46]. In Fig. 54b a hole within the film is depicted, disclosing the underlying bare gold surface with a monatomic deep hole in the centre. The bottom of this hole is covered by molecules in a $(\sqrt{3} \times \sqrt{3})R30^\circ$ arrangement. No indication could, however, be found for the $c(4 \times 2)$ superstructure on top of the $(\sqrt{3} \times \sqrt{3})R30^\circ$ structure, which has been reported before for alkanethiol SAMs on Au(111) [122, 198].

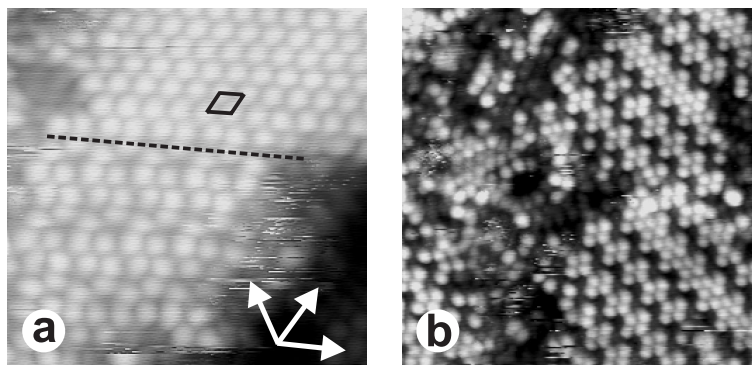


Figure 53: High-coverage structures at room temperature.

Ordered overlayers are shown, obtained after high-coverage evaporation of cysteine onto Au(111) held at room temperature. Areas of different structures are found, exhibiting several variations of a hexagonal pattern. Image sizes: $150 \text{ \AA} \times 150 \text{ \AA}$ (a) and $200 \text{ \AA} \times 200 \text{ \AA}$ (b).

6.5 Discussion

At low temperatures, the formation of unordered islands nucleating in the elbows of the herringbone reconstruction and growing from the step edges was disclosed. Depending on the coverage, several coexisting structures were observed at room temperature, including an ordered structure, which preserves the underneath herringbone reconstruction. This indicates that the cysteine molecules interact only weakly with the underlying substrate. In particular, a sulphur-gold bond formation, commonly observed for thiols on Au(111) and reported in many studies on cysteine on gold [136–138, 143], seems unlikely on the basis of this observation. Coexisting with this ordered layer, unordered islands were observed, which grow in size upon increasing exposure.

When annealing at 380 K, the observed ordered structure vanishes and local ordering is introduced in the previously unordered cysteine island. The surrounding herringbone reconstruction was found to be affected by the cysteine islands. This suggests that a transition from the physisorbed to the chemisorbed state may have taken place upon annealing, most likely involving a covalent sulphur-gold bonding.

Upon increasing coverage at room temperature, a (2×2) cysteine structure was found locally. This structure is, however, characterised by various pertur-

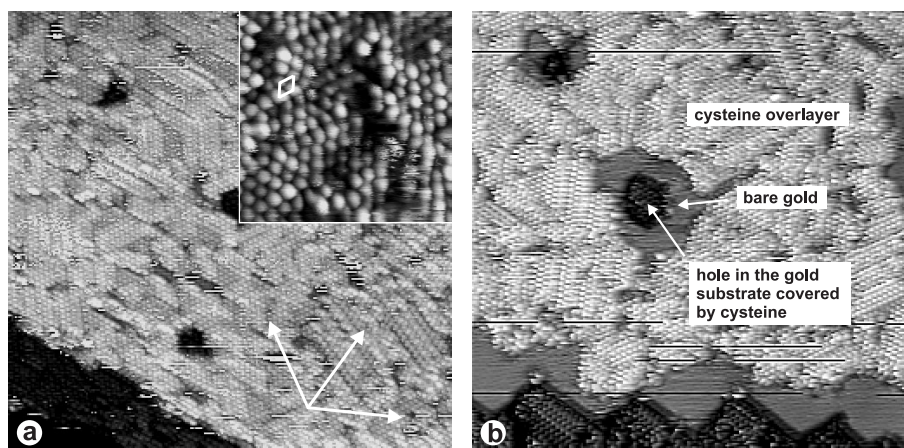


Figure 54: High-coverage structure after annealing.

(a) Upon annealing the high-coverage structure, a $(\sqrt{3} \times \sqrt{3})R30^\circ$ superstructure is formed locally. This overlayer is imperfect at a large scale and possesses holes of 2.4 Å depth. Image size: 500 Å × 500 Å. Inset: High-resolution image of the $(\sqrt{3} \times \sqrt{3})R30^\circ$ superstructure, demonstrating some local ordering. Image size: 100 Å × 100 Å. (c) Holes within the cysteine layer disclosing the bare gold surface with a monatomically deep hole covered by molecules. Image size: 500 Å × 500 Å.

bations and poor ordering on a larger scale. Annealing of these cysteine films leads to the formation of a $(\sqrt{3} \times \sqrt{3})R30^\circ$ structure, in agreement with the results presented previously for a cysteine layer deposited from solution [136]. This adlayer is only locally ordered and many monatomic holes are observed in the overlayer.

The variety of coexisting adsorption structures obtained upon cysteine deposition is remarkable. In contrast to the commonly reported observation of a strongly bound, chemisorbed $(\sqrt{3} \times \sqrt{3})R30^\circ$ thiolate layer on Au(111), cysteine apparently forms a multitude of different overlayers, which may be explained by different arrangements of the functional groups within the structures. The present study illustrates that coexisting molecular structures are quite common even for this small molecule.

Compared to the results on the Au(110) surface, the experiments on the less corrugated Au(111) surface revealed a larger influence of the molecule-molecule

interactions on the structure formation compared to the molecule-substrate interactions, since several overlayers are identified on Au(111) with no or only little dependence on the particular surface geometry. Especially the ordered overlayer observed at room temperature demonstrates the weak molecule-substrate interaction. In contrast to the situation on Au(110), the molecules appear to be physisorbed at room temperature, and the transition to the dehydrogenated cysteinate species occurs first after annealing the sample. This may be explained by the reduced reactivity of Au(111) compared to Au(110).

7 Dodecanethiol on Cu(110)

The adsorption of dodecanethiol ($\text{CH}_3(\text{CH}_2)_{11}\text{SH}$) films on Cu(110) by vapor deposition under UHV conditions was studied in cooperation with S. VOLLMER, G. WITTE and CH. WÖLL from the University of Bochum, Germany. The TPD, XPS and LEED experiments presented in this chapter were performed by S. VOLLMER.

This combined TPD, STM, XPS, and LEED study emphasises the structural changes accompanying the transition from a physisorbed monolayer to a chemisorbed saturation structure. Adsorption at 110 K leads to the formation of an ordered physisorbed layer with flat-lying thiol molecules. Upon room-temperature deposition, initially an ordered pin-stripe phase is formed which may be a molecular double layer. This layer transforms with time into a stable saturation structure of upright-tilted thiolates in a local $c(2 \times 2)$ arrangement that exhibits a long-range $c(12 \times 16)$ modulation, attributed to a moiré pattern. The XPS measurements show that the room-temperature saturation structure contains a fraction of sulphide species formed by partial decomposition and desorption of alkyl chains. At 400 K, the thiolate monolayer desorbs dissociatively, eventually resulting in a $p(5 \times 2)$ sulphur structure.

7.1 Introduction

Ultrathin molecular films, or self-assembled monolayers (SAMs), have attracted considerable interest, not least because of their promising technical applications in versatile fields such as lubrication, corrosion protection, high-resolution lithography or bio-chemical surface functionalisation [98, 199].

To date, the main body of data has been collected for monolayers of alkanethiols ($\text{CH}_3(\text{CH}_2)_{n-1}\text{SH}$) on Au(111), partly because this system is considered to be prototypical for SAM formation, but also because such films are comparatively easy to prepare by immersion of a gold sample into a thiol solution [46, 104]. Using an alternative preparation method, vapor-phase deposition, it has proven

possible to trace the individual steps by which SAMs form in such systems, starting from mobile, physisorbed thiol molecules followed by dehydrogenation to chemisorbed thiolate species [102, 200, 201].

Whereas no lateral ordering has been observed for the physisorbed alkanethiol molecules, a highly ordered “pin-stripe” thiolate phase, formed from molecules adsorbed with their backbone nearly parallel to the surface, has been identified at low coverages. With increasing coverage several thiolate phases are formed, accompanied by a continuous molecular upright tilting until a homogeneous and well-ordered, close-packed thiolate saturation phase is formed [202]. This transition can be reversed by partial desorption from the saturated monolayer [47, 103, 203, 204].

Compared to the case of gold, significant differences have been observed for alkanethiol films on other transition metals such as copper [205]. For example, an adsorption-induced reconstruction has been found for the Cu(111) surface [206], and a coexistence of thiolate and sulphide species has been identified in the saturated monolayer on Cu(100) [207]. Such observations demonstrate the need to extend the existing database on the ordering mechanisms and properties of thiolate monolayers to a larger range of substrates.

The current picture of the formation of alkanethiol SAMs on copper surfaces follows that for gold with some deviations. From He atom scattering, physisorbed alkanethiol molecules have been shown to lie flat on copper surfaces, but no lateral ordering has been observed for these films [208]. No ordered low-coverage thiolate phase with molecules lying prone on the surface has hitherto been observed on copper neither. An ordered phase where the molecules stand upright with tilt angles between 12° and 25° , almost independently of the molecular chain length ($n=6-16$), has been identified from *near edge X-ray absorption fine structure* (NEXAFS) measurements on various low Miller-index copper surfaces [209–213]. Annealing of such monolayers causes molecular dissociation with the sulphur remaining at the surface.

In this study, the adsorption of dodecanethiol ($n=12$) on a Cu(110) surface is reported, using TPD, variable temperature STM, XPS, and LEED. The main focus of the present study is on the structural changes that accompany the transition from an initially physisorbed layer to a close-packed layer of dehydrogenated thiolate molecules. The study of this transition has, in part, been enabled by the appropriate choice of an alkyl chain length for the alkanethiol molecule: Since the molecular physisorption energy increases with the chain length [102] which is reflected by the temperatures for desorption and transition from physisorbed to chemisorbed states, the transition rate at room temperature is reduced for longer thiols and thus allows a detailed study of the intermediate phases. Previous structural studies were not suited for the investigation

of the physisorbed phase and the subsequent transition since they were performed at room temperature and with short alkanethiols ($n < 8$) [206, 214–216]. The main results from the present multi-technique investigation can be summarised as follows. At the lowest temperature investigated, 110 K, an ordered layer of physisorbed molecules is found, lying flat on the surface. At room temperature, a transition from a physisorbed to a chemisorbed state occurs. Two transient “pin-stripe” structures are observed which can be designated by $\begin{pmatrix} 8 & -2 \\ 1 & 1 \end{pmatrix}$ and $c(2 \times 8)$ unit cells, respectively. Interestingly, indications exist that the former structure is a molecular double layer on top of the $c(2 \times 8)$ structure. Still at room temperature, these transient structures convert with time into a structure where the molecules are standing up, locally with an approximate $c(2 \times 2)$ arrangement, but exhibiting a long-range moiré modulation resulting in a $c(12 \times 16)$ unit cell. Within a few hours, or by briefly heating to 345 K, a partial dissociation of the molecules of this saturated thiolate film is observed, leading to the coexistence of chemisorbed sulphide and thiolate, while maintaining the $c(12 \times 16)$ moiré pattern. Upon annealing above 400 K, dodecanethiol desorbs dissociatively, resulting in a $p(5 \times 2)$ sulphur structure. The STM images were typically recorded with a bias of -1.25 V applied to the sample and a tunnelling current of ~ 0.6 nA. These parameters were found to be non-destructive since an influence from the scanning process on the thiol film was only observed if the tunnelling current was increased to about 4 nA.

7.2 TPD results

To survey the adsorption states of dodecanethiol on Cu(110), first the results from TPD measurements are described. Because of a high fragmentation probability of dodecanethiol upon ionisation in the mass spectrometer, TPD spectra were recorded simultaneously for the mass of the entire molecule ($m = 202$) and the C_3H_5 -fragment ($m = 41$) which was found to be the most probable fragment in the dodecanethiol gas-phase mass spectrum. Figure 55a shows a typical TPD spectrum obtained after exposing the Cu(110) surface to 200 L dodecanethiol ($1 \text{ L} \equiv 1 \times 10^{-6} \text{ torr}\cdot\text{s}$) at a sample temperature of 170 K. Three different desorption peaks are observed at temperatures of 242, 362 and 392 K, respectively. Whereas the low-temperature peak could be measured for the mass of the entire molecule and the C_3H_5 -fragment, the other two peaks appeared only for the fragment. A similar result has been observed previously for the desorption of heptanethiol from Cu(110) [213] as well as for various alkanethiols on Cu(100) [207]. In analogy to these studies, the lower temperature peak is attributed to multilayer desorption while the other desorption peaks reflect the dissociative desorption of alkyl chains upon sulphur-carbon

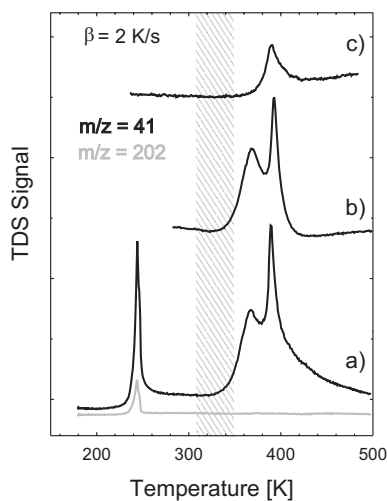


Figure 55: Thermal desorption spectra for dodecanethiol on Cu(110).

Series of TPD spectra for dodecanethiol adsorbed on Cu(110) recorded for the mass of the molecule ion ($m/z = 202$; grey line) and of the most prominent fragment C_3H_5 ($m/z = 41$; black line), at a heating rate of $\beta = 2$ K/s (a) for a multilayer film after exposure of 200 L at 170 K, (b) for a saturated monolayer (250 L) prepared at room temperature and (c) a saturated monolayer after additional annealing at 345 K for 10 min. The shaded region around 340 K indicates the desorption temperature of physisorbed dodecanethiol estimated from an extrapolation of the corresponding desorption temperatures of shorter alkanethiols (see discussion section). Spectra courtesy of S. VOLLMER.

bond breaking, which is characteristic for alkanethiolate films on copper surfaces [207, 213]. The presence of a double peak is tentatively attributed to two slightly different adsorption geometries for the thiolates.

Activation energies of 63 kJ/mol for desorption, and 95 kJ/mol and 103 kJ/mol for dissociation, respectively, were calculated from the temperatures of the corresponding desorption peak maxima by applying the Redhead formula [64] with a typical pre-exponential factor of 10^{13} s^{-1} (see equation 10).

To enable comparison with the STM data presented below, TPD spectra were measured for two other adsorption conditions. First, TPD spectra were recorded directly after saturating the surface with thiols at room temperature

(Fig. 55b), in which case the same high-temperature desorption doublet is observed. Second, TPD spectra were recorded after annealing such a saturated monolayer for 10 min at 345 K. As shown in Fig. 55c, this leads to a quenching of the lower temperature peak of the doublet, while the desorption peak at 392 K remains.

7.3 STM results

7.3.1 Low-temperature deposition

Upon deposition of dodecanethiol at 110 K, an ordered overlayer is formed, as shown in the STM image in Fig. 56a. The overlayer structure consists of elongated features approximately 6 Å wide and 17 Å long, stacked in parallel to form rows. The size of these molecular features agrees well with the length of a dodecanethiol molecule (15.2 Å), suggesting that the molecules are adsorbed parallel to the surface. Comparing STM images of this thiol structure to images of the bare surface, it is found that the main axis of the molecules is rotated by $\pm 6^\circ$ with respect to the $[1\bar{1}0]$ direction of the substrate. The rotation leads to two mirror domains as indicated by the grids superimposed in the STM image (see Fig. 56a).

The existence of ordered domains implies that individual molecules are mobile at 110 K. They diffuse on the surface until they are incorporated into the close-packed domains and become immobile. This picture is supported by the STM finding that the ordered domains have fuzzy edges, which is ascribed to molecules attaching and detaching in equilibrium with a surrounding lattice-gas phase.

7.3.2 Room-temperature deposition

Next, results obtained by depositing and imaging the molecules at room temperature are presented. Upon gradually increasing the exposure, clear evidence for adsorbed dodecanethiol was not observed until the surface was completely covered by an unordered molecular layer. This layer developed within few minutes into the ordered structures discussed below. The failure to observe dodecanethiol at submonolayer coverage is attributed to a high molecular mobility on the unsaturated surface at room temperature. This is further supported by the finding that the STM images recorded at low coverage show a high degree of noise and streakiness. Figure 56b shows a large-scale STM image of the dodecanethiol monolayer after room-temperature saturation. Two coexisting structures (denoted α and β) can be identified, with the α phase existing as two reflection domains, α_1 and α_2 . A high-resolution STM image of the α_2

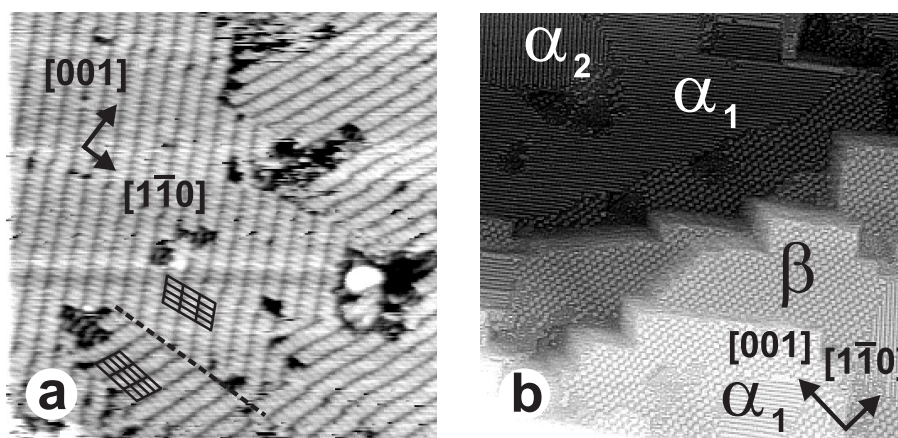


Figure 56: Dodecanethiol on Cu(110) at 110 K and at room temperature.

(a) STM image ($283 \text{ \AA} \times 274 \text{ \AA}$) recorded at 110 K after dodecanethiol adsorption at 110 K. Two reflection domains of an ordered overlayer (marked by grinds) are seen. (b) STM overview ($1830 \text{ \AA} \times 1770 \text{ \AA}$) recorded at room temperature after dodecanethiol deposition at room temperature showing the coexistence of the transient α structure with two reflection domains (α_1 , α_2) and the β structure.

structure is depicted in Fig. 57a. The structure consists of elongated entities arranged in rows to give the characteristic striped appearance seen in Fig. 56b. The periodic length along/perpendicular to the stripes amounts to 4.4 \AA and 21.6 \AA , respectively, and the stripes are oriented at angles of $\pm 55^\circ$ with respect to the $[1\bar{1}0]$ direction for the two reflection domains. In matrix notation, the α phase can be described by the $\begin{pmatrix} \pm 8 & -2 \\ \pm 1 & 1 \end{pmatrix}$ unit cell shown in Fig. 57a. A height profile of the α structure is shown in Fig. 57e, disclosing a corrugation of about 0.9 \AA . The STM images do not allow an unambiguous determination of the detailed molecular arrangement within this layer. To relate the structure of the α phase to the size of the dodecanethiol molecules, however, a possible molecular adsorption geometry, consisting of molecules adsorbed parallel to the surface with their sulphur atoms at the bright terminations of the elongated features, is indicated in Fig. 57a. At some places, features were observed, which appear to be holes in the α film, as indicated by the arrow in Fig. 57b. As can be seen in the height profile depicted in Fig. 57f, these holes have a depth of about

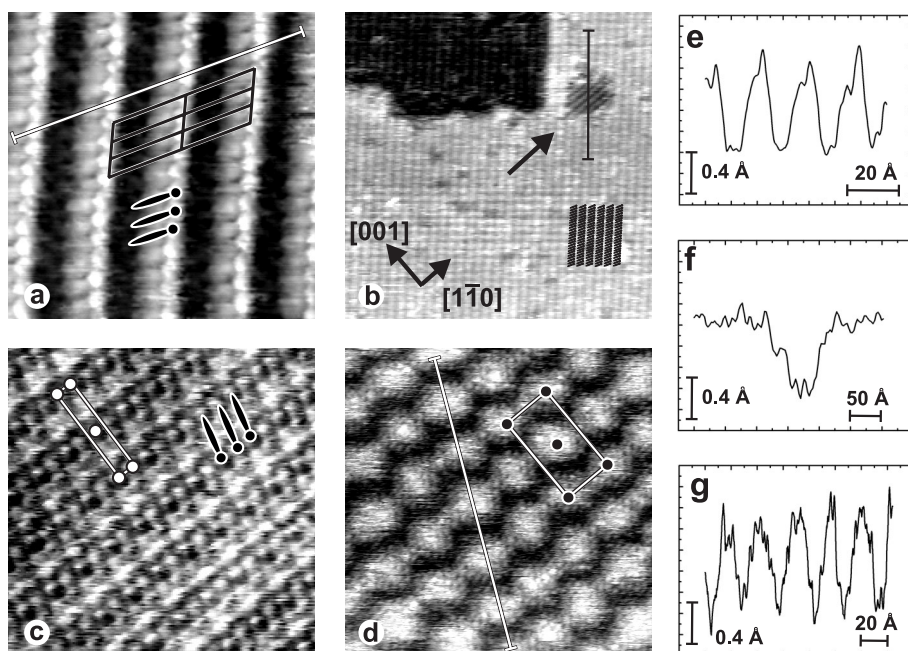


Figure 57: High-resolution STM images of dodecanethiol structures at room temperature.

(a) Image ($85 \text{ \AA} \times 83 \text{ \AA}$) showing one reflection domain of the transient α structure. A tentative structure suggestion is given by sketched lying-down molecules. (b) Image ($637 \text{ \AA} \times 616 \text{ \AA}$) showing a hole in the α structure with the underlying γ structure. (c) Zoom-in on the γ structure ($122 \text{ \AA} \times 118 \text{ \AA}$). One unit cell is indicated corresponding to a $c(2 \times 8)$ structure. (d) β structure exhibiting a $c(2 \times 2)$ structure with a $c(12 \times 16)$ moiré pattern. A $c(12 \times 16)$ unit cell is marked ($187 \text{ \AA} \times 177 \text{ \AA}$). (e-f) Height profiles of the lines marked in the images (a), (b) and (d).

0.7 \AA . The structure found at the bottom of the holes, denoted γ , is depicted at high resolution in Fig. 57c. The γ structure exhibits periodicities of 5.1 \AA and 28.9 \AA along the $[1\bar{1}0]$ and $[001]$ directions, respectively, corresponding to a $c(2 \times 8)$ unit cell as shown. A tentative explanation for the molecular adsorption geometry in the γ structure is superposed on the STM image in Fig. 57c.

The observation of the γ structure suggests the interesting possibility that the α phase described above may be a molecular double layer.

A zoom-in on the β structure is shown in Fig. 57d. This structure exhibits a characteristic long-wavelength modulation with a corrugation amplitude of approximately 1.1 Å, as can be seen in the line scan in Fig. 57g. The centre-to-centre distances between the protrusions of this long-range pattern are 31 Å and 58 Å along the $[1\bar{1}0]$ and $[001]$ directions, respectively, corresponding to a $c(12 \times 16)$ structure (indicated in Fig. 57d). By zooming further in on this β structure, a molecular-level fine structure is revealed which appears to be consistent with a local $c(2 \times 2)$ arrangement of the adsorbed species (a comparatively high noise level in these images prevents direct, unequivocal identification of long-range $c(2 \times 2)$ order in this layer). The β structure is attributed to molecules in an upright geometry and, as will be discussed in more detail below, the $c(12 \times 16)$ modulation is ascribed to a moiré pattern resulting from a mismatch between the overlayer of the approximate $c(2 \times 2)$ structure and the underlying substrate.

To directly investigate the evolution over time of the molecular overlayer structures, series of consecutive STM images were acquired of the same area on the surface (STM movies). By following the area depicted in Fig. 56b for 130 minutes at room temperature it was found that the two reflection domains of the α structure convert reversibly into each other. More interestingly, both α structures could be seen to convert into the β structure. This eventually resulted in the β phase covering the entire surface after about two hours, demonstrating that this phase is the energetically most favourable. It is noteworthy, however, that the reverse β to α conversion was also observed occasionally at the boundaries between these phases, demonstrating a local reversibility of the phase transition.

If the saturated monolayer formed at room temperature is annealed at 345 K for 10 minutes, a β' structure shown in Fig. 58 is formed. This structure differs only slightly from the β structure observed at room temperature and still reveals the long-range order associated with the $c(12 \times 16)$ moiré pattern. A probable reason for the different appearance of the two structures may be the onset of a partial dissociative desorption, as evidenced by the above-mentioned TPD results and the XPS measurements discussed in the following.

When the molecular film is annealed above 420 K, the molecules desorb dissociatively resulting in a $p(5 \times 2)$ sulphur structure as also observed by other authors [217].

Finally, it is noted that the evaporation of dodecanethiol at room temperature introduces step-faceting, changing the steps of the clean Cu(110) surface into the rectangular step features noticeable in Fig. 56b. This effect becomes even

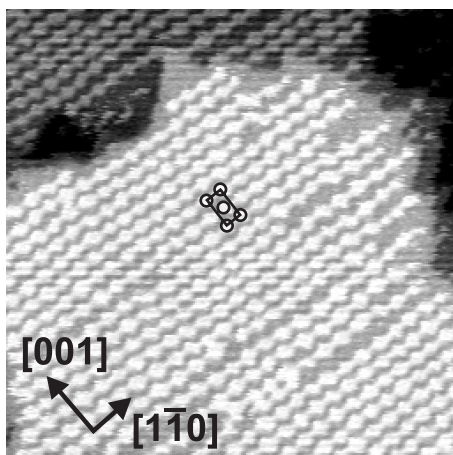


Figure 58: Saturation dodecanethiol structure after annealing at 345 K.

STM image of the saturation structure ($845 \text{ \AA} \times 826 \text{ \AA}$) after annealing the β phase at 345 K for 10 min, resulting in a slightly modified β' structure.

more pronounced when the β structure is fully developed. This step faceting evidences a substantial mobility of the substrate atoms at room temperature and/or possible adsorbate-mediated substrate modifications.

7.4 XPS results

To identify and characterise the different chemical adsorption states, variable-temperature XPS measurements were carried out. Fig. 59 shows a comparison of S 2p and C 1s XP spectra for dodecanethiol films on the Cu(110) surface taken after an exposure of about 10 L at 110 K and after saturating the surface at 300 K and 350 K, respectively. All spectra have been referenced to a Cu 2p_{3/2} line energy of 932.4 eV [218]. To determine the exact peak positions, the S 2p doublets were fitted by two gaussian curves with a fixed intensity ratio of $I_{3/2}/I_{1/2} = 2$ and a fixed energy separation of 1.3 eV. While the position of the carbon peak remains almost constant at 285 eV, a temperature-dependent shift of the S 2p_{3/2} binding energy was observed. A fit to the room-temperature data yielded a S 2p_{3/2} binding energy of $E_B=162$ eV. By comparison, the sulphur peak observed for the low-temperature preparation is substantially broader and can be decomposed into two S 2p doublets with S 2p_{3/2} binding

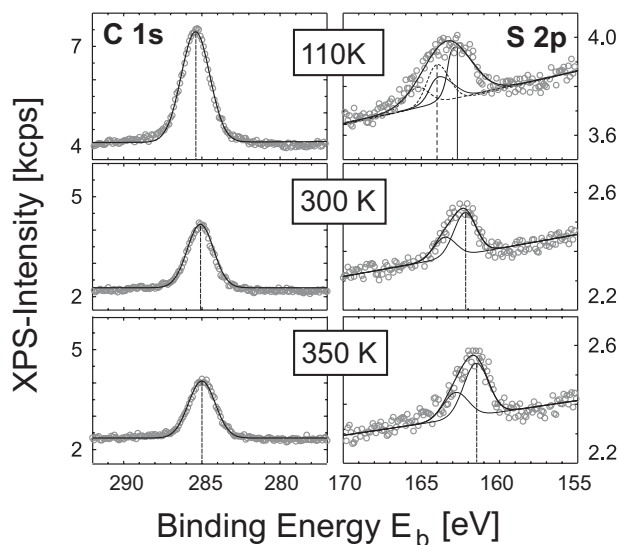


Figure 59: XP spectra for dodecanethiol films.

Series of XP spectra of the S $2p_{3/2}$ and C $1s$ peaks for dodecanethiol films prepared at 110 K (about 10 L) and for saturation dosage (200 L) at 300 K and 350 K. The data (grey circles) have been fitted by a set of one and two gaussian curves for carbon and sulphur, respectively. The two sulphur doublets at low temperature can be attributed to a physisorbed monolayer (solid line) and thiol multilayers (dashed line). Spectra courtesy of S. VOLLMER.

energies of 162.8 and 164.0 eV. A very similar result has been observed recently in a high-resolution XPS study of the adsorption of butanethiol on Cu(110) by employing synchrotron radiation. In that study, a physisorbed thiol monolayer and thiol multilayers could clearly be distinguished, and corresponding S $2p_{3/2}$ binding energies of 162.6 eV and 164.0 eV have been determined. The present low-temperature measurements thus indicate a coexistence of a physisorbed monolayer and a thiol multilayer. The reduction of the sulphur binding energy by about 1 eV when going to room temperature has been observed before also for other alkanethiols on copper surfaces and reflects the thiolate formation upon deprotonation of the sulphur headgroup [207, 213, 219].

The analysis of the corresponding peak intensities, determined by integration of the fitted Gaussians after a linear background subtraction, yielded a

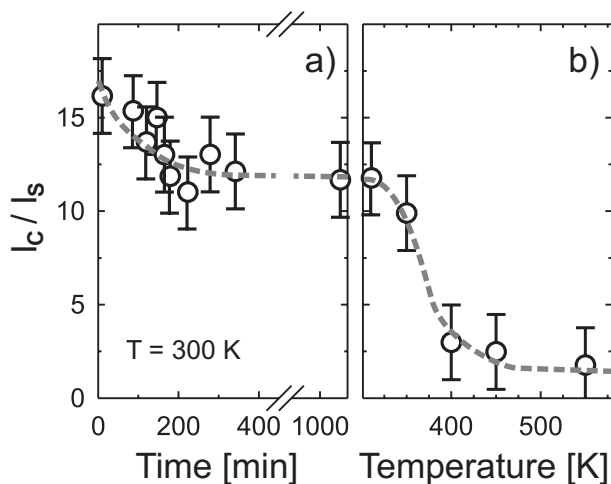


Figure 60: Evolution of the intensity ratio of the C 1s and S 2p_{3/2} XP peaks.

Evolution of the intensity ratio of the C 1s and S 2p_{3/2} XP peaks for dodecanethiol adsorbed at room temperature as a function of (a) time and (b) the subsequent annealing temperature. The data of panel (b) were all recorded at room temperature after the sample was held at the displayed annealing temperatures for 1 min. Data courtesy of S. VOLLMER.

C 1s/S 2p_{3/2} intensity ratio of 12.6 ± 1 for 110 K, while the ratio increases to 16.2 ± 1 for a film preparation at 300 K. This change is attributed to an enhanced attenuation of the electrons originating from the sulphur atoms through the upright tilted alkyl chains [209–211] of the saturated thiolate phase compared to the flat-lying, physisorbed alkanethiol molecules on copper [208]. By following the XPS intensities as a function of time, the changes in the saturated monolayer films could be followed. As shown in Fig. 60a, the C 1s/S 2p_{3/2} intensity ratio decreases from an initial value of 16.2 ± 1 after preparation to about 12 ± 1 within 200 min and subsequently remains constant at this level for a further 800 min. A similar reduction of the C 1s/S 2p_{3/2} intensity ratio was observed upon a brief annealing of the thiolate film to 350 K. Since the close packing of the saturated thiolate monolayer does not allow the molecules to tilt downwards again, this decrease in the ratio is explained by a partial degradation of the dodecanethiol film causing the carbon intensity to decrease while the sulphur coverage remains essentially constant. The alkyl-chain density is estimated to

be reduced by about 20-25% at room temperature after equilibration.

A similar change in intensities was observed previously for various alkanethiol films on Cu(100) [207], where it was shown that the partial deterioration was not caused by radiation-induced damage. To exclude radiation damage in the present experiment, the recording time for each XP spectrum was limited to about 10 min and the X-ray source was switched off between the different measurements.

It is noteworthy that a small shift of the sulphur S 2p_{3/2} binding energy to E_B=161.5 eV accompanies the decrease in the C 1s/S 2p_{3/2} intensity ratio upon annealing at 345 K (see Fig. 59). Unfortunately, the resolution in the present experiments was not sufficient to directly resolve the anticipated sulphide species in the XPS data. It is, however, noted that the presence of such a sulphide species has been clearly identified in a recent high-resolution XPS experiment using synchrotron radiation.

Upon additional annealing at elevated temperatures, a further decrease of the C 1s/S 2p_{3/2} intensity ratio was observed, as shown in Fig. 60b. The corresponding XP spectra were all recorded at room temperature after the sample was held at the indicated temperature for about 1 min. The intensity ratio starts to decrease already slightly above room temperature and vanishes almost completely after heating to 400 K. This reflects that at temperatures above 400 K, a complete dissociative desorption of all alkyl chains occurs with the sulphur remaining at the copper surface, in good agreement with the conclusions from the TPD and STM measurements.

7.5 LEED results

LEED measurements were carried out to further characterise the long-range ordering of the dodecanethiol films. To prevent possible electron beam damage to the film, all LEED measurements were performed with a microchannelplate LEED system operated with an incident electron beam current of typically 100 pA. In view of the soft external vibrational modes of thin organic films [208, 220], which lead to a strong DEBYE-WALLER attenuation of the diffraction peaks, the sample was cooled to a temperature below 120 K after preparation before recording the LEED pattern. Attempts to observe any diffraction pattern for a physisorbed dodecanethiol layer prepared by exposing the sample held at 120 K were not successful. Instead, only an enhanced diffuse background signal was obtained.

After saturating the Cu(110) surface with dodecanethiol at room temperature, rather broad diffraction peaks at $c(2 \times 2)$ positions were obtained accompanied by an enhanced diffuse background as displayed in Fig. 61a. Although, these

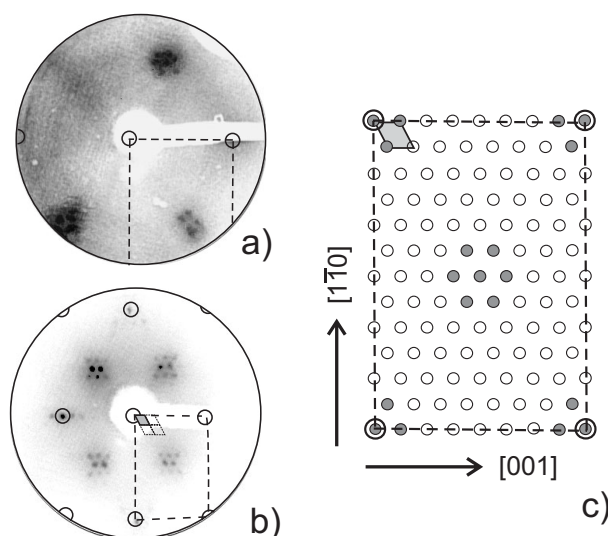


Figure 61: LEED pattern for a room-temperature saturation structure of dodecanethiol on the Cu(110).

(a) LEED pattern for a room-temperature saturation structure of dodecanethiol on the Cu(110) surface taken at an incident energy of 27 eV. For comparison a LEED pattern ($E_i = 73$ eV) for a saturated ethanethiolate monolayer on Cu(110) is displayed in (b). Both diffraction patterns were recorded at $T_S = 120$ K. For clarification the diffraction pattern of a $c(12 \times 16)$ structure is shown in panel (c) together with the unit cells of the superstructure (grey parallelogram) and the substrate (dashed rectangle). The visible diffraction spots (filled grey circles) are located near the $c(2 \times 2)$ positions. Images courtesy of S. VOLLMER.

spots clearly show an internal intensity modulation, analysis of the underlying superstructure is hampered by a weak contrast. Previous studies have shown that saturation thiolate structures on various copper surfaces do not depend on the chain length [206, 207, 214], while the contrast of the corresponding LEED patterns decreases with increasing chain length due to an attenuation of the diffraction intensity by the chains itself [207]. Inspired by these observations and to facilitate a more detailed structure analysis, additional LEED data were recorded for saturated monolayers of shorter alkanethiols with chain

length ranging from $n=2-7$ on the Cu(110) surface. Figure 61b displays the corresponding LEED pattern for ethanethiol, which has a structure identical to those obtained for the other chain lengths. A narrow mesh of diffraction spots is clearly observed, as depicted schematically in Fig. 61c, in agreement with a $c(12 \times 16)$ superstructure. Since diffraction spots were only observed near the $c(2 \times 2)$ positions, these data can be interpreted in terms of a moiré pattern consisting locally of a $c(2 \times 2)$ structure with a slight lattice mismatch forming the large $c(12 \times 16)$ unit cell as shown schematically in Fig. 61c. The LEED data for the ethanethiolate monolayer is thus consistent with the large-scale periodicity observed in the STM images for the saturated dodecanethiol layer. Returning to the LEED data for dodecanethiol, it is noted that no diffraction pattern was found corresponding to the intermediate pin-stripe phases observed in the STM measurements. After annealing the dodecanethiol film (as well as the films of the shorter alkanethiols) above 400 K, a sharp $p(5 \times 2)$ LEED pattern was observed, in agreement with the STM observation of such a sulphur structure [217].

7.6 Discussion

In the following discussion, the different observations from the present multi-technique study of the adsorption of dodecanethiol on Cu(110) will be interrelated and related to findings published in literature in order to form a coherent picture.

Adsorption of dodecanethiol at low temperatures (110 K) leads to the formation of a physisorbed layer with an ordered, pin-stripe structure exhibiting two reflection domains (see Fig. 56a). The STM data suggests an orientation of the molecules parallel to the surface which is corroborated by the C 1s/S 2p_{3/2} intensity ratio in the corresponding XPS measurements. The same molecular orientation has been derived from an analysis of the low-energy vibrational modes for heptanethiol physisorbed on Cu(110) [208].

It is interesting to compare this physisorbed phase with the monolayer structure adopted by saturated hydrocarbon chains on the same surface. For octane on Cu(110), a $p(5 \times 6)$ monolayer structure has been identified in which the alkane molecules are aligned with the close-packed $[1\bar{1}0]$ direction of the anisotropic surface. In the present low-temperature dodecanethiol film, the molecules are rotated by $\pm 6^\circ$ with respect to the close-packed direction, demonstrating the important influence of the endgroups on the resulting film structure.

The low-temperature physisorption structure could not be observed by LEED. This is attributed to the wide spread of diffraction spots due to the large unit cell size together with the domain structure and the small scattering cross sec-

tion of sulphur and carbon compared to the substrate which in combination result in weak diffraction spots (especially at out-of-phase conditions with respect to the substrate).

The observed shift of the XP S $2p_{3/2}$ peak binding energy from 163 eV at 110 K to 162 eV at room temperature indicates that a full or partial conversion from physisorbed molecules to thiolates has occurred at the latter temperature. The expected desorption temperature for physisorbed dodecanethiol molecules can be obtained from extrapolation of the corresponding desorption temperatures obtained for shorter alkanethiols. This is possible because the physisorption energy scales almost linearly with the chain length due to the molecular adsorption geometry parallel to the surface [102]. By this approach, the expected desorption temperature for physisorbed dodecanethiol is estimated to be 320 ± 10 K. This temperature band is indicated by the shaded region in Fig. 55, but does not coincide with any of the desorption peaks. In fact, the TPD signal for the mass of the entire molecule shows no spectral features above the multilayer desorption peak at about 240 K. In combination with the XPS results, this points to a complete conversion from dodecanethiol molecules to chemisorbed thiolate species during the thermal ramp of the desorption measurements. On the other hand, the chemical transition rate is reduced at room temperature, where typical conversion times of up to several hours were found from the time-lapsed XPS data of Fig. 60a. This allows the observation by room-temperature STM of several intermediate structures appearing during the formation of a saturated thiolate layer.

Upon evaporation of dodecanethiol at room temperature, an initial surface mobility was inferred from inabilities in STM imaging at submonolayer coverages. Again, this suggests that the individual molecules are initially adsorbed in a physisorbed precursor state, and only become observable with STM once the molecules form a continuous island or film.

The first ordered structure formed upon room-temperature deposition is the pin-stripe α phase with a $\begin{pmatrix} 8 & -2 \\ 1 & 1 \end{pmatrix}$ unit cell. With time, this structure converts into the β phase characterised by local approximate $c(2 \times 2)$ order and a long wavelength moiré modulation described by a $c(12 \times 16)$ unit cell.

It may seem tempting to equate the physisorption to chemisorption transition observed with XPS and TPD with the structural α to β phase transition observed by STM. Since a hydrogen atom is, however, lost upon dehydrogenation to form chemisorbed thiolate species, the local reversibility of this phase transition, as seen in the STM movies at the boundaries between the two phases, strongly suggests that the molecular species in both the α and β phases are in

the same, chemisorbed, state.¹²

The saturated monolayer of the β structure is thermally metastable. Already gentle annealing of the film at 345 K leads to a partial, dissociative desorption of the alkyl chains and causes a reduction of the film density. This is evidenced by the observed decrease in the C 1s/S 2p_{3/2} intensity ratio in the XPS data. Interestingly, the resulting β' structure has essentially the same structure as the β structure, as seen by STM. The time-lapsed XPS measurements shown in Fig. 60a indicate that a similar partial degradation of the film takes place at a time scale of several hours already at room temperature. The stable room-temperature saturation phase is thus demonstrated to comprise coexisting thiolate and sulphide species. Such an instability has been observed previously for the adsorption of alkanethiols of various chain lengths on Cu(100) [207] and thus seems to be quite general for the adsorption of thiolates on copper surfaces.

Heating the saturated film above 400 K causes a complete dissociative desorption of the alkyl chains, as observed by XPS and TPD, and leads to the formation of locally ordered domains of a p(5 × 2) sulphur structure identical to the one observed earlier upon deposition of sulphur on Cu(110) [217].

Now the β structure is discussed in further detail. In general, the formation of a moiré pattern can be explained by a coincidence mesh between two layers with a slight lattice mismatch. In the present case, this could be realised either by a periodic substrate relaxation or by a slight expansion/compression of the molecular overlayer away from a commensurate c(2 × 2) structure (as shown schematically in Figs. 62a and b, respectively). Although the appearance of surface stress upon chemisorption of molecules has been demonstrated [221], a stress-release pattern being the reason for a periodic substrate surface relaxation seems unlikely in the present case, since no evidence for such a modulation was found even for the stronger bound sulphur in the bare p(5 × 2) structure after thermal desorption of the alkyl chains. A primitive c(2 × 2) structure on the Cu(110) surface (i.e., with one molecule per unit cell) yields a molecular packing area of 18.4 Å² per molecule, very close to the molecular packing area of 18.6 Å² found in bulk alkanethiols. A closer inspection discloses, however, very anisotropic nearest-neighbour distances. While the molecules are separated by 5.1 Å along the [1 $\bar{1}$ 0] direction, the separation is only 4.4 Å along [1 $\bar{1}$ 1] compared to a spacing of 4.6 Å in a hexagonally close-packed configuration. A driving force for small relaxations in the c(2 × 2) structure could thus be a tendency of the alkane chains to maintain an *isotropic* intermolecular packing

¹²Rehydrogenation of the molecules in the β phase to allow a transition from chemisorbed to physisorbed molecules seems unlikely as the strong sulphur–copper interaction does not favour reformation of the comparatively weak sulphur–hydrogen bond.

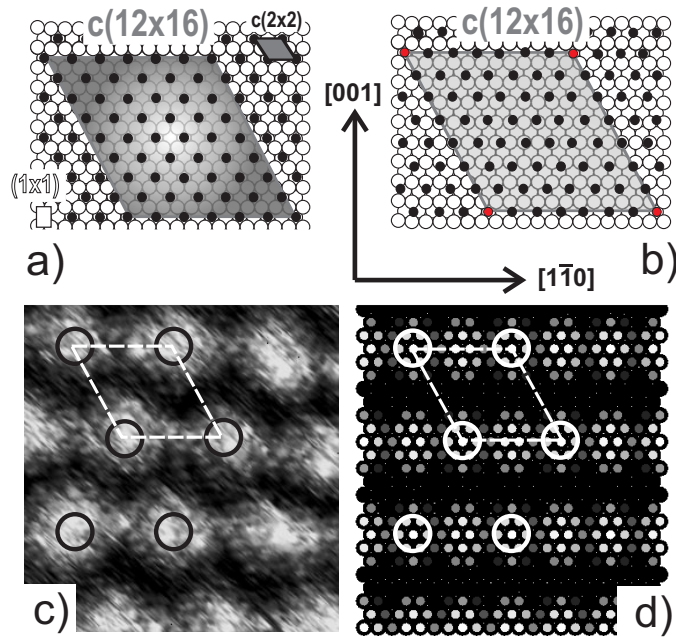


Figure 62: Origin of the observed moiré pattern.

Panels (a) and (b) illustrate two possible reasons for the appearance of the $c(12 \times 16)$ moiré pattern. (a) A $c(2 \times 2)$ phase with an additional modulation of the substrate (large parallelogram) due to a stress release pattern and (b) an anisotropically relaxed $c(2 \times 2)$ overlayer (the overlayer is compressed in the $[1\bar{1}0]$ direction to place seven molecules over 12 copper atoms and expanded in the $[001]$ direction to place seven molecules over 16 copper atoms). (c) STM image showing the moiré pattern observed at room temperature. (d) Simulated moiré pattern resulting from a simple hardball stacking model of structure (b). This modification results in an almost hexagonal overlayer with (12×16) periodicity.

distance close to the bulk value. Using a simple hardball stacking model, the coincidence meshes for a large variety of modified $c(2 \times 2)$ overlayers have been explored on an unperturbed (110) substrate, resulting in moiré periodicities with, or close to, the experimentally observed $c(12 \times 16)$ unit cell. The best agreement with the STM data is found for the model displayed in Fig. 62b, obtained by anisotropic relaxation of a $c(2 \times 2)$ overlayer involving a 14% com-

pression in the $[1\bar{1}0]$ direction and a 14% expansion in the $[001]$ direction. These relaxations yield an almost hexagonal overlayer with a molecular packing area of 18.0 \AA^2 . This model clearly reproduces the protrusions (Fig. 62d) indicated in the STM image (Fig. 62c), but in addition exhibits a number of slightly smaller protrusions along the $[1\bar{1}0]$ direction. These additional protrusions in the model are not seen in the STM image, but interconnections seem to exist between the experimentally observed protrusions along the $[1\bar{1}0]$ direction, whereas no interconnections are present for other high-symmetry directions in the STM image. These interconnections are even more pronounced after annealing, as shown in Fig. 58. The lack of complete agreement between the STM image and a simple hardball stacking model on an unperturbed substrate suggests that the observed moiré pattern may result from a more complicated mechanism, perhaps also involving a lateral relaxation of the copper substrate, similar to that observed for a sulphate-covered Cu(111) surface [222].

No evidence of a pronounced reconstruction of the Cu(110) substrate underneath the dodecanethiol layer was found in the present STM and LEED data. This is in contrast to the complete rearrangement of the top layer that has been observed following the adsorption of thiols on Cu(111) [206,214]. The reconstruction on Cu(111) has been attributed to the tendency of sulphur atoms to occupy fourfold coordinated sites. The observed stability of the rather open Cu(110) surface is likely to be explained by the availability of such specific adsorption sites in combination with the close agreement between the molecular packing area in the β structure and in bulk alkanethiols. While the surface terraces do not appear to reconstruct, it should be noted that significant step faceting occurred upon formation of the saturation structure, as seen from Fig. 56b.

As mentioned earlier, indications exist that the α phase is a molecular bilayer. First, high-resolution STM images, like the one shown in Fig. 57b, directly reveal features which appear to be holes within the α phase, exhibiting a $c(2 \times 8)$ superstructure (γ phase). Second, the existence of a bilayer is corroborated by the consideration of the molecular densities of the different structures. The area per molecule in the α and γ phases are 92.1 \AA^2 and 73.6 \AA^2 , respectively, if one/two dodecanethiol molecules for each $\begin{pmatrix} \pm 8 & -2 \\ \pm 1 & 1 \end{pmatrix} / c(2 \times 8)$ unit cell is assumed, as seems reasonable from the dimensions of the dodecanethiol molecules tentatively superposed on the corresponding STM images. The $c(2 \times 2)$ saturation structure has a considerably higher molecular packing density with one upright molecule per 18.4 \AA^2 . The observed local reversibility of the α to β phase transition can only be facilitated when extensive mass transport is not required. Although the combined density of the α and γ structures do still not fully suffice to provide the molecular density in the β structure, these considerations

support the conclusion that the α phase is a molecular double layer.

7.7 Conclusion

The adsorption of dodecanethiol on a Cu(110) surface was studied by STM, LEED, XPS, and TPD with particular emphasis on the transient structures that appear upon formation of a saturated thiolate monolayer.

At the lowest temperature of 110 K, an ordered layer of physisorbed molecules is observed. By choosing a fairly long-chained alkanethiol, the physisorption energy becomes so large that the transition into chemisorbed species, i.e., thiolate formation, sets in before the desorption of the physisorbed species occurs. This allows a number of intermediate adsorption structures to be observed at room temperature. Two intermediate pin-stripe structures are observed and indications exist that they are both part of a molecular double layer. These structures transform into an approximate $c(2 \times 2)$ saturation phase. This close-packed structure exhibits a long-range $c(12 \times 16)$ modulation. The saturated thiolate film is thermally metastable since the partial dissociative desorption of about 25% of the alkyl chains was observed after several hours. The resulting saturation structure consists of coexisting thiolate and sulphide species. Heating the saturated film above 400 K causes a complete desorption of the alkyl chains, resulting in a $p(5 \times 2)$ sulphur structure.

8 German summary

Die vorliegende Arbeit befaßt sich mit der Adsorption von organischen und insbesondere biologisch relevanten Molekülen auf verschiedenen Metalloberflächen im Ultrahochvakuum (UHV). Die vorwiegend eingesetzte experimentelle Technik ist die Rastertunnelmikroskopie (*scanning tunnelling microscopy* (STM)), die es erlaubt, einzelne Atome und Moleküle auf einer metallischen Oberfläche abzubilden. Ziel der Untersuchung ist ein tieferes Verständnis der intermolekularen Wechselwirkungen sowie der Wechselwirkungen zwischen den Molekülen und der Oberfläche. Diese Wechselwirkungen, COULOMB-Anziehung, VAN-DEER-WAALS Wechselwirkung, Ausbildung von Wasserstoffbrückenbindungen bis hin zu kovalenten Bindungen, bestimmen die Struktur, d.h. Ordnung und Orientierung der Moleküle auf der Oberfläche. Durch eine geeignete Wahl von Molekülen verschiedener Größe mit verschiedenen funktionellen Gruppen und durch die Variation von Oberflächeneigenschaften können die relativen Einflüsse der wirkenden Kräfte variiert und letztendlich zur Herstellung definierter Strukturen gezielt eingesetzt werden.

Eine vielversprechende Strategie zur schnellen und ökonomischen Herstellung von geordneten Nanostrukturen mit definierten Eigenschaften ist die Ausnutzung von Selbstorganisation, *self-assembly*. Diese spontane, reversible Anordnung von Molekülen zu größeren, funktionalen Einheiten ist allgegenwärtig in der belebten Natur, zum Beispiel bei der Entstehung eines so komplexen, dreidimensionalen Gebildes wie eines Proteins aus einer linearen Kette von Aminosäuren. Das Verständnis der Prozesse, die diese Selbstorganisation steuern, ist nicht nur notwendig für die Anwendung von *self-assembly* in der Nanotechnologie, es ist auch eine Voraussetzung, zentrale Prozesse der belebten Natur zu verstehen.

Im Rahmen dieser Arbeit wurde die Adsorption zweier Moleküle, Dodecanthiol und Cystein, auf Kupfer beziehungsweise auf Gold untersucht. Dodecanthiol gehört zur Gruppe der Alkanthiole, die aufgrund der starken Wechselwirkung

von Schwefel mit Goldoberflächen im Zusammenhang mit sogenannten *self-assembled monolayers* (SAMs) intensiv untersucht wurden und inzwischen zum Paradebeispiel für self-assembly wurden. Alkanthiolstrukturen auf Kupfer dagegen wurden bisher nur wenig untersucht, und das vergleichende Studium der sich bildenden Moleküllagen erlaubt Rückschlüsse auf den Einfluß der Substratoberfläche auf die Strukturbildung. In dieser Arbeit wurden der temperaturabhängige Übergang von einer physisorbierten Dodecanthiollage zu chemisorbiertem Dodecanthiol und die damit verbundene Veränderung der Molekülstrukturen auf der Oberfläche untersucht. Neben Aufnahmen mit dem Rastertunnelmikroskop wurden in Zusammenarbeit mit S. Vollmer, G. Witte und Ch. Wöll von der Ruhr-Universität Bochum auch Röntgen-Photoelektronenspektroskopie Experimente durchgeführt.

Der Schwerpunkt dieser Arbeit aber liegt auf Adsorptionsexperimenten von Cystein auf Gold. Cystein ist eine natürliche Aminosäure, d.h. es ist eine der zwanzig Aminosäuren, die unter anderem für den Menschen zum Aufbau der Proteine notwendig sind. Darüber hinaus ist Cystein die einzige natürliche Aminosäure, die eine Mercapto Gruppe (-SH) besitzt und damit gleichzeitig zu der bereits diskutierten Klasse der Thiole gehört. Der Einfluß der Oberfläche wurde durch Experimente auf zwei verschiedenen Kristallflächen, (111) und (110), untersucht. Während auf der relativ gering korrigierten Au(111) Oberfläche eine Vielzahl von leicht unterschiedlichen, geordneten wie auch ungeordneten Molekülstrukturen existiert, spielt im Falle von Au(110) aufgrund der rekonstruierten Oberfläche die deutlich ausgeprägtere Korrugation eine entscheidende Rolle für die Strukturbildung.

Abhängig von Temperatur und Bedeckungsgrad lassen sich auf Au(111) zahlreiche, leicht variierende Strukturen beobachten, die auf der Oberfläche koexistieren und auf die Wechselwirkung der drei funktionellen Gruppen von Cystein zurückzuführen sind. Auf der (110) Oberfläche dagegen bilden sich Strukturen, die auf der Wechselwirkung mit der Oberfläche basieren, wie zum Beispiel Cystein Dimere, deren Bildung nur durch die besondere Oberflächengeometrie mit der sogenannten *missing-row* Oberflächenrekonstruktion möglich ist. Die Experimente mit dem Rastertunnelmikroskop wurden durch Infrarotspektroskopie Messungen ergänzt, die in Zusammenarbeit mit Q. CHEN und N. V. RICHARDSON von der Universität St. Andrews, Großbritannien, durchgeführt wurden. Diese Messungen lieferten zusätzliche Informationen über die Bindungsverhältnisse von Cysteine auf Gold.

Experimente bei tiefen Temperaturen zeigten ein besonders markantes Beispiel der Selbstorganisation, nämlich die Bildung von Cystein Nanoclustern, welche, im Gegensatz zu sogenannten metallischen "*magic clusters*", keine Größenvariation aufweisen, sondern absolut identisch sind. Diese Uniformität ist in-

teressant, da die Eigenschaften von Quantenstrukturen untrennbar mit deren Dimensionen verknüpft sind.

Eine weitere, wichtige Eigenschaft von Cystein ist seine Chiralität. Chiralität, oder auch "Händigkeit", beschreibt die geometrische Eigenschaft eines Objekts, nicht mit seinem Spiegelbild kongruent zu sein. Chiralität ist von größter Bedeutung in der belebten Natur, da fundamentale chemische und biologische Prozesse von der Chiralität der beteiligten Moleküle abhängig sind. In der Molekularbiologie zentrale Makromoleküle sind häufig chiral, und ihre korrekte Wirkungsweise ist von ihrer Chiralität abhängig. Proteine zum Beispiel bestehen ausschließlich aus L Aminosäuren, während die Zuckermoleküle in der DNA ausschließlich D Konfiguration besitzen. Chirale Wiedererkennung, molekulare Wiedererkennung mit chiraler Spezifität, spielt eine zentrale Rolle in enzymatischen und anderen Ligand-Rezeptor Reaktionen, unter anderem auch für Medikamente, da verschiedene Enantiomere eines Medikaments unterschiedliche Wirkungen haben können. Ein alltägliches Beispiel chiraler Wiedererkennung ist der Geruch von Kümmel und grüner Minze, der, für uns deutlich unterscheidbar, von den zwei chiralen Konfigurationen eines ansonsten identischen Moleküls herrührt.

In dieser Arbeit wird ein Prozeß vorgestellt, der chirale Wiedererkennung auf molekularer Skala demonstriert. Bei der Dimerisierung von Cysteinmolekülen auf der Au(110) Oberfläche zeigt sich, daß sich ausschließlich homochirale Molekülpaare bilden, wenn beide Enantiomere gleichzeitig adsorbiert werden. B. HAMMER und L. MOLINA von der Universität Aarhus haben *density-functional theory* (DFT) Berechnungen zur Adsorption von Cysteine durchgeführt. In enger Zusammenarbeit zwischen Experiment und Theorie konnten die Hintergründe für die enantioselektive Paarbildung verstanden werden: Die Optimierung von drei Bindungen für jedes Cysteinmolekül in einem Paar ist für die beobachtete Enantioselektivität verantwortlich. Diese drei Bindungen sind gegeben durch eine kovalente Bindung des Schwefels zur Goldoberfläche, durch die Wechselwirkung der Aminogruppe mit der Oberfläche und durch die Bildung von Wasserstoffbrückenbindungen der Carboxylgruppe zur Carboxylgruppe des zweiten Cysteinmoleküls im Paar. Damit ist das vorgestellte System eine Illustration eines bekannten Modells für chirale Wiedererkennung, das sogenannte 3-Punkt-Kontakt-Modell. Dieses Modell, im Jahre 1933 von L. H. EASON und E. STEDMAN formuliert, beschreibt als geometrische Voraussetzung für chirale Wiedererkennung die Wechselwirkung eines chiralen Objekts (z. B. eines Liganden) mit einer Adsorptionsstelle (ein Rezeptor) an mindestens drei Kontaktpunkten. Nachdem Chiralität eine mit der räumlichen Morphologie, d.h. dreidimensionalen Ausdehnung verknüpfte Eigenschaft ist, leuchtet unmittelbar ein, daß die Chiralität eines Objekts mit der Definition von drei

Punkten eindeutig bestimmt ist. Die vorgestellten Experimente illustrieren dieses Modell anschaulich, indem jeder Kontaktpunkt einer Bindung im Cysteinpaaar zugeordnet werden kann. Damit ist ein Modellsystem vorgestellt, für welches die von L. H. EASSON und E. STEDMAN beschriebenen Kontaktpunkte erstmalig auf kleinster, d.h. molekularer Ebene bestimmt werden konnten.

9 Publications

9.1 List of publications related to this thesis

1. A. Kühnle, S. Vollmer, T. R. Linderoth, G. Witte, Ch. Wöll and F. Besenbacher, Adsorption of dodecanethiol on Cu(110): Structural ordering upon thiolate formation, *Langmuir* **18** (2002) 5558-5565
2. A. Kühnle, T. R. Linderoth, B. Hammer and F. Besenbacher, Chiral recognition in dimerization of adsorbed cysteine observed by scanning tunnelling microscopy, *Nature* **415** (2002) 891-893
3. A. Kühnle, T. R. Linderoth and F. Besenbacher, Self-assembly of supramolecular nanoclusters of cysteine on Au(110)-(1×2), in preparation
4. A. Kühnle, L. Molina, T. R. Linderoth, B. Hammer and F. Besenbacher, Adsorbate-induced surface restructuring as the driving mechanism for uni-directional molecular-chain growth, in preparation
5. A. Kühnle, T. R. Linderoth, B. Hammer and F. Besenbacher, Temperature dependent adsorption structures of cysteine on Au(110)-(1×2), in preparation
6. A. Kühnle, M. Schunack, T. R. Linderoth and F. Besenbacher, Cysteine overlayers on Au(111) investigated by UHV-STM, in preparation
7. A. Kühnle, T. R. Linderoth, B. Hammer and F. Besenbacher, Possible chiral symmetry breaking upon cysteine adsorption onto Au(110)-(1×2), in preparation

9.2 Other studies

Besides the studies discussed here, I have been involved in other projects that are not included in this thesis. One study was performed in collaboration with M. SCHUNACK and has concentrated on the investigation of a largish organic molecule, hexa-*tert*-buty-decacyclene ($C_{60}H_{66}$), on the (110) facet of copper with a low and variable-temperature STM [223]. This work revealed another interesting example of adsorbate-induced surface reconstruction, demonstrating that these large hydrocarbons are able to restructure the surface to improve the binding to the surface.

An obvious question in relation to the presented results regarding the cysteine dimerisation reported in section 4.3 is whether the molecular pairing is still observable after small perturbations in the molecular structure. To investigate the influence of a slightly modified molecular size, the adsorption of homocysteine ($HS-CH_2-CH_2-CH(NH_2)-COOH$) onto Au(110) has been investigated. Homocysteine resembles cysteine apart from an additional CH_2 group. Homocysteine forms different phases on Au(110), but no dimerisation is found as in the case of cysteine, illustrating the crucial role of the detailed adsorption geometry. In the view of the presented model for the cysteine adsorption, the choice of homocysteine may not have been the optimum, as the insertion of a CH_2 group not only leads to a change in molecule size, but also in the geometry due to the angle of $\sim 109^\circ$ introduced by the sp^3 hybridised carbon atom. A cysteine molecule with two additional CH_2 groups inserted ($HS-CH_2-CH_2-CH_2-CH(NH_2)-COOH$), would allow the angles between the functional groups to remain nearly unchanged. Such a molecule may be a more promising candidate for the formation of molecular dimers.

Preliminary cysteine adsorption experiments have been obtained on titanium dioxide. TiO_2 is an important material for the study of biomolecular adsorption as titanium is used in implants [43], and a detailed knowledge of the adsorption of amino acids is of interest for understanding complex processes such as cell adhesion and biocompatibility [8]. In this context, adsorption studies in a more natural environment are desired, and eventually one has to move towards *scanning force microscopy* (SFM) in liquids. I have been involved in testing different SFMs and performing preliminary liquid-phase protein adsorption experiments on different nanostructured surface that have been prepared in the group of B. KASEMO at Chalmers in Gothenburg, Sweden [224, 225].

10 List of abbreviations

In this thesis, the following abbreviations have been introduced:

AES	auger electron spectroscopy
DFT	density-functional theory
DNA	desoxyribonucleic acid
EMT	effective-medium theory
fcc	face-centred cubic
GGA	generalised gradient approximation
HAS	helium-atom scattering
hcp	hexagonally closed-packed
LDA	local density approximation
LDOS	local density of states
LEED	low-energy electron diffraction
NEXAFS	near edge X-ray absorption fine structure
RAIRS	reflection absorption infrared spectroscopy
RNA	ribonucleic acid
SAM	self-assembled monolayer
SFM	scanning force microscopy (or microscope)
STM	scanning tunnelling microscopy (or microscope)
TPD	temperature-programmed desorption
UHV	ultrahigh vacuum
XPS	X-ray photoelectron spectroscopy

11 Acknowledgements

The work presented in this thesis has been performed during my PhD study in the STM group at the Department of Physics and Astronomy of the University of Aarhus. This work has been financed by the Danish National Research Foundation through the Center for Atomic-scale Materials Physics (CAMP).

I am very grateful to my doctoral advisor Flemming Besenbacher for giving me the opportunity to join the group, which I really feel has been a great experience. I also would like to thank my co-supervisor Trolle Linderøth for his invaluable help and continuous support. This thesis has gained from the very close interplay between experiment and theory, and it is a pleasure to acknowledge Bjørk Hammer and Luis Molina for the fruitful cooperation regarding the cysteine adsorption on Au(110).

I would like to acknowledge all members of the research group for being a very friendly and collegial team and for their kind assistance whenever needed. I would like to express special thanks to Erik Lægsgaard for his technical assistance, to Michael Schunack who has been involved in the cysteine measurements on Au(111), and, of course, to Jeanette Dandanell who spell-checked all my abstracts and manuscripts, even the 38th version as well as for correcting the manuscript of this thesis. Anne-Louise Stranne, Peter Thostrup and Maria Dall Rasmussen are gratefully acknowledged for critically reading the draft version of the thesis. Fruitful collaboration and stimulating discussions with Qiao Chen, Neville Richardson, Stefan Vollmer, Gregor Witte and Christof Wöll are gratefully appreciated.

References

- [1] C. M. Niemeyer, Tools for the Biomolecular Engineer, *Science* **297**, 62 (2002).
- [2] A. D. Hamilton, Much binding in the lab, *Nature* **418**, 375 (2002).
- [3] S. C. Zimmerman, M. S. Wendland, N. A. Rakow, I. Zharov, and K. S. Suslick, Synthetic hosts by monomolecular imprinting inside dendrimers, *Nature* **418**, 399 (2002).
- [4] M. Boncheva, D. H. Gracias, H. O. Jacobs, and G. M. Whitesides, Biomimetic self-assembly of a functional asymmetrical electronic device, *Proc. Natl. Acad. Sci.* **99**, 4937 (2002).
- [5] D. H. Gracias, M. Boncheva, O. Omoregie, and G. M. Whitesides, Biomimetic self-assembly of helical electrical circuits using orthogonal capillary interactions, *Appl. Phys. Lett.* **80**, 2802 (2002).
- [6] A. Prokop, Bioartificial organs in the twenty-first century - Nanobiological devices, *Annals of the New York Academy of Sciences* **499**, 472 (2001).
- [7] B. Kasemo, Biological Surface Science, *Curr. Op. Sol. St. Mat. Sci.* **3**, 451 (1998).
- [8] B. Kasemo, Biological Surface Science, *Surf. Sci.* **500**, 656 (2002).
- [9] J. Alper, Stretching the Limits, *Science* **297**, 329 (2002).
- [10] A. Abbott, The society of proteins, *Nature* **417**, 894 (2002).
- [11] M. Miessner, M. G. Peter, and J. F. V. Vincent, Preparation of insect-cuticle-like biomimetic materials, *Biomacromolecules* **2**, 369 (2002).

- [12] B. Chen, X. Peng, W. Wang, J. Zhang, and R. Zhang, Research on the microstructure of insect cuticle and the strength of a biomimetic preformed hole composite, *Micron* **33**, 571 (2002).
- [13] A. Lazaris, Spider Silk Fibers Spun from Soluble Recombinant Silk Produced in Mammalian Cells, *Science* **295**, 472 (2002).
- [14] E. Oroudjev, J. Soares, S. Arcidiacono, J. B. Thompson, S. A. Fossey, and H. G. Hansma, Segmented nanofibers of spider dragline silk: Atomic force microscopy and single-molecule force spectroscopy, *Proc. Natl. Acad. Sci.* **99** (Suppl. 2), 6460 (2002).
- [15] J. B. Thompson, J. H. Kindt, B. Drake, H. G. Hansma, D. E. Morse, and P. K. Hansma, Bone indentation recovery time correlates with bond reforming time, *Nature* **414**, 773 (2001).
- [16] L. A. Estroff and A. D. Hamilton, At the Interface of Organic and Inorganic Chemistry: Bioinspired Synthesis of Composite Materials, *Chem. Mater.* **13**, 3227 (2001).
- [17] C. M. Zaremba, A. M. Belcher, M. Fritz, Y. Li, S. Mann, P. K. Hansma, D. E. Morse, J. S. Speck, and G. D. Stucky, Critical Transitions in the Biofabrication of Abalone Shells and Flat Pearls, *Chem. Mater.* **8**, 679 (1996).
- [18] T. E. Schäffer, C. Ionescu-Zanetti, R. Proksch, M. Fritz, D. A. Walters, N. Almqvist, C. M. Zaremba, A. M. Belcher, B. L. Smith, G. D. Stucky, D. E. Morse, and P. K. Hansma, Does Abalone Nacre Form by Heteroepitaxial Nucleation or by Growth through Mineral Bridges?, *Chem. Mater.* **9**, 1731 (1997).
- [19] T. A. Taton, C. A. Mirkin, and R. L. Letsinger, Scanometric DNA Array Detection with Nanoparticle Probes, *Science* **289**, 1757 (2000).
- [20] K. Haupt and K. Mosbach, Molecularly Imprinted Polymers and Their Use in Biomimetic Sensors, *Chem. Rev.* **100**, 2495 (2000).
- [21] M. D. Marazuela and M. C. Moreno-Bondi, Fiber-optic biosensors - an overview, *Anal. Bioanal. Chem.* **372**, 664 (2002).
- [22] A. F. Collings and F. Caruso, Biosensors: recent advances, *Rep. Prog. Phys.* **60**, 1397 (1997).
- [23] A. P. F. Turner, Biosensors - Sense and Sensitivity, *Science* **290**, 1315 (2000).

-
- [24] G. Stix, Little Big Science, *Sci. Am.* **285**, 26 (2001).
- [25] G. E. Moore, Cramming more components onto integrated circuits, *Electronics* **38**, 114 (1965).
- [26] C. M. Lieber, The incredible shrinking circuit, *Sci. Am.* **285**, 51 (2001).
- [27] K. K. Berggren, A. Bard, J. L. Wilbur, J. D. Gillaspay, A. D. Helg, J. J. McClland, S. L. Rolston, W. D. Phillips, M. Prentiss, and G. Whitesides, Microlithography by Using Neutral Metalstable Atoms and Self-Assembled Monolayers, *Science* **269**, 1255 (1995).
- [28] C. Joachim, J. K. Gimzewski, and A. Aviram, Electronics using hybrid-molecular and mono-molecular devices, *Nature* **408**, 541 (2000).
- [29] D. S. Franceschi and L. Kouwenhoven, Electronics and the single atom, *Nature* **417**, 701 (2002).
- [30] M. Schulz, The end of the road for silicon?, *Nature* **399**, 729 (1999).
- [31] R. Service, Molecules Get Wired, *Science* **294**, 2442 (2002).
- [32] G. Binnig, H. Rohrer, C. Gerber, and E. Weibel, Surface Studies by Scanning Tunneling Microscopy, *Phys. Rev. Lett.* **49**, 57 (1982).
- [33] G. Binnig, C. F. Quate, and C. Gerber, Atomic Force Microscopy, *Phys. Rev. Lett.* **56**, 930 (1986).
- [34] G. Whitesides, J. Mathias, and C. Seto, Molecular Self-Assembly and Nanochemistry: A Chemical Strategy for the Synthesis of Nanostructures, *Science* **254**, 1312 (1991).
- [35] G. Whitesides and B. Grzybowski, Self-Assembly at All Scales, *Science* **295**, 2418 (2002).
- [36] V. Percec, M. Glodde, T. K. Bera, Y. Miura, I. Shiyankovskaya, K. D. Singer, V. S. K. Balagurusamy, P. A. Heiney, I. Schnell, A. Rapp, H.-W. Spiess, S. D. Hudson, and H. Duan, Self-organization of supramolecular helical dendrimers into complex electronic materials, *Nature* **419**, 384 (2002).
- [37] E. W. Meijer and A. P. Schenning, Chemistry: Material marriage in electronics, *Nature* **419**, 353 (2002).

- [38] N. C. Seeman and A. M. Belcher, Emulating biology: Building nanostructures from the bottom up, *Proc. Natl. Acad. Sci.* **99** (Suppl. 2), 6451 (2002).
- [39] O. Ikkala and G. t. Brinke, Functional Materials Based on Self-Assembly of Polymeric Supramolecules, *Science* **295**, 2407 (2002).
- [40] C. Anfinsen, Principles that govern the folding of protein chains, *Science* **181**, 223 (1973).
- [41] D. Baker, A surprising simplicity to protein folding, *Nature* **405**, 39 (2000).
- [42] E. M. Zahidi, H. Oudghiri-Hassani, and P. H. McBreen, Formation of thermally stable alkylidene layers on a catalytically active surface, *Nature* **409**, 1023 (2001).
- [43] B. Kasemo and J. Gold, Implant Surfaces and Interface Processes, *Adv. Dent. Res.* **13**, 8 (1999).
- [44] J. Fritz, M. K. Baller, H. P. Lang, H. Rothuizen, P. Vettiger, E. Meyer, H.-J. Güntherodt, C. Gerber, and J. K. Gimzewski, Translating Biomolecular Recognition into Nanomechanics, *Science* **288**, 316 (2000).
- [45] M. K. Baller, H. P. Lang, J. Fritz, C. Gerber, J. K. Gimzewski, U. Drechsler, H. Rothuizen, M. Despont, P. Vettiger, F. M. Battiston, J. P. Ramsayder, P. Fornaro, E. Meyer, and H.-J. Güntherodt, A cantilever array-based artificial nose, *Ultramicroscopy* **82**, 1 (2000).
- [46] F. Schreiber, Structure and growth of self-assembling monolayers, *Prog. Surf. Sci.* **65**, 151 (2000).
- [47] G. E. Poirier and E. D. Pylant, The Self-Assembly Mechanism of Alkanethiols on Au(111), *Science* **272**, 1145 (1996).
- [48] C. D. Bain and G. Whitesides, Modelling Organic Surfaces with Self-Assembled Monolayers, *Angew. Chem. Int. Ed.* **28**, 506 (1989).
- [49] K. L. Prime and G. Whitesides, Self-assembled Organic Monolayers: Model Systems for Studying Adsorption of Proteins at Surfaces, *Science* **252**, 1164 (1991).
- [50] R. Koch, M. Borbonus, O. Haase, and K.-H. Rieder, Reconstruction Behaviour of fcc(110) Transition Metal Surfaces, *Appl. Phys. A* **55**, 417 (1992).

- [51] T. Gritsch, D. Coulman, R. J. Behm, and G. Ertl, A scanning tunneling microscopy investigation of the structure of the Pt(110) and Au(110) surfaces, *Surf. Sci.* **257**, 297 (1991).
- [52] J. V. Barth, H. Brune, G. Ertl, and R. J. Behm, Scanning tunneling microscopy observations on the reconstructed Au(111) surface: Atomic structure, long-range superstructure, rotational domains, and surface defects, *Phys. Rev. B* **42**, 9307 (1990).
- [53] G. Nelson, J. Chandrashekar, M. A. Hoon, L. Feng, G. Zhao, N. J. P. Ryba, and C. S. Zuker, An amino-acid taste receptor, *Nature* **416**, 199 (2002).
- [54] A. Dally, Thalidomide: Was the tragedy preventable?, *The Lancet* **351**, 1197 (1998).
- [55] L. H. Easson and E. Stedman, Studies on the relationship between chemical constitution and physiological action, *Biochem. J.* **27**, 1257 (1933).
- [56] T. D. Booth, D. Wahnou, and I. W. Wainer, Is chiral recognition a three-point process?, *Chirality* **9**, 96 (1997).
- [57] W. A. de Heer, The physics of simple metal clusters: experimental aspects and simple models, *Review of Modern Physics* **65**, 611 (1993).
- [58] C. J. Chen, *Introduction to Scanning Tunneling Microscopy* (Oxford University Press, New York, Oxford, 1993).
- [59] J. Bardeen, Tunneling from a Many-Particle Point of View, *Phys. Rev. Lett.* **6**, 57 (1961).
- [60] J. Tersoff and D. R. Hamann, Theory and Application for the Scanning Tunneling Microscope, *Phys. Rev. Lett.* **50**, 1998 (1983).
- [61] I. S. Tilinin, M. K. Rose, J. C. Dunphy, M. Salmeron, and M. A. V. Hove, Identification of adatoms on metal surfaces by STM: experiment and theory, *Surf. Sci.* **418**, 511 (1998).
- [62] L. Bartels, G. Meyer, and K.-H. Rieder, Controlled vertical manipulation of single CO molecules with the scanning tunneling microscope: A route to chemical contrast, *Appl. Phys. Lett.* **71**, 213 (1997).
- [63] M. P. Seah and W. A. Dench, Compilation of experimental data determined with various electron energies for a large variety of materials, *Surf. Interf. Anal.* **1**, 1 (1979).

- [64] P. A. Redhead, Thermal Desorption of Gases, *Vacuum* **12**, 203 (1962).
- [65] W. J. Here, L. Radom, P. v. R. Schleyer, and J. A. Pople, *Ab Initio Molecular Orbital Theory* (Wiley, New York, 1987).
- [66] W. Kohn, Nobel Lecture: Electronic structure of matter — wave functions and density functionals, *Review of Modern Physics* **71**, 1253 (1999).
- [67] P. Hohenberg and W. Kohn, Inhomogeneous Electron Gas, *Phys. Rev.* **136**, B864 (1964).
- [68] W. Kohn and L. J. Sham, Self-Consistent Equations Including Exchange and Correlation Effects, *Phys. Rev.* **140**, A1133 (1965).
- [69] B. Hammer, K. W. Jacobsen, and J. K. Nørskov, Role of nonlocal exchange correlation in activated adsorption, *Phys. Rev. Lett.* **70**, 3971 (1993).
- [70] J. P. Perdew, in *Electronic Structure of Solids '91*, Vol. 17 of *Physical Research*, edited by P. Ziesche and H. Eschrig (Akademie Verlag, Berlin, 1991), pp. 11–20.
- [71] J. P. Perdew, J. A. Chevary, S. H. Vosko, K. A. Jackson, M. R. Pederson, and D. J. Singh, Atoms, molecules, solids, and surfaces: Applications of the generalized gradient approximation for exchange and correlation, *Phys. Rev. B* **46**, 6671 (1992).
- [72] J. P. Perdew, K. Burke, and M. Ernzerhof, Generalized Gradient Approximation Made Simple, *Phys. Rev. Lett.* **77**, 3865 (1996).
- [73] B. Hammer, L. B. Hansen, and J. K. Nørskov, Improved adsorption energetics within density-functional theory using revised Perdew-Burke-Ernzerhof functionals, *Phys. Rev. B* **59**, 7413 (1999).
- [74] K. W. Jacobsen, J. K. Nørskov, and M. J. Puska, Interatomic interactions in the effective-medium theory, *Phys. Rev. B* **35**, 7423 (1987).
- [75] K. W. Jacobsen, Bonding in metallic systems: an effective-medium approach, *Comments Condens. Matter Phys.* **14**, 129 (1988).
- [76] P. Stoltze, Simulation of Surface Defects, *J. Phys. Cond. Matt.* **6**, 9495 (1994).
- [77] J. K. Nørskov, K. W. Jacobsen, P. Stoltze, and L. B. Hansen, Many-atom interactions in metals, *Surf. Sci.* **283**, 277 (1993).

- [78] J. K. Nørskov, K. W. Jacobsen, and P. Stoltze, A semi-empirical effective medium theory for metals and alloys, *Surf. Sci.* **366**, 394 (1996).
- [79] L. Pasteur, *C. R. Seances Acad. Sci. Paris* **26**, 535 (1848).
- [80] P. Luger and M. Weber, DL-Cysteine at 298 K, *Acta Cryst.* **55**, 1882 (1999).
- [81] J. D. Horvath and A. J. Gellman, Enantiospecific Desorption of Chiral Compounds from Chiral Cu(643) and Achiral Cu(111) Surfaces, *J. Am. Chem. Soc.* **124**, 2384 (2002).
- [82] C. F. McFadden, P. S. Cremer, and A. J. Gellman, Adsorption of Chiral Alcohols on “Chiral” Metal Surfaces, *Langmuir* **12**, 2483 (1996).
- [83] D. S. Sholl, A. Asthagiri, and T. D. Power, Naturally Chiral Metal Surfaces as Enantiospecific Adsorbents, *J. Phys. Chem. B* **105**, 4771 (2001).
- [84] D. S. Sholl, Adsorption of Chiral Hydrocarbons on Chiral Platinum Surfaces, *Langmuir* **14**, 862 (1998).
- [85] T. D. Power and D. S. Sholl, Enantiospecific adsorption of chiral hydrocarbons on naturally chiral Pt and Cu surfaces, *J. Vac. Sci. Technol. A* **17**, 1700 (1999).
- [86] G. A. Attard, A. Ahmadi, J. Feliu, A. Rodes, E. Herrero, S. Blais, and G. Jerkiewicz, Temperature Effects in the Enantiomeric Electro-Oxidation of D- and L-Glucose on Pt(643), *J. Phys. Chem. B* **103**, 1381 (1999).
- [87] P. S. Weiss, Molecules join the assembly line, *Nature* **413**, 585 (2001).
- [88] T. Yokoyama, S. Yokoyama, T. Kamikado, Y. Okuno, and S. Mashiko, Selective assembly on a surface of supramolecular aggregates with controlled size and shape, *Nature* **413**, 619 (2001).
- [89] A. Dmitriev, N. Lin, J. Weckesser, J. V. Barth, and K. Kern, Supramolecular Assemblies of Trimesic Acid on a Cu(100) Surface, *J. Phys. Chem. B* **106**, 6907 (2002).
- [90] J. V. Barth, J. Weckesser, C. Cai, P. Günter, L. Bürgi, O. Jeandupeux, and K. Kern, Building Supramolecular Nanostructures at Surfaces by Hydrogen Bonding, *Angew. Chem. Int. Ed.* **39**, 1230 (2000).

- [91] J. Weckesser, A. D. Vita, J. V. Barth, C. Cai, and K. Kern, Mesoscopic Correlation of Supramolecular Chirality in One-Dimensional Hydrogen-Bonded Assemblies, *Phys. Rev. Lett.* **87**, 096101 (2001).
- [92] J. V. Barth, J. Weckesser, G. Trimarchi, M. Vladimirova, A. D. Vita, C. Cai, H. Brune, P. Günter, and K. Kern, Stereochemical Effects in Supramolecular Self-Assembly at Surfaces: 1-D versus 2-D Enantiomorphic Ordering for PVBA and PEBA on Ag(111), *J. Am. Chem. Soc.* **124**, 7991 (2002).
- [93] Y. Huang, X. Duan, Q. Wei, and C. M. Lieber, Directed Assembly of One-Dimensional Nanostructures into Functional Networks, *Science* **291**, 630 (2001).
- [94] Y. Okawa and M. Aono, Nanoscale control of chain polymerization, *Nature* **409**, 683 (2001).
- [95] Y. Okawa and M. Aono, Linear chain polymerization initiated by a scanning tunneling microscope tip at designated positions, *J. Chem. Phys.* **115**, 2317 (2001).
- [96] G. Lopinski, D. Wayner, and R. Wolkow, Self-directed growth of molecular nanostructures on silicon, *Nature* **406**, 48 (2000).
- [97] M. Böhringer, K. Morgenstern, W.-D. Schneider, R. Berndt, F. Mauri, A. D. Vita, and R. Car, Two-Dimensional Self-Assembly of Supramolecular Clusters and Chains, *Phys. Rev. Lett.* **83**, 324 (1999).
- [98] A. Ulman, *An Introduction to Ultrathin Organic Films: From Langmuir-Blodgett to Self Assembly* (Academic Press, Boston, MA, 1991).
- [99] G. E. Poirier, Mechanism of Formation of Au Vacancy Islands in Alkanethiol Monolayers on Au(111), *Langmuir* **13**, 2019 (1997).
- [100] G. E. Poirier, Butanethiol self-assembly on Au(001): The 1×4 Au missing row, $c(2 \times 8)$ molecular lattice, *J. Vac. Sci. Technol. B* **14**, 1453 (1996).
- [101] H.-J. Himmel, C. Wöll, R. Gerlach, G. Polanski, and H.-G. Rubahn, Structure of Heptanethiolate Monolayers on Au(111): Adsorption from Solution vs Vapor Deposition, *Langmuir* **13**, 602 (1997).
- [102] D. Lavrich, S. M. Wetterer, S. Bernasek, and G. Scoles, Physisorption and Chemisorption of Alkanethiols and Alkyl Sulfides on Au(111), *J. Phys. Chem. B* **102**, 3456 (1998).

- [103] R. Staub, M. Toerker, T. Fritz, T. Schmitz-Hübsch, F. Sellam, and K. Leo, Flat Lying Pin-Stripe of Decanethiol Self-Assembled Monolayers on Au(111), *Langmuir* **14**, 6693 (1998).
- [104] A. Ulman, Formation and Structure of Self-Assembled Monolayers, *Chem. Rev.* **96**, 1533 (1996).
- [105] A. J. Leavitt and T. P. J. Beebe, Chemical reactivity studies of hydrogen sulfide on Au(111), *Surf. Sci.* **314**, 23 (1994).
- [106] V. Bondzie, S. J. Dixon-Warren, and Y. Yu, Molecular beam study of the adsorption and desorption of hydrogen sulfide on Au{100}, *J. Chem. Phys.* **111**, 10670 (1999).
- [107] A. R. Alemozafar, X.-C. Guo, and R. J. Madix, Adsorption and reaction of sulfur dioxide with Cu(110) and Cu(110)-p(2×1)-O, *J. Chem. Phys.* **116**, 4698 (2002).
- [108] Q. Chi, J. Zhang, J. U. Nielsen, E. P. Friis, I. Chorkendorff, G. W. Canters, J. E. T. Andersen, and J. Ulstrup, Molecular Monolayers and Interfacial Electron Transfer of Pseudomonas aeruginosa Azurin on Au(111), *J. Am. Chem. Soc.* **122**, 4047 (2000).
- [109] Y. C. Sasaki, K. Yasuda, Y. Suzuki, T. Ishibashi, I. Satoh, Y. Fujiki, and S. Ishiwata, Two-Dimensional Arrangement of a Functional Protein by Cysteine-Gold Interaction: Enzyme Activity and Characterization of a Protein Monolayer on a Gold Substrate, *Biophys. J.* **72**, 1842 (1997).
- [110] M. Carrion-Vazquez, A. F. Oberhauser, S. B. Fowler, P. E. Marszalek, S. E. Broedel, J. Clarke, and J. M. Fernandez, Mechanical and chemical unfolding of a single protein: A comparison, *Proc. Natl. Acad. Sci.* **96**, 3694 (1999).
- [111] J. A. Rodriguez and J. Hrbek, Interaction of Sulfur with Well-Defined Metal and Oxide Surfaces: Unraveling the Mysteries behind Catalyst Poisoning and Desulfurization, *Acc. Chem. Res.* **32**, 719 (1999).
- [112] J. V. Lauritsen, S. Helveg, E. Lægsgaard, I. Stensgaard, B. S. Clausen, H. Topsøe, and F. Besenbacher, Atomic-Scale Structure of Co-Mo-S Nanoclusters in Hydrotreating Catalysts, *J. Catal.* **197**, 1 (2001).
- [113] P. J. Feibelman, Modification of Transition Metal Electronic Structure by P, S, Cl and Li Adatoms, *Surf. Sci.* **149**, 48 (1985).

- [114] B. Hammer and J. K. Nørskov, Theoretical Surface Science and Catalysis – Calculation and Concepts, *Adv. Catal.* **45**, 71 (2000).
- [115] I. Touzov and B. Gorman, A Scanning Tunneling Microscopy Study of the Interaction of H₂S with a Au(111) Surface: Characterization of Corrosion and Monolayer Structures, *Langmuir* **13**, 4850 (1997).
- [116] G. Liu, J. A. Rodriguez, J. Dvorak, J. Hrbek, and T. Jirsak, Chemistry of sulfur-containing molecules on Au(111): thiophene, sulfur dioxide, and methanethiol adsorption, *Surf. Sci.* **505**, 295 (2002).
- [117] V. A. Bondzie, S. C. Parker, and C. T. Campbell, Oxygen adsorption on well-defined gold particles on TiO₂(110), *J. Vac. Sci. Technol. A* **17**, 1717 (1999).
- [118] M. Kostelitz, J. L. Domagne, and J. Oudar, A study of the adsorption of sulphur on gold by low energy electron diffraction and Auger spectroscopy, *Surf. Sci.* **34**, 431 (1973).
- [119] D. M. Jaffey and R. J. Madix, The adsorption of hydrogen sulfide on clean and sulfided Au(110), *Surf. Sci.* **258**, 359 (1991).
- [120] B. Frühberger, M. Grunz, and D. J. Dwyer, The formation and stability of sulphydryl-groups on the Au(110) surface, *J. Phys. Chem.* **98**, 609 (1994).
- [121] J. Gottschalck and B. Hammer, A density functional theory study of the adsorption of sulfur, mercapto, and methylthiolate on Au(111), *J. Chem. Phys.* **116**, 784 (2002).
- [122] M. C. Vargas, P. Giannozzi, A. Selloni, and G. Scoles, Coverage-Dependent Adsorption of CH₃S and (CH₃S)₂ on Au(111): a Density Functional Theory Study, *J. Phys. Chem. B* **105**, 9509 (2001).
- [123] H. Grönbeck, A. Curioni, and W. Andreoni, Thiols and Disulfides on the Au(111) Surface: The Headgroup-Gold Interaction, *J. Am. Chem. Soc.* **122**, 3839 (2000).
- [124] Y. Morikawa, T. Hayashi, C. C. Liew, and H. Nozoye, First-principles theoretical study of alkylthiolate adsorption on Au(111), *Surf. Sci.* **507-510**, 46 (2002).
- [125] L. M. Molina and B. Hammer, Theoretical study of adsorbate-induced reconstructions on the Au(111) surface, *Chem. Phys. Lett.* **360**, 264 (2002).

- [126] P. Löfgren, A. Krozer, J. Lausmaa, and B. Kasemo, Glycine on Pt(111): a TDS and XPS study, *Surf. Sci.* **370**, 277 (1997).
- [127] K.-H. Ernst and K. Christmann, The Interaction of Glycine with a Platinum (111) Surface, *Surf. Sci.* **224**, 277 (1989).
- [128] S. Barlow, K. Kitching, S. Haq, and N. V. Richardson, A study of glycine adsorption on a Cu(110) surface using reflection absorption infrared spectroscopy, *Surf. Sci.* **401**, 322 (1998).
- [129] J. Hasselström, O. Karis, M. Weinelt, N. Wassnahl, A. Nilsson, M. Nyberg, L. G. M. Pettersson, M. G. Samant, and J. Stöhr, The adsorption structure of glycine adsorbed on Cu(110); comparison with formate and acetate Cu(110), *Surf. Sci.* **407**, 221 (1998).
- [130] N. Booth, D. P. Woodruff, O. Schaff, T. Giessel, R. Lindsay, P. Baumgärtel, and A. M. Bradshaw, Determination of the local structure of glycine adsorbed on Cu(110), *Surf. Sci.* **397**, 258 (1999).
- [131] Q. Chen, D. J. Frankel, and N. V. Richardson, Chemisorption induced chirality: glycine on Cu{110}, *Surf. Sci.* **497**, 37 (2002).
- [132] X. Zhao, Z. Gai, R. Zhao, W. Yang, and T. Sakurai, Adsorption of glycine on Cu(001) and related step faceting and bunching, *Surf. Sci.* **424**, L347 (1999).
- [133] X. Zhao, R. Zhao, and W. Yang, Adsorption of alanine on Cu(001) studied by scanning tunneling microscopy, *Surf. Sci.* **442**, L995 (1999).
- [134] J. Williams, S. Haq, and R. Raval, The bonding and orientation of the amino acid L-alanine on Cu(110) determined by RAIRS, *Surf. Sci.* **368**, 303 (1996).
- [135] A. S. Dakkouri, D. M. Kolb, R. Edelstein-Shima, and D. Mandler, Scanning Tunneling Microscopy Study of L-Cysteine on Au(111), *Langmuir* **12**, 2849 (1996).
- [136] G. Doderio, L. D. Michieli, O. Cavalleri, R. Rolandi, L. Oliveri, A. Dacca, and R. Parodi, L-Cysteine chemisorption on gold: an XPS and STM study, *Colloids and Surfaces A* **175**, 121 (2000).
- [137] W. Yang, J. J. Gooding, and D. B. Hibbert, Characterisation of gold electrodes modified with self-assembled monolayers of l-cysteine for the adsorptive stripping analysis of copper, *Journal of Electroanalytical Chemistry* **516**, 10 (2001).

- [138] O. Cavalleri, L. Oliveri, A. Dacca, R. Parodi, and R. Rolandi, XPS measurements on L-cysteine and 1-octadecanethiol self-assembled films: a comparative study, *Appl. Surf. Sci.* **175-176**, 357 (2001).
- [139] L. Qingwen, G. Hong, W. Yiming, L. Guoan, and M. Jie, Studies on Self-Assembly Monolayers of Cysteine on Gold by XPS, QCM, and Electrochemical Techniques, *Electroanalysis* **13**, 1342 (2001).
- [140] J. Zhang, Q. Chi, J. U. Nielsen, E. P. Friis, J. E. T. Andersen, and J. Ulstrup, Two-Dimensional Cysteine and Cystine Cluster Networks on Au(111) Disclosed by Voltammetry and in Situ Scanning Tunneling Microscopy, *Langmuir* **16**, 7229 (2000).
- [141] J. Zhang, Q. Chi, J. E. T. Andersen, A. G. Hansen, J. U. Nielsen, and J. Ulstrup, Organization and Control of Nanoscale Structures on Au(111), *Probe Microscopy* **2**, 151 (2001).
- [142] Q.-M. Xu, L.-J. Wan, C. Wang, C.-L. Bai, Z.-Y. Wang, and T. Nozawa, New Structure of L-Cysteine Self-Assembled Monolayer on Au(111): Studies by In Situ Scanning Tunneling Microscopy, *Langmuir* **17**, 6203 (2001).
- [143] K. Uvdal, P. Bodö, and B. Liedberg, L-cysteine Adsorbed on Gold and Copper: An X-Ray Photoelectron Spectroscopy Study, *J. Colloid Interface Sci.* **149**, 162 (1992).
- [144] M. O. Lorenzo, C. J. Baddeley, C. Muryn, and R. Raval, Extended surface chirality from supramolecular assemblies of adsorbed chiral molecules, *Nature* **404**, 376 (2000).
- [145] R. Raval, Creating chiral architectures at metal surfaces, *J. Phys. Cond. Matt.* **14**, 4119 (2002).
- [146] V. Humblot, S. Haq, C. Muryn, W. A. Hofer, and R. Raval, From Local Adsorption Stresses to Chiral Surfaces: (R,R)-Tartaric Acid on Ni(110), *J. Am. Chem. Soc.* **124**, 503 (2002).
- [147] C. J. Eckhardt, N. M. Peachey, D. R. Swanson, J. M. Takacs, M. A. Khan, X. Gong, J.-H. Kim, J. Wang, and A. Uphaus, Separation of chiral phases in monolayer crystals of racemic amphiphiles, *Nature* **362**, 614 (1993).
- [148] S. D. Feyter, P. C. M. Grim, M. Rücker, P. Vanoppen, C. Meiners, M. Sieffert, S. Valiyaveetil, K. Müllen, and F. D. Schryver, Expression of Chirality by Achiral Coadsorbed Molecules in Chiral Monolayers Observed by STM, *Angew. Chem. Int. Ed.* **37**, 1223 (1998).

- [149] F. Stevens, D. J. Dyer, and D. M. Walba, Direct Observation of Enantiomorphous Monolayer Crystals from Enantiomers by Scanning Tunneling Microscopy, *Angew. Chem. Int. Ed.* **35**, 900 (1996).
- [150] S. J. Sowerby, W. M. Heckl, and G. B. Petersen, Chiral Symmetry Breaking During the Self-Assembly of Monolayers from Achiral Purine Molecules, *J. Mol. Evol.* **43**, 419 (1996).
- [151] X. Zhao, R. G. Zhao, and W. S. Yang, Scanning Tunneling Microscopy Investigation of L-lysine adsorbed on Cu(001), *Langmuir* **16**, 9812 (2000).
- [152] X. Zhao, Fabricating Homochiral Facets on Cu(001) with L-lysine, *J. Am. Chem. Soc.* **122**, 12584 (2000).
- [153] Q. Chen, C. W. Lee, D. J. Frankel, and N. V. Richardson, The formation of enantiospecific phases on a Cu(110) surface, *PhysChemComm* **9**, (1999).
- [154] R. M. Hazen, T. R. Filley, and G. A. Goodfriend, Selective adsorption of L- and D-amino acids on calcite: Implications for biochemical homochirality, *Proc. Natl. Acad. Sci.* **98**, 5487 (2001).
- [155] R. M. Hazen, Life's Rocky Start, *Sci. Am.* **284**, 76 (2001).
- [156] D. B. Cline, *Physical Origin of Homochirality in Life* (American Institute of Physics Conference Proceedings 379, Woodbury, New York, 1995).
- [157] M. Böhringer, K. Morgenstern, W.-D. Schneider, and R. Berndt, Separation of a Racemic Mixture of Two-Dimensional Molecular Clusters by Scanning Tunneling Microscopy, *Angew. Chem. Int. Ed.* **38**, 821 (1999).
- [158] G. Lopinski, D. Moffatt, D. Wayner, and R. Wolkow, Determination of the absolute chirality of individual adsorbed molecules using the scanning tunneling microscope, *Nature* **392**, 909 (1998).
- [159] S. B. Lee, D. T. Mitchell, L. Trofin, T. K. Nevanen, H. Söderlund, and C. R. Martin, Antibody-Based Bio-Nanotube Membranes for Enantiomeric Drug Separations, *Science* **296**, 2198 (2002).
- [160] M. Schunack, E. Lægsgaard, I. Stensgaard, I. Johannsen, and F. Besenbacher, A Chiral Metal Surface, *Angew. Chem. Int. Ed.* **40**, 2623 (2001).
- [161] A. Ahmadi, G. Attard, J. Feliu, and A. Rodes, Surface Reactivity at "Chiral" Platinum Surfaces, *Langmuir* **15**, 2420 (1999).

- [162] V. Fiorentini, M. Methfessel, and M. Scheffler, Reconstruction Mechanism of fcc Transition Metal (001) Surfaces, *Phys. Rev. Lett.* **71**, 1051 (1993).
- [163] R. J. Needs, M. J. Godfrey, and M. Mansfield, Theory of surface stress and surface reconstruction, *Surf. Sci.* **242**, 215 (1991).
- [164] G. Binnig, H. Rohrer, C. Gerber, and E. Weibel, (111) facets as the origin of reconstructed Au(110) surfaces, *Surf. Sci.* **131**, L379 (1983).
- [165] M. Sturmat, R. Koch, and K.-H. Rieder, Real Space Investigation of the Roughening and Deconstruction Transitions of Au(110), *Phys. Rev. Lett.* **77**, 5071 (1996).
- [166] J. K. Gimzewski, R. Berndt, and R. R. Schlittler, Scanning tunneling microscopy study of antiphase domain boundaries, dislocations, and local mass transport on Au(110) surfaces, *Phys. Rev. B* **45**, 6844 (1992).
- [167] N. D. S. Canning, D. Outka, and R. J. Madix, The Adsorption of Oxygen on Gold, *Surf. Sci.* **141**, 240 (1994).
- [168] A. Ihs and B. Liedberg, Chemisorption of L-Cysteine and 3-Mercaptopropionic Acid on Gold and Copper Surfaces: An Infrared Reflection-Absorption Study, *J. Colloid Interface Sci.* **144**, 282 (1991).
- [169] P. Tarakeshwar and S. Manogaran, Conformational effects on vibrational frequencies of cysteine and serine: an ab initio study, *Journal of Molecular Structure* **303**, 205 (1994).
- [170] H. Li, C. Wurrey, and G. Thomas, Structural studies of viruses by laser Raman spectroscopy. Part XXXVI. Cysteine conformation and sulfhydryl interactions in proteins and viruses. 2. Normal coordinate analysis of the cysteine side chain in model compounds, *J. Am. Chem. Soc.* **114**, 7463 (1992).
- [171] A. Kühnle, T. R. Linderoth, B. Hammer, and F. Besenbacher, Chiral recognition in dimerization of adsorbed cysteine observed by scanning tunnelling microscopy, *Nature* **415**, 891 (2002).
- [172] B. Hammer, Cysteine dimerisation in the gas phase, *private communication* (2002).
- [173] Z. Sljivancanin, K. V. Gothelf, and B. Hammer, Density functional theory of enantioselective adsorption at chiral surfaces, *J. Am. Chem. Soc.* in press (2002).

- [174] T. Hayashi, Y. Morikawa, and H. Nozoye, Adsorption state of dimethyl disulfide on Au(111): Evidence for adsorption as thiolate at the bridge site, *J. Chem. Phys.* **114**, 7615 (2001).
- [175] Y. Yourdshahyan and A. M. Rappe, Structure and energetics of alkanethiol adsorption on the Au(111) surface, *J. Chem. Phys.* **117**, 825 (2002).
- [176] Z. Sljivancanin and B. Hammer, Oxygen dissociation at close-packed Pt terraces, Pt steps, and Ag-covered Pt-steps studied with density functional theory, *Surf. Sci.* **515**, 235 (2002).
- [177] J. S. Siegel, Homochiral imperative of molecular evolution, *Chirality* **10**, 24 (1998).
- [178] W. A. Bonner, Chirality and Life, *Origins Life Evol. Biosphere* **25**, 175 (1995).
- [179] W. A. Bonner, The Quest for Chirality, *AIP Conference Proceedings* **379**, 17 (1996).
- [180] K. Soai, S. Osanai, K. Kadowaki, S. Yonekubo, T. Shibata, and I. Sato, d- and l-Quartz-Promoted Highly Enantioselective Synthesis of a Chiral Organic Compound, *J. Am. Chem. Soc.* **121**, 11235 (1999).
- [181] D. Kondepudi, R. Kaufman, and N. Singh, Chiral Symmetry Breaking in Sodium Chlorate Crystallisation, *Science* **250**, 975 (1990).
- [182] F. Charra and J. Cousty, Surface-Induced Chirality in a Self-Assembled Monolayer of Discotic Liquid Crystal, *Phys. Rev. Lett.* **80**, 1682 (1998).
- [183] J. S. Siegel, Chemistry: Shattered mirrors, *Nature* **419**, 346 (2002).
- [184] D. A. Singleton and L. K. Vo, Enantioselective Synthesis without Discrete Optically Active Additives, *J. Am. Chem. Soc.* **124**, 10010 (2002).
- [185] D. G. Blackmond, Kinetic Aspects of Nonlinear Effects in Asymmetric Catalysis, *Acc. Chem. Res.* **33**, 402 (2000).
- [186] S. Lukas, G. Witte, and C. Wöll, Novel Mechanism for Molecular Self-Assembly on Metal Substrates: Unidirectional Rows of Pentacene on Cu(110) Produced by a Substrate-Mediated Repulsion, *Phys. Rev. Lett.* **88**, 028301 (2002).

- [187] K. Morgenstern, E. Lægsgaard, I. Stensgaard, F. Besenbacher, M. Böhlinger, W.-D. Schneider, R. Berndt, F. Mauri, A. D. Vita, and R. Car, Stability of two-dimensional nanostructures, *Appl. Phys. A* **69**, 559 (1999).
- [188] L. Bartels, G. Meyer, and K.-H. Rieder, Basic Steps of Lateral Manipulation of Single Atoms and Diatomic Clusters with a Scanning Tunneling Microscope Tip, *Phys. Rev. Lett.* **79**, 697 (1997).
- [189] C. Kodama, T. Hayashi, and H. Nozoye, Decomposition of alkanethiols adsorbed on Au(111) at low temperature, *Appl. Surf. Sci.* **169-170**, 264 (2001).
- [190] N. D. Lang, Theory of Single-Atom Imaging in the Scanning Tunneling Microscope, *Phys. Rev. Lett.* **56**, 1164 (1986).
- [191] M. Foss, R. Feidenhans'l, M. Nielsen, E. Findeisen, T. Buslap, R. L. Johnson, F. Besenbacher, and I. Stensgaard, X-ray diffraction investigation of the sulphur induced 4×1 reconstruction of Ni(110), *Surf. Sci.* **296**, 283 (1993).
- [192] L. Ruan, I. Stensgaard, E. Lægsgaard, and F. Besenbacher, A scanning tunneling microscopy investigation of the Ni(110)-p(4×1)S phase, *Surf. Sci.* **296**, 275 (1993).
- [193] G. S. Ferguson, M. K. Chaundhury, G. B. Sigal, and G. M. Whitesides, Contact Adhesion of Thin Gold Films on Elastomeric Supports: Cold Welding Under Ambient Conditions, *Science* **253**, 776 (1991).
- [194] S. Helveg, J. V. Lauritsen, E. Lægsgaard, I. Stensgaard, J. K. Nørskov, B. S. Clausen, H. Topsøe, and F. Besenbacher, Atomic-Scale Structure of Single-Layer MoS₂ Nanoclusters, *Phys. Rev. Lett.* **84**, 951 (2000).
- [195] W. G. Cullen and P. N. First, Island shapes and intermixing for submonolayer nickel on Au(111), *Surf. Sci.* **420**, 53 (1999).
- [196] D. D. Chambliss, R. J. Wilson, and S. Chiang, Nucleation of Ordered Ni Island Arrays on Au(111) by Surface-Lattice-Dislocations, *Phys. Rev. Lett.* **66**, 1721 (1991).
- [197] E. Kopatzki, I. D. Baikie, R. J. Behm, and J. A. Meyer, Preferential island nucleation at the elbows of the Au(111) herringbone reconstruction through place exchange, *Surface Science Letters* **365**, L647 (1996).

- [198] G. E. Poirier, Characterization of Organosulfur Molecular Monolayers on Au(111) using Scanning Tunneling Microscopy, *Chem. Rev.* **97**, 1117 (1997).
- [199] A. Ulman, *Self-Assembled Monolayers of Thiols, Thin Films* (Academic Press, San Diego, CA, 1998).
- [200] H. Kondoh, C. Kodama, H. Sumida, and H. Nozoye, Molecular processes of adsorption and desorption of alkanethiol monolayers on Au(111), *J. Chem. Phys.* **111**, 1175 (1999).
- [201] F. Schreiber, A. Eberhardt, T. Y. B. Leung, P. Schwartzand, A. M. Wetterer, D. J. Lavrich, L. Bermann, P. Fenter, P. Eisenberger, and G. Scoles, Adsorption mechanisms, structures, and growth regimes of an archetypal self-assembling system: Decanethiol on Au(111), *Phys. Rev. B* **57**, 12476 (1998).
- [202] G. E. Poirier, W. P. Fitts, and J. M. White, Two-Dimensional Phase Diagram of Decanethiol on Au(111), *Langmuir* **17**, 1176 (2001).
- [203] R. Gerlach, G. Polanski, and H.-G. Rubahn, Structural manipulation of ultrathin organic films on metal surfaces: the case of decane thiol Au(111), *Appl. Phys. A* **65**, 375 (1997).
- [204] M. Toerker, R. Staub, T. Fritz, T. Schmitz-Hübsch, F. Sellam, and K. Leo, Annealed decanethiol monolayers on Au(111) - intermediate phases between structures with high and low molecular surface density, *Surf. Sci.* **445**, 100 (2000).
- [205] Y.-H. Lai, C.-T. Yeh, S.-H. Cheng, P. Liao, and W.-H. Hung, Adsorption and Thermal Decomposition of Alkanethiols on Cu(110), *J. Phys. Chem. B* **106**, 5438 (2002).
- [206] S. M. Driver and D. P. Woodruff, Adsorption Structures of 1-Octanethiol on Cu(111) Studied by Scanning Tunneling Microscopy, *Langmuir* **16**, 6693 (2000).
- [207] S. Vollmer, G. Witte, and C. Wöll, Structural Analysis of Saturated Alkanethiolate Monolayers on Cu(100): Coexistence of Thiolate and Sulfide Species, *Langmuir* **17**, 7560 (2001).
- [208] S. Vollmer, P. Fouquet, G. Witte, C. Boas, M. Kunat, U. Burghaus, and C. Wöll, Low-energy vibrational dynamics of ultrathin organic adlayers: alkanethiols adsorbed on copper, *Surf. Sci.* **462**, 135 (2000).

- [209] H. Rieley, G. K. Kendall, A. Chan, R. G. Jones, J. Lüdecke, D. P. Woodruff, and B. C. C. Cowie, Surface adsorption structures in 1-octanethiol self-assembled on Cu(111), *Surf. Sci.* **392**, 143 (1997).
- [210] A. Imanishi, K. Isawa, F. Matsui, T. Tsuduki, T. Yokoyama, H. Kondoh, Y. Kitajima, and T. Ohta, Structural studies of adsorbed alkanethiols on Cu(111) by use of S and C K-edge X-ray absorption fine structures, *Surf. Sci.* **407**, 282 (1998).
- [211] T. Tsuduki, A. Imanishi, K. Isawa, S. Terada, F. Matsui, M. Kiguchi, T. Yokoyama, and T. Ohta, Adsorption structures of alkanethiols self-assembled monolayers on the Cu(100) surface studied by S-K EXAFS and C-K NEXAFS spectroscopies, *Journal of Synchrotron Radiation* **6**, 787 (1999).
- [212] A. Götzhäuser, S. Panov, and C. Wöll, Determination of molecular-orientation in ultrathin films of aminophenylthiolate on Cu(100) prepared by vapor-phase deposition, *Surface Science Letters* **314**, L849 (1994).
- [213] G. Loepp, S. Vollmer, G. Witte, and C. Wöll, Adsorption of Heptanethiol on Cu(110), *Langmuir* **15**, 3767 (1999).
- [214] S. M. Driver and D. P. Woodruff, Scanning tunnelling microscopy study of the interaction of dimethyl disulphide with Cu(111), *Surf. Sci.* **457**, 11 (2000).
- [215] S. M. Driver and D. P. Woodruff, A new pseudo-(100) sulphur-induced reconstruction of Cu(111) observed by scanning tunnelling microscopy, *Surf. Sci.* **479**, 1 (2001).
- [216] S. M. Driver and D. P. Woodruff, Methanethiolate structural phases on Cu(100) and Cu(410), *Surf. Sci.* **488**, 207 (2001).
- [217] I. Stensgaard, L. Ruan, F. Besenbacher, F. Jensen, and E. Lægsgaard, STM investigations of adsorption induced phases on metal surfaces, *Surf. Sci.* **269/270**, 81 (1992).
- [218] C. D. Wagner, W. M. Riggs, L. E. Davis, and J. F. Moulder, *Handbook of X-ray photoelectron spectroscopy* (Perkin Elmer Cooperation, Eden Prairie, MN, 1979).
- [219] M. S. Kariapper, C. Fisher, D. P. Woodruff, B. C. C. Cowie, and R. G. Jones, A structural study of methanethiolate adsorbed on Cu(100), *J. Phys. Cond. Matt.* **12**, 2153 (2000).

-
- [220] G. Witte and C. Wöll, External vibrations of hydrocarbons on Cu(100), *J. Chem. Phys.* **103**, 5860 (1995).
- [221] A. Grossmann, W. Erley, and H. Ibach, Adsorbate-induced surface stress and surface reconstruction: Oxygen, sulfur and carbon on Ni(111), *Surf. Sci.* **337**, 183 (1995).
- [222] P. Broekmann, M. Wilms, and K. Wandelt, Atomic Structures of a Cu(111) Surface Under Electrochemical Conditions: An In-Situ STM Study, *Surf. Rev. Lett.* **6**, 907 (1999).
- [223] M. Schunack, L. Petersen, A. Kühnle, E. Lægsgaard, I. Stensgaard, I. Johannsen, and F. Besenbacher, Anchoring of organic molecules to a metal surface: HtBDC on Cu(110), *Phys. Rev. Lett.* **86**, 456 (2001).
- [224] D. S. Sutherland, M. Broberg, H. Nygren, and B. Kasemo, Influence of Nanoscale Surface Topography and Chemistry on the Functional Behaviour of an Adsorbed Model Macromolecule, *Macromol. Biosci.* **1**, 270 (2001).
- [225] P. Hanarp, D. Sutherland, J. Gold, and B. Kasemo, Nanostructured model biomaterial surfaces prepared by colloidal lithography, *Nanostruct. Mater.* **12**, 429 (1999).

List of Figures

1	Processes influencing the molecular-structure formation on a substrate surface.	4
2	Cysteine as a biomolecule, a thiol and a chiral molecule.	5
3	Hands are chiral objects.	6
4	One-dimensional tunnelling junction.	12
5	Setup of the Aarhus STM.	14
6	RAIRS metal surface selection rule.	16
7	Notation for chiral molecules.	22
8	CAHN-INGOLD-PRELOG analogy to define the absolute chirality of a kinked fcc(111) surface.	23
9	Self-assembled monolayer of alkanethiols on a Au(111) surface.	25
10	The (1×2) missing-row reconstructed Au(110) surface.	34
11	Ball model of the cysteine molecule.	35
12	Overview of the cysteine structures on Au(110)- (1×2)	36
13	STM images after evaporation of L cysteine on Au(110) held at room temperature.	38
14	RAIRS spectrum of cysteine adsorbed onto Au(110) held at room temperature.	40
15	Low coverage of L cysteine on Au(110) after annealing at 380 K.	43
16	D cysteine dimers on Au(110).	44
17	DL cysteine dimers.	45
18	Adsorbate-induced surface reconstruction.	46
19	DFT calculation of an LL cysteine dimer.	47
20	DFT calculation of DL cysteine dimers.	48
21	Summary of the DFT results.	51
22	Sketch of the three-point contact model.	52
23	D cysteine pairs on the terrace and at an S kink site.	53
24	D cysteine pair adsorbed at an R kink site and L cysteine pair adsorbed at an S kink site.	54
25	Cysteine double-row structure.	56
26	Large-scale STM image of molecular chains of cysteine on Au(110).	57
27	Ball models of the most stable D cysteine double-row structures.	60
28	Most stable D cysteine double-row structure.	61
29	Dependence of the binding energy of hydrogen bonds on the O–HO distance.	62
30	Growth mechanism of the cysteine chains.	63
31	Alignment of L cysteine pairs.	66
32	Unit cell of the surface restructuring.	67

33	Vacancy structure formation energy calculated by DFT and EMT.	68
34	Cysteine structures on Au(110) after annealing the sample to 380 K.	70
35	High-resolution image of the dense cysteine phase.	71
36	STM images showing the $c(2 \times 2)$ and $c(4 \times 2)$ structures.	72
37	LEED patterns monitored during annealing of a Au(110) surface covered with L cysteine.	73
38	High-coverage DL cysteine after subsequent annealing of the sample to 420 K.	77
39	Model of a kinked Au(110) surface.	78
40	Cysteine as deposited at 120 K and after annealing at 270 K.	82
41	High-resolution cysteine nanoclusters.	83
42	STM images demonstrating the chirality of the nanoclusters.	84
43	Lateral manipulation of a cysteine nanocluster.	85
44	Structure suggestion for the cysteine nanocluster.	87
45	Phase diagram of the cysteine structures on Au(110)- (1×2) .	89
46	Au(110) after 15 min dosing of H_2S at a sample temperature of 470 K.	92
47	STM image of the $c(4 \times 2)$ sulphur structure.	93
48	STM image and model of the $p(4 \times 1)$ sulphur structure.	95
49	STM images after evaporation of cysteine onto Au(111) held at 120 K.	99
50	STM images after evaporation of cysteine on Au(111) held at room temperature.	100
51	Zoom-in on the ordered structure obtained after evaporation of cysteine onto Au(111) held at room temperature.	102
52	STM images showing the internal structure of the cysteine islands after annealing the sample to 380 K.	103
53	High-coverage structures at room temperature.	104
54	High-coverage structure after annealing.	105
55	Thermal desorption spectra for dodecanethiol on Cu(110).	110
56	Dodecanethiol on Cu(110) at 110 K and at room temperature.	112
57	High-resolution STM images of dodecanethiol structures at room temperature.	113
58	Saturation dodecanethiol structure after annealing at 345 K.	115
59	XP spectra for dodecanethiol films.	116
60	Evolution of the intensity ratio of the C 1s and S $2p_{3/2}$ XP peaks.	117
61	LEED pattern for a room-temperature saturation structure of dodecanethiol on the Cu(110).	119
62	Origin of the observed moiré pattern.	123